

VOT 78088

**NANO TUNGSTEN CARBIDE FOR REMEDIATION
CHLOROFLOUROCARBON**

ABD. RAHIM YACOB

**JABATAN KIMIA, FAKULTI SAINS,
UNIVERSITI TEKNOLOGI MALAYSIA**

2009

ACKNOWLEDGEMENT

I would like to express my sincere gratitude to my respectful supervisors, Assoc. Prof. Dr. Abdul Rahim Yacob for all his guidance, advice and encouragement. His kindness and generosity in sharing knowledge and experience is very much appreciated.

I also would like to thank all the lectures especially to Assoc. Prof. Dr. Asiah Hussain and Dr. Zaiton Majid and staffs in Chemistry Department, Ibnu Sina Institute for always been helpful and friendly in helping me to solve my problems through out the period of my research.

I'm very grateful to the 'Black Diamond' research group, Dr. Abdul Rahim Yacob, Ratna and Asraf for being so cooperative and contribute brilliant ideas in completing this research successfully. To all my colleagues, thank you so much for all those times, advices and efforts.

I must express my profound thanks to the Fundamental Research Grant Scheme (FRGS 78088).and PGD Scholarship.

Last but certainly not least, to my adored family members my dad Mr. Inderan, my mom Mrs. Diawanai, my sister Puganeswary and my Brothers Kathir and VimeI. I would like to thank all of you from bottom of my heart for being so supportive. Not forgotten my dearest friend Anilarasu and my lovely juniors Kavi, Praveen and Uma Shangkar for the kind motivation whenever I'm down. Thank you so much.

PREFACE

This thesis is the result of my work carried out in the Department of Chemistry, Universiti Teknologi Malaysia between December 2005 and December 2007 under the supervision of Assoc. Prof. Dr. Abdul Rahim Yacob. Part of my work described in this thesis has been sent for exhibition participations and reported in the following publications:

1. Abd. Rahim, Y., and Vicinisvarri, I (2007). “Haute Superficie De Carbure De Tungstene Pour la Remediation De CFC”. Exhibition participation for the Innova Eureka Exhibition, Silver medal. Brussels, Belgium, 22-25 November 2007.
2. Abd. Rahim, Y. and Vicinisvarri I (2007). “High Surface Area Tungsten Carbide Catalyst Supported on Activated Carbon for the Hydrodehalogenation of Chlorofluorocarbon” Exhibition participation for the PECIPTA 2007. Gold medal award. Kuala Lumpur convention Centre, 10-12 August 2007.
3. Abd. Rahim Y., Zaiton A. M., Asiah H., Ratna Sari Dewi D. and Vicinisvarri I. “Kernel WC for Rocket Thruster’s Fuel. (2007). Exhibition participation for the Malaysia Technology Exhibition 2006. Bronze medal award. Putra World Trade Centre, Kuala Lumpur. 29-31 March 2007.
4. Abd. Rahim Y., Zaiton A. M., Asiah H., Ratna Sari Dewi D. and Vicinisvarri I. (2006). “BLACK DIAMOND”-NanoTungsten Carbide for Hard Metal Tools. Exhibition participation for the Malaysia Technology Exhibition 2006. Bronze medal award. Putra World Trade Centre, Kuala Lumpur. 23-25 February 2006.

5. Vicinisvarri I., Abd. Rahim Y., Asiah H. and Ratna Sari Dewi D. (2006). Preparation and Characterization of Tungsten Catalyst on Activated Carbon. Poster presented at the Annual Fundamental Science Seminar 2005. Ibnu Sina Institute, UTM Skudai, Johor. 6-7 June 2006.

6. Ratna Sari Dewi D, Abd. Rahim Y., Zaiton A. M. and Vicinisvarri I. (2005). Comparison and Physical Characterization of Various Source of High Surface Area Carbon Prepared by Different Types of Activation. Poster presented at the Simposium Kimia Analisis Malaysia 18. Hyatt Regency Hotel, Johor Bahru. 12-14 September 2005.

ABSTRACT

The importance of activated carbon as adsorbent, catalyst and catalyst support has been increased in industry and environmental applications for its special features; a very high surface area absorbency, inertness, and porosity. The surface structure and porosity of an activated carbon largely depended on the starting materials and the activation method used. In this study, activated carbons were prepared from palm kernel shell by chemical activation using zinc chloride under both nitrogen flow and vacuum condition. The effects of impregnation ratio (ZnCl_2 to palm kernel shell) and activation condition on the surface properties of carbons were carefully studied in order to optimize these parameters. All the prepared activated carbons were characterized using FTIR, single point BET surface area, nitrogen adsorption analysis, FESEM-EDX and Thermogravimetry analysis. The selected activated carbons were used as a carbon source as well as catalyst support in the preparation of tungsten carbide (WC). The catalyst was prepared via sublimation technique where the metal precursor tungsten hexacarbonyl and activated carbon were milled together and heat-treated at 700 °C and 950 °C in Helium flow. Two sets of WC catalysts with 6 percent and 15 percent tungsten content were prepared. The heat-treated catalysts were characterized by XRD, single point BET surface area and FESEM-EDX. The performance of the optimal prepared WC catalyst was tested on dichlorodifluoromethane, CFC-12 in hydrodehalogenation reaction. The results show that the impregnation ratio and the activation conditions had significant effect on the properties of activated carbon prepared. In this study the activated carbon prepared with ZnCl_2 impregnation ratio of 1:1 under nitrogen flow (AC-1Z-N) showed the highest surface area, 878 cm^2g^{-1} with micropore volume around 0.36 cm^3g^{-1} . While, the catalyst with 15% tungsten content supported on AC-1Z-N showed the highest formation of tungsten carbide and found to be very active in the hydrodehalogenation reaction of CFC-12.

ABSTRAK

Kepentingan karbon teraktif sebagai bahan penyerap, pemangkin dan penyokong pemangkin semakin meningkat dalam industri kimia disebabkan ciri-ciri unik seperti luas permukaan yang besar, lengai and struktur keliangannya. Struktur permukaan dan sifat keliangan karbon teraktif sangat bergantung kepada bahan pemula dan kaedah pengaktifan. Dalam kajian ini karbon teraktif telah disediakan dengan menggunakan tempurung kelapa sawit melalui kaedah pengaktifan kimia menggunakan zink klorida di bawah aliran gas nitrogen dan keadaan vakum. Kesan nisbah bahan pengaktif $ZnCl_2$ kepada tempurung kelapa sawit telah dikaji untuk membentuk parameter yang optima. Pencirian teliti telah dilakukan menggunakan FTIR, penjerapan titik tunggal BET, analisis penjerapan nitrogen, FESEM-EDX dan TGA. karbon teraktif yang terpilih telah digunakan sebagai sumber karbon dan juga sebagai bahan penyokong kepada mangkin tungsten karbida, WC. Dalam kajian ini mangkin WC telah disediakan melalui teknik pemejalwapan dimana tungsten hexakarbonil dan karbon teraktif digiling dan dipanaskan pada suhu 700 °C dan 950 °C dalam aliran gas helium. Dua set sampel WC dengan kandungan tungsten 6% dan 15% telah disediakan. Pencirian pemangkin WC telah dilakukan menggunakan XRD, titik tunggal BET dan FESEM-EDX. Prestasi mangkin telah diuji melalui tindak balas diklorodiflorometana, CFC-12 hidrodahalogenasi. Keputusan pencirian menunjukkan bahawa nisbah $ZnCl_2$ kepada tempurung kelapa sawit dan keadaan pengaktifan memberi kesan yang penting keatas sifat karbon teraktif. Dalam kajian ini karbon teraktif yang telah disediakan dengan nisbah $ZnCl_2$ kepada tempurung kelapa sawit, 1:1 mempunyai luas permukaan yang tinggi iaitu $878 \text{ m}^2\text{g}^{-1}$ dengan isipadu mikroliang $0.36 \text{ m}^3\text{g}^{-1}$. Sementara mangkin dengan kandungan 15% tungsten yang disediakan dengan AC-1Z-N menunjukkan pembentukan tungsten karbida yang tertinggi dan didapati sangat aktif dalam tindak balas CFC-12 hidrodahalogenasi.

TABLE OF CONTENTS

CHAPTER	TITLE	PAGE
	DECLARATION	ii
	DEDICATION	iii
	ACKNOWLEDGEMENTS	iv
	PREFACE	v
	ABSTRACT	vi
	ABSTRAK	vii
	TABLE OF CONTENTS	viii
	LIST OF TABLES	xii
	LIST OF FIGURES	xiv
	LIST OF SYMBOLS / ABBREVIATIONS	xvii
	LIST OF APPENDICES	xix
1	INTRODUCTION	
	1.1 Problem Statement	3
	1.2 Objective of the Research	4
	1.3 Scope of Studies	4
2	LITERATURE REVIEWS	
	2.1 Activated Carbon	6
	2.1.1 Physical Properties of Activated Carbon	7

2.2	Agricultural Byproduct as Raw Material	8
2.3	Preparation of Activated Aarbon	10
2.3.1	Selecting Raw Material	10
2.3.2	Pre-treatment	12
2.3.3	Carbonization	12
2.3.4	Activation	13
	2.3.4.1 Activation with Zinc Chloride	14
2.3.5	Washing	15
2.4	Catalyst Support	15
2.4.1	Activated Carbon as Catalyst Support	18
2.5	Transition metal carbides	19
2.5.1	Tungsten Carbide in Catalytic Usages	21
2.6	Chlorofluorocarbons (CFCs)	22
2.6.1	Remediation and Conversion of CFCs	23
2.6.2	Hydrodehalogenation of CFCs on Tungsten Carbide	25
2.7	Preparation of Tungsten Carbide	27
2.8	Fourier Transform Infrared (FTIR)	28
2.9.	Nitrogen adsorption analysis	29
2.9.1	Adsorption Isotherms	31
2.9.2	Brunauer, Emmett and Teller (BET) Surface Area	33
2.9.3	The <i>t</i> -plot	34
2.10	Thermogravimetry Analysis (TGA)	35
2.11	Field Emission Scanning Electron Microscopy (FESEM) and Energy Dispersive X-ray Spectroscopy (EDX)	36
2.12	X-ray Diffraction (XRD)	37
2.13	Gas Chromatography (GC)	39

3

EXPERIMENTAL

3.1	Instrumentations	41
3.2	Chemicals	43

3.3	Preparation of Activated Carbon	43
3.3.1	Preparation of raw material	43
3.3.2	Chemical activation	44
3.4	Preparation of Tungsten Carbide	46
3.5	Sample Characterization	48
3.5.1	Characterization of activated carbon	48
3.5.2	Characterization of tungsten carbide	49
3.6	Catalytic testing-Hydrodehalogenation of CFC-12	49

4

RESULTS AND DISCUSSION

4.1	General	51
4.2	Characterization of Activated Carbons	51
4.2.1	Fourier Transform Infrared Spectroscopy	52
4.2.2	Nitrogen Adsorption Analysis	56
4.2.2.1	Single Point BET Surface Area	57
4.2.2.2	BDDT Isotherms and Pore Size Distribution	59
4.2.2.3	The <i>t</i> -plot	65
4.2.3	FESEM analysis of Activated Carbons	67
4.2.4	Energy Dispersive X-ray Analysis	72
4.2.5	Thermogravimetry Analysis	73
4.2.5.1	Thermogravimetry Analysis of Raw palm Kernel Shell	74
4.2.5.2	Thermogravimetry analysis of Activated Carbon in Air Flow	75
4.2.5.3	Thermogravimetry Analysis of Activated Carbon in Nitrogen Flow	78
4.3	Tungsten Carbide Catalyst	80
4.3.1.	X-ray diffraction	81
4.3.1.1	XRD analysis of Tungsten Carbide Catalyst Supported on AC-1Z-N	81
4.3.1.2	XRD analysis of Tungsten Carbide Catalyst Supported on AC-1Z-V	85

4.3.2	Field Emission Scanning Electron Microscopy	88
4.3.3	Single point BET Surface Area	91
4.4	Hydrodehalogenation of CFC-12	93
5	CONCLUSIONS	97
	REFERENCES	99
	APPENDICES	108

LIST OF TABLES

TABLE NO.	TITLE	PAGE
2.1	Classification of pores of a porous material	8
2.2	Agricultural by-products used to produce activated carbon	9
2.3	Physical and chemical properties of supports	17
2.4	Type of catalyst supports and their applications	18
3.1	Notation for tungsten carbide samples	48
4.1	Sample notation for activated carbons	53
4.2	Vibration wavenumber and functional groups of the samples	57
4.3	Surface area and pore volume of activated carbon	67
4.4	EDX analysis of activated carbons	74
4.5	Percentage of weight loss of AC-1Z-N and AC-1Z-V in air flow	78
4.6	Percentage of weight loss of AC-1Z-N and AC-1Z-V in nitrogen flow	80
4.7	Notation for the samples prepared	82
4.8	Relative intensity of main peaks for AC-1Z-N supported catalysts	85
4.9	Relative intensity of main peaks for AC-1Z-V supported catalysts	89
4.10	Single point BET surface area of samples	93

LIST OF FIGURES

FIGURE NO.	TITLE	
PAGE		
2.1	structure of transition metal carbides	20
2.2	The gas sorption process	30
2.3	Types of BDDT physisorption isotherm	32
2.4	X-ray scattered by atoms in an ordered lattice interfere constructively in direction given by Braggs Law	39
2.5	Diagram of a gas chromatograph	41
3.1	Flow diagram for the preparation of activated carbon	46
3.2	Schematic diagram of vacuum line system	47
3.3	Schematic set-up used for heat-treatment of tungsten carbide catalyst	49
3.4	Schematic set-up for hydrodehalogenation catalytic reaction	51
4.1	FTIR spectra for raw palm kernel shell, commercial activated carbon and samples activate in vacuum condition	54
4.2	FTIR spectra for raw pal kernel shell, commercial activated carbon and amples activate in nitrogen flow	55
4.3	Single point BET surface area of raw-PKS and prepared	

	activated carbon	58
4.4	BDDT isotherm of AC-1Z-N and AC-1Z-V	61
4.5	Pore size distribution graph of AC-1Z-N	62
4.6	Pore size distribution graph of AC-1Z-V	62
4.7	BDDT isotherm of AC-2Z-N and AC-2Z-V	64
4.8	Pore size distribution of AC-2Z-N	65
4.9	Pore size distribution of AC-2Z-V	65
4.10	Micrograph of raw-PKS with magnification of 500x	69
4.11	Micrograph of AC-1Z-N with magnification of 150x	70
4.12	Micrograph of AC-1Z-N with magnification of 7500x	70
4.13	Micrograph of AC-1Z-V with magnification of 150x	71
4.14	Micrograph of AC-1Z-V with magnification of 500x	71
4.15	Micrograph of AC-2Z-N with magnification of 250x	72
4.16	Micrograph of AC-2Z-N with magnification of 350x	73
4.17	TGA/DTG of raw-PKS	75
4.18	TGA/DTG of AC-1Z-N in air flow	77
4.19	TGA/DTG of AC-1Z-V in air flow	77
4.20	TGA/DTG of AC-1Z-N in nitrogen flow	79
4.21	TGA/DTG of AC-1Z-V in nitrogen flow	80
4.22	X-ray diffractogram of samples with 6 percent of tungsten content supported on AC-1Z-N	83
4.23	X-ray diffractogram of samples with 15 percent of tungsten content supported on AC-1Z-N	84
4.24	X-ray diffractogram of samples with 6 percent of tungsten content supported on AC-1Z-V	87

4.25	X-ray diffractogram of samples with 15 percent of tungsten content supported on AC-1Z-V	88
4.26	Micrograph of ACN-15-950 with magnification of 140x	90
4.27	Micrograph of ACV-15-950 with magnification of 840x	90
4.28	EDX of ACN-15-950	91
4.29	EDX of ACV-15-950	92
4.30	Chromatogram of CFC-12 gas	95
4.31	Chromatogram of product mixture at different temperature	96
4.32	Conversion of CFC-12	97

LIST OF SYMBOLS / ABBREVIATIONS

°C	-	degree Celsius
µm	-	micrometer
BET	-	Brunauer-Emmett-Teller
cm	-	centimetre
DTA	-	Differential thermal analysis
EDX	-	Energy Dispersive X-ray analysis
Eq.	-	Equation
FTIR	-	Fourier Transformation Infra red
g	-	gram
ID	-	internal diameter
K	-	Kelvin
ksi	-	kips per linear foot
kV	-	kilo volt
mA	-	mili ampere
NA	-	nitrogen adsorption
mL	-	millilitre
nm	-	nanometer
rpm	-	rotation per minute

TG	-	Thermogravimetry
XRD	-	X-ray Diffraction
θ	-	Half angle of diffraction beam
λ	-	wavelength

LIST OF APPENDICES

APPENDIX NO.	TITLE	PAGE
1	Calculation of weight used from atomic weight percentage ratio of tungsten and activated carbon support in tungsten carbide preparation	110
2	Nitrogen Adsorption Data of AC-1Z-N	111
3	Nitrogen Adsorption Data of AC-1Z-V	112
4	Nitrogen Adsorption Data of AC-2Z-N	113
5	Nitrogen Adsorption Data of AC-2Z-V	114
6	<i>t</i> -Plot Analysis of AC-1Z-N	115
7	<i>t</i> -Plot Analysis of AC-1Z-V	117
8	<i>t</i> -Plot Analysis of AC-2Z-N	119
9	<i>t</i> -Plot Analysis of AC-2Z-V	121
10	EDX Spectrum of AC-1Z-N	123
11	EDX Spectrum of AC-1Z-V	124
12	EDX Spectrum of AC-2Z-N	125
13	EDX Spectrum of ACN-15-950	126
14	EDX Spectrum of ACN-15-950	127

CHAPTER 1

INTRODUCTION

Activated carbons are carbonaceous materials that have highly developed porosity and internal surface area. They are widely used in a number of applications, such as separation and storage of gases; recovery of chemical products, removal of organic pollutants from drinking water and also as catalyst support. The increasing usage and competitiveness of activated carbon prices, has prompted the usage of agricultural by-products such as coconut shell (Azevedo *et al.*, 2007), pistachio shell (Lua *et al.*, 2004), saw dust (Mohanty *et al.*, 2005), and walnut shell (Alvim-Ferraz *et al.*, 2003) as raw materials to prepare activated carbon. The physical properties of an activated carbon depend on the raw material and its treatment (Manocha, 2003).

Base on a study done by Kawser and Farid (2000), Malaysia generates 7.7 million tonnes of empty fruit bunches 6.0 million tonnes of fibre and 2.4 million tonnes of palm kernel shell every year. These by-products often considered as waste and have cause significant disposal problem. Therefore, in this research palm kernel shell was used as a starting material to prepare activated carbon in addition it is also a feasible solution to this environmental issue. The prepared activated carbon is then used as the carbon source as well as catalyst support for tungsten carbide catalyst.

The most important parameters for the catalyst support are inertness, porosity and surface area (Cameron *et al.*, 1990) Activated carbon is a material that combines all these characteristics optimally and additionally it has unique properties like its

stability in both acidic and basic media, high surface area, microporosity, and cost effectiveness (Jankowska *et al.*, 1991, and Auer *et al.*, 1998).

The catalytic properties of tungsten carbide have attracted interest since Levy and Boudard (1973) first discovered that the carbides of groups IV-VI resemble the catalytic properties similar to those of Platinum group metals. Since then they have been investigated for application in heterogeneous catalysis. To date, the use of tungsten carbide as well as other transition metal carbides as heterogeneous catalysts has grown (Keller *et al.*, 1991; Moreno-Castilla *et al.*, 2001 and Oxley *et al.*, 2004)

Several methods have been developed for the preparation of tungsten carbide and mostly involve solid precursor and reducing agent (Gao and Kear, 1997; Liang *et al.*, 2003). In general the resulting carbide has a low surface area. Therefore in this research tungsten carbide catalyst supported on activated carbon was prepared to obtain a high surface area catalyst. The catalyst was then tested on hydrodehalogenation of dichlorodifluoromethane (CCl_2F_2 ; CFC-12).

The widespread application of CFCs in industry including refrigeration, foam blowing agent and cleaning agent cause severe damage to the ozone layer and contributed significantly to global warming. Thus, destruction of ozone depleting substances especially CFCs has been attract many researchers interest since their production and uses have been phase out under international agreement known as Montreal Protocol (UNEP 2000). Presently, several treatment technologies are available such as thermal incineration, catalytic conversion and activated carbon adsorption. Among them catalytic conversion of CFCs into valuable compounds like hydrofluorocarbon (HFC) seem to be an attractive technique (Yu *et al.*, 2006).

In past few years, the catalytic performances of transition metal carbide catalyst for hydrodehalogenation of CFCs have been studies because of their low cost and Platinum-like behaviour in catalysis (Delannoy *et al.*, 2000 and Oxley *et al.*, 2004);. Thus, the tungsten carbide catalyst prepared in this research can be a potential substitute for the traditional catalyst platinum and palladium.

In this study, high surface area tungsten carbide catalyst supported on activated carbon was prepared. Locally obtained palm kernel shell was used as starting material to produce activated carbon. The resulting catalyst was then tested in catalytic hydrodehalogenation reaction of dichlorodifluoromethane, CFC-12.

1.1 Problem Statement

Palm kernel shell, is an abundant tropical waste from palm oil processing mills in tropical countries like Malaysia and Thailand. They either treat the waste by disposing it or use it as fuel. To economically utilize these agricultural by-products, it is proposed to use them as prospective starting materials for the preparation of activated carbon.

For the past few years a number of studies have been conducted on the preparation of activated carbon from palm kernel shells. However, so far there is no research has been done on application of palm kernel shell base activated carbon as tungsten carbide catalyst support. Tungsten carbide catalyst has exhibited platinum-like catalytic properties but is difficult to prepare with high surface area. The present work was devoted to study kernel shell base activated carbon as the carbon source as well as catalyst support towards synthesis a high surface area tungsten carbide catalyst. The optimal prepared tungsten carbide catalyst was tested on catalytic hydrodehalogenation of CFC-12 to find an economic approach to the remediation of CFCs.

1.2 Objective of the Research

The objectives of this research are as follows:

- 1) To prepare high surface area activated carbon from palm kernel shells.
- 2) To study the surface physical properties of the prepared activated carbon support.
- 3) To prepare and optimize condition for high surface area tungsten carbide catalyst using activated carbon.
- 4) To carry out the catalytic testing of hydrodehalogenation of CFC-12 using the optimal laboratory prepared tungsten carbide catalyst.

1.3 Scope of Studies

The first part of this study is concentrated on preparing the high surface area activated carbon using locally obtained raw material, palm kernel shells. Activated carbons were prepared by chemical activation using zinc chloride under both nitrogen flow and vacuum condition. The effects of impregnation ratio (ZnCl_2 to palm kernel shell) and activation condition on the surface properties of carbons were studied in order to optimize these parameters. The prepared activated carbons will be characterized using several techniques which are, Fourier transform infrared (FTIR), single point BET analysis, nitrogen adsorption, field emission scanning electron microscopy (FESEM) and Thermogravimetry analysis (TGA).

The prepared activated carbons used as the carbon source as well as catalyst support for tungsten carbide catalyst. The catalyst was prepared via sublimation technique followed by heat-treatment.

Catalytic testing hydrodehalogenation of CFC-12 was carried out using the optimal laboratory prepared tungsten carbide. The performances of tungsten carbide catalyst at temperature range from 200 °C to 350 °C were studied as an alternative for the expensive commercially available catalyst.

CHAPTER 2

LITERATURE REVIEW

2.1 Activated Carbon

Activated carbon is an amorphous form of carbon which shows a very disordered of graphite-like crystalline composed of complex aromatic-aliphatic forms. The crystallites are randomly oriented and extensively interconnected (Radovic, 2001).

The structure of an activated carbon may be visualized as a stack of poorly developed aromatic sheets, distributed and cross-linked in a random manner, separated by disordered carbonaceous matter and inorganic matter (ash) derived from the raw material. The anisotropic crystallite alignment is associated with the presence of void (Banosz, 2006). During the activation process, the spaces between crystallites become cleared of less organized carbonaceous matter and at the same time some of the carbon is removed from the crystallites. The resulting channels through the graphitic regions and interstices between the crystallites of the activated carbon make up the porous structure which usually has large surface area. Thus, the pore size distributions for a typical activated carbon are complex and cover a wide range of pore widths (Jankowska *et al.*, 1991; Jaroniec *et al.*, 1996).

2.1.1 Physical properties of activated carbon

The adsorption capacity of an activated carbon depends largely on the presence of pore structure. The surface area and pore structure are perhaps the main physical properties that characterize activated carbon and are interrelated to each other (Ahmad *et al.*, 2007; Prauchner and Rodriguez-Reinoso, 2007).

The surface of any solid is hardly ever truly plane on an atomic scale but there are always present cracks and fissures some of which may penetrate very deeply, and these will contribute towards the internal surface. Meanwhile the superficial cracks and indentations will contribute towards the external surface. The external surface may be taken to include all the prominence and all of those cracks which are wider than they are deep and internal surface on the other will then comprise the walls of all cracks, pores and cavities which are deeper than they are wide (Ponec *et al.*, 1974).

Usually commercial activated carbons have specific surface areas ranging from 400-1500 m²g⁻¹ (Marsh and Rodriguez-Reinoso, 2006). However, recently values of up to 4000 m²g⁻¹ are found for some super activated carbon and these are unrealistically high. Generally, the larger the specific surface area, the higher will be its adsorption capacity. (Lua and Guo, 1998).

The pore systems of an activated carbon are of many different kinds that may vary greatly both in size and in shape within a solid. According to the International Union of Pure and Applied Chemistry (IUPAC), the pores of a porous material are classified in three categories as shown in Table 2.1 (Kinoshita, 1987). These values represent the width, i.e. the distance between the pore wall for slit-shape pores and the radius for cylindrical pores. The classification of pores is introduced based on nitrogen, N₂ adsorption at 77 K, where N₂ molecules adsorbed by different mechanisms (multilayer adsorption, capillary condensation and micropore filling.) (Radovic, 2001).

Table 2.1: Classification of pores of a porous material

Type of pores	Diameter of pores (nm)
Macropores	>50
Mesopores	2-50
Micropores	<2

Each of these groups of pores plays a specific role in the adsorption process. Macropores, >50 nm, is considered as being open surface, and assists only with transport of adsorptive into interior of carbon particles, where adsorption takes place mainly in the micropores (Marsh and Rodriguez-Reinoso, 2006). The process of filling their volume with adsorbate takes place via the mechanism of multilayer adsorption. Mesopores (2-50 nm) also perform as the main transport arteries for the adsorbate. In mesopores the volume filled with adsorbate via the mechanism of capillary condensation. Micropores, <2 nm, have sizes comparable with those of adsorbed molecules. The energy of adsorption in micropores is substantially greater than that for adsorption in mesopores or at non-porous surface, which cause a particularly large increase of adsorption capacity for small equilibrium pressure of adsorbate. In, micropores adsorption proceeds via the mechanism of volume filling (Jankowska *et al.*, 1991).

2.2 Agricultural by-products as raw material for activated carbon

Agricultural by-products have proved to be promising raw materials for the preparation of activated carbons because of the availability at low cost. Table 2.2 summarizes some of the agricultural residues that were used to produce activated carbon. The BET surface area and pore volume of the activated carbon are also tabulated in the same table. Other precursors such as minerals (bituminous coal and lignite) have high degree of inorganic material, of the order of 20% (Minkova *et al.*, 1991), which necessitates demineralization followed by washing steps so that the

material obtains certain properties (Kinoshita, 1987) required for the preparation of activated carbons. In addition high content of inorganic material lowers the resulting yield of the final product. Consequently the total cost and time of the preparation process increase (Galiatsatou *et al.*, 2001). In construct, the low ash content and absence of sulphur and heavy metals in the agricultural raw material eliminates some time consuming and expensive procedural steps. Therefore, the preparation of activated carbon from agricultural by-products has been encouraged, since they are considered as waste and their use in this manner would prevent their accumulation.

Table 2.2: Agricultural by-products used to produce activated carbon

Agricultural by-product	BET surface area (m² g⁻¹)	Micropore volume (cm³ g⁻¹)	Reference
Pistachio nut-shell	1579	0.322	Lua <i>et al</i> (2004)
Apricot stone	728	0.320	Youssef <i>et al</i> (2005)
Coconut shell	2114	1.142	Azevedo <i>et al.</i> (2007)
Oil palm wood	1084	Not reported	Ahmad <i>et al.</i> (2007)
<i>Tectona grandis</i> sawdust	585	0.442	Mohanty <i>et al.</i> (2005)
Olive stone	686	0.200	Galiatsatou <i>et al.</i> (2001)
Almond shell	438	Not reported	Alvim-Ferraz <i>et al.</i> (2003)

Oil palm (*Elaeis guineensis*) is a major source of edible oil which is extracted from its fruits. However, palm-oil mills produced large amount of solid wastes, such as extracted palm oil fibres, palm shells, palm gases, stones and empty fruit bunches. For example, here in Malaysia, more than two million tons (dry weight) of extracted oil palm fibre are estimated to be generated annually (Lua and Guo., 1998). It is estimated that for every one million tonnes of palm oil produced, 0.8 million tonnes of palm shells is created (Daud *et al.*, 2000). Based on a total oil production in Malaysia of 7.4 million tonnes in 1993, the amount of palm shell generated in that year alone was about 6 million tonnes. To economically utilize these agricultural by-products, it

is proposed to use them as prospective starting materials for the preparation of activated carbon as they have high density, relatively high carbon content and low ash content.

Palm kernel shell (*endocarp*) is a lignocellulosic material which content 29.7% cellulose, 47.7% hemicellulose and 53.4% lignin (Suhas *et al.*, 2007). Studies were made to compare the pore development in activated carbons produced under identical conditions from palm shell and coconut shell by Daud and Ali (2004). It was stated that the surface area and the porosity of palm kernel shell based carbons which are high lignin content, were found to be more compared to coconut based carbons (30.1% lignin).

2.3 Preparation of activated carbon

Basically, the preparation of activated carbon consists of four steps, namely selection of raw materials, pretreatment, carbonization, activation and finally washing. However, the main process for manufacturing activated carbon only involves two steps; the carbonization of the raw material and activation of the carbonized product.

2.3.1 Selecting of raw materials

In the selection of an appropriate raw material for preparation of activated carbon, several factors are taken into consideration. Industrially, inexpensive raw material with high carbon and low ash content is preferred as raw material for the production of activated carbon. High density of the precursor and sufficient volatile content are of considerable importance. Evolution of volatiles during pyrolysis results

in porous char, essential for making activated carbons (Manocha, 2003). While high density contributes to enhanced structural strength of the carbon, essential to withstand excessive particle crumble during use (Stiles, 1987).

It is widely agreed that the pore structure and pore size distribution of an activated carbon is largely determined by the nature of the starting material. A study conducted by Rodriguez-Reinoso and Solana (1989) on several agricultural wastes such as peach stone, sherry stone, palm stone and almond shell found that the botanical family of the material influences the pore size distribution as well as the pore size.

One of the parameter which differentiates one material from another is the material composition, cellulose, halocellulose and lignin. Gergova *et al.* (1994) produced activated carbon from grape seed and cherry stone and attributes the predominantly mesopore and macropore structure of the carbon produced from them to the high lignin content in the raw material. The work also revealed the possibility of selecting raw materials to produce activated carbon with certain pore distribution by recognizing their differences in material content. For example, if an activated carbon with significant amount of mesopores and macropores is required, it may be produced from lignocellulosic materials that contain comparatively high percentage of lignin content.

In this research palm kernel shells which have high density, relatively high fixed carbon, and low ash content were used as starting material to produce high surface area activated carbon.

2.3.2 Pre-treatment

The raw material will need pretreatments prior to its activation. In the case of regular powdered or granular carbons, the raw material must first be prepared to require size by grinding and sieving. Sometimes, a washing step is applied with water or acid in order to remove any dirt coming with the raw material and to reduce any mineral matter.

2.3.3 Carbonization

Carbonization process involves pyrolysis of the raw material at moderate temperature (100-400 °C) in the absence of air, normally performed in the presence of a stream of nitrogen (N₂) and carbon dioxide (CO₂) to remove the volatile matters and produce chars with rudimentary pore structures (Manocha, 2003; Marsh and Rodriguez-Reinoso, 2006) .

During the carbonization of the raw materials, heteroatoms such as oxygen, hydrogen and nitrogen are eliminated as volatile gaseous products and the residual elementary carbon atoms are then grouped into stacks of flat aromatic sheets cross linked in a random manner. Since the arrangement of these sheets is irregular, it leaves free interstices among them. The porosity of char which refers to the interstices is not then completely accessible and tends to be filled or partially blocked with tars and other decomposition products which become disorganized carbon (Rodriguez-Reinoso, 1997).

Carbonization temperature has the most significant effect followed by, the nitrogen flow rate and then finally the carbonization residence time. Generally increasing carbonization temperature reduces yield of activated carbon. According to Putun *et al.* (2005), increasing temperature leads to a decreased yield solid and an increased yield of liquid and gasses. As the temperature is raised, there is a rise in ash and fixed carbon percentage and there is a decrease in volatile matter. Consequently,

higher temperature yields chars of greater quality. The decrease in the char yield with increasing temperature could either be due to greater primary decomposition of biomass at higher temperature or secondary decomposition of char residue.

2.3.4 Activation

As discussed above, during the carbonization the free interstices present in carbon filled or at least partially blocked by tar substances. The resulting carbonized product has only a very small adsorption capacity (Bandosz, 2006). The purpose of activation is to enlarge the diameters of pores which are created during the carbonization process and to create some new porosity. Activation can be carried out by physical and chemical means (Auer *et al.*, 1998).

Physical activation is a process by which the carbonized product develops porous structure and extended surface area on heat treatment in the temperature range from 800-1000 °C in the presence of suitable oxidizing gases such as steam or CO₂, (Rodriguez-Reinoso *et al.*, 1995; Ratna *et al.*, 2005).

In chemical activation process the two steps, carbonization and activation carried out simultaneously, with the precursor being mixed with chemical activating agents, as dehydrating agents and oxidants. Once the impregnation step is complete, heat treatment is carried out under a flow of nitrogen and the resulting carbon is washed to eliminate remaining chemical (Molina-Sabio and Rodriguez-Reinoso, 2004). Chemical activation offers several advantages since it is carried out in a single step, performed at lower temperatures and therefore resulting in development of a better porous structure (Ioannidou and Zabaniotou *et al.*, 2007). The chemical agents normally used such as zinc chloride, phosphoric acid, calcium chloride or potassium hydroxide. In this study activated carbons were prepared via chemical activation using zinc chloride.

2.3.4.1 Activation with zinc chloride

Zinc chloride was the principal method of chemical activation up to 1970, and it is still used in China. Initially, the precursor is mixed with the chemical (ZnCl_2) in an aqueous solution to form a paste and the mixture kept at around 85-110 °C without evaporation. In this way, the swelling of the interior channels of the botanic structure allows for better access of the reactant to the interior of the particle. Further partial or complete evaporation of solution will force the incorporation of the reactant to the interior of the particles. After the evaporation, the impregnated carbon heat treated in an inert atmosphere at temperature between 600 – 750 °C (Marsh and Rodriguez-Reinoso, 2006). During the heat treatment ZnCl_2 acts as a dehydrating agent favouring the elimination of hydrogen and oxygen as water instead of CO_x or hydrocarbons. Thus inhibiting the loss of volatile matter as well as tars and leaving behind more fixed carbon and consequently a higher reaction solid yield (Almansa *et al.*, 2004).

The extent of chemical activation can significantly alter the characteristics of the produced carbons. According to Caturla *et al.*, (1991), at high ZnCl_2 concentrations, some ZnCl_2 remains in external part of the carbon particles and widens the porosity by a localized decomposition of organic matter. This process results in the enhancement of meso and macropore formation. Ahmadopour and Do (1997) described pore evolution with respect activating agents and showed that micropore formation is predominant when ZnCl_2 to precursor mass ratio is less than one. They also observed that when impregnation ratio is greater than 2, pore widening becomes the dominant mechanism and meso pores formed.

Preparation of activated carbons by chemical activation in inert atmosphere such as nitrogen had been carried out by many researches (Molina-Sabio and Rodriguez-Reinoso, 2004; Khalili *et al.*, 2000); however, chemical activation of palm kernel shell base carbon under vacuum conditions seldom reported in the literature.

Therefore, in this study the effects of different parameters, the impregnation ratio and the activation condition (nitrogen gas and vacuum) on pore development were studied.

2.3.5 Washing

Some applications need very pure activated carbons, and to comply with this need many manufacturers remove most of the ash components by washing the carbon with water or acids such as hydrochloric or nitric acid. In some cases a more exhaustive washing is requires the use of hydrofluoric acids to eliminate the aluminosilicate components of the ash. The washing process is very important when the carbon is to be used in pharmaceutical preparations, food industries or in catalysis particularly when the carbon is used either as a catalyst or a catalyst support. Furthermore, the high ash content and impurities may influence the activity of catalyst (Auer *et al.*, 1998)

2.4 Catalyst Support

Catalyst support is vital important in today's chemical industry. The primary aim of the support is to improve dispersion significantly and provide access to a much large number of catalytically active species. In addition, the support may also be added to stabilize the catalyst against agglomeration and sintering (Stiles, 1987).

Normally catalyst supports are consist of inert substances that provide a means of spreading out an expensive catalyst ingredient, especially precious metal in order to achieve a greater effective utilization of the metal compare with a bulk metal system.

The most important physical characteristics of a catalyst support are hardness, surface area, porosity and pore size distribution (Winterbottom and King, 1999).

High surface area and well developed porosity are essential for achieving large metal dispersions, which usually results in high catalytic activity. The pore size distribution plays an important role, for it not only determines the surface area available but also control the diffusion of substrate molecules to catalytically active site and thus exhibit higher activity.

Normally, the nature of reaction system largely determines the type of catalyst support. For a liquid phase reaction, in which large or complex molecules are being processed, it is essential that the pore size be relatively large which means that the surface area must be relatively low. The definition of low surface area would be in the range from 1 to 125 m²g⁻¹, whereas high surface area would be in the range of 125 to 2000 m²g⁻¹ (Stiles, 1987). Generally, catalysts for the activation of hydrogen (hydrogenation Moreno-Castilla *et al.*, 2001), hydrodehalogenation (Delannoy *et al.*, 2000), hydrodesulfurization and hydronitrogenation (Landau, 1997) require high surface area support, whereas selective oxidations such as olefin epoxidation (Yu *et al.*, 2007) need low surface area support to suppress the undesirable reactions.

Basically in selecting an appropriate support for a particular catalyst, a numerous physical and chemical aspects must be taken into account. Table 2.3 shows the desirable physical and chemical properties to be considered in choosing a support (Winterbottom, 1999; Hagen, 2006).

Table 2.3: Physical and chemical properties of supports

Physical properties	Chemical properties
----------------------------	----------------------------

i. surface area (activity and distribution of catalyst)	i. Inert to undesirable reactions
ii. Porosity (mass and heat transport)	ii. Stable under reaction and regeneration condition
iii. Partical size and shape (pore diffusion)	iii. Interaction with active component (to improve activity and selectivity)
iv. Mechanical stability (abrasion and durability)	iv. Stabilize the catalyst against sintering
v. Thermal stability (catalyst lifetime and regenerability)	v. Minimise catalyst poisoning
vi. Bulk density (active component content per unit reactor volume)	
vii. Separability (filterability of powder catalysts)	

There are various types of catalyst supports available commercially. Table 2.4 shows the type of catalyst supports and their applications in chemical industry. Among these supports, alumina, silica, zeolite and activated carbon are used in most of the industrial catalytic process (Rodriguez-Reinoso, 1997; Winterbottom, 1999).

Table 2.4: Type of catalyst supports and their applications (Stiles, 1987)

Support	Specific surface area (m ² g ⁻¹)	Applications
Alumina	160-300	Hydrogenation, dehydrogenation and metathesis.
Alumina silicate	>800	Cracking reactions, dehydration, isomerization and ammoxidation.
Silica	200-1000	Polymerization, hydrogenation, oxidation and NO _x reduction
Titania	40-200	Selective oxidation, oxidation of <i>o</i> -xylene to phthalic anhydride.
Activated carbon	600-2000	hydrogenation with precious metal catalysts (fine chemical), oxidation.
Clay	50-300	Hydrogenation and condensation
Zeolites	300-600	Refinery processing, by functional catalysis and organic synthesis.

2.4.1 Activated Carbon as Catalyst Support

Activated carbon has been used for decades in heterogeneous catalysis. It is used predominantly as a support for metal catalysts especially precious metal in fine chemicals, petroleum refining and also environmental applications.

A very important point for the economic use of precious metal catalysts in chemical industry is recovery, refining and recycling of the metal. This procedure is simplified by the use of activated carbon as support where this material can be burnt off, and produce high concentrated ashes that permit an economical recovery of precious metal. This technology is also environmental friendly, for it does not produce large amount of solid waste that need to be land filled (Auer *et al.*, 1998).

Today activated carbon supported catalysts are used in a vast number of catalytic reactions. The majority of the reactions involved hydrogenation reactions. Hydrogenation of nitrobenzene (Perez *et al.*, 1997), ethylene (Moreno-Castilla *et al.*, 2001), halogenated nitroaromatic compound and carbon monoxide in alcohol synthesis (Zhong-rui *et al.*, 2001) are some of the reaction that used activated carbon supported catalyst. In environmental applications activated carbon supported catalysts are used in conversion of halocarbons towards remediation of ozone layer depletion (Oxley *et al.*, 2004).

2.5 Transition metal carbide

The transition metals also known as transition elements occupy the space between group 2 and group 3 of the periodic table. The incorporation of carbon into lattices of early transition metals (IVB-VIB) produces compounds with unique physical, chemical and catalytic properties, which combine the characteristic properties of three different classes materials: covalent solids, ionic crystals and transition metals. These resulting alloys are referred to transition metal carbides. The carbides are well known for their hardness, strength, high melting points, and also characteristics of ceramic materials (Toth, 1971).

The carbides of early transition metal are often characterized by simple crystal structures. The metal atoms form lattices of face-centered cubic (fcc), hexagonal packed (hcp), or simple hexagonal (hex) structures, while carbon atoms reside in interstitial sites between metal atoms (Oyama, 1996). Figure 2.1 show respective structures of transition metal carbides. Referring to Figure 2.1 the open and filled circles represent metal and non-metal atoms (carbon), respectively. In general, carbon atoms occupy the largest interstitial sites available, for this reason, transition metal carbides are often termed interstitial alloys (Chen, 1996).

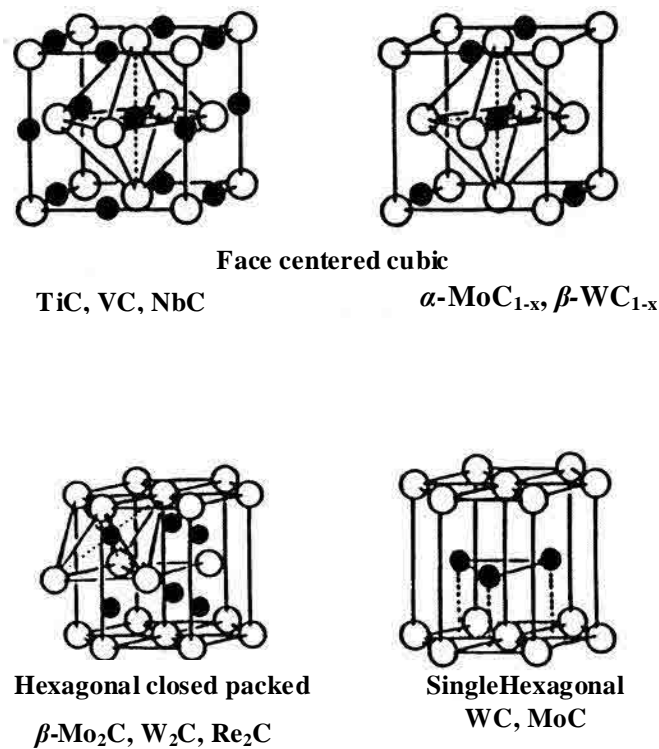


Figure 2.1: structure of transition metal carbides

Theoretical band calculations of transition metal carbides have indicated that the bonding in these compounds involves simultaneous contribution from metallic, covalent and ionic bonding. The metallic bonding is related to the rearrangement of metal-metal bonds; the covalent contribution is due to the formation of covalent bonds between metal and nonmetal atoms; and the ionic is characterized by the charge transfer between metal and nonmetal atoms. The formation of carbide modifies the nature of the d band of the parent metal, which in turn gives rise to catalytic properties that are different from those of the parent metals but similar to those of group VIII noble metals (Oyama and Keiffer, 1992).

Carbides have been demonstrated to have excellent catalytic activities in variety of reactions, including hydrogenolysis, hydrogenation, dehydrogenation, isomerization, hydrodesulfurization, hydrodenitrogenation and ammonia synthesis. One of the primary interests in the applications of carbides in these reactions was to use them as cheaper alternative catalysts to replace group VIII noble metals. In many

cases the catalytic activities of carbide resemble those of noble metals. Another potential catalytic advantage of carbides is that they often show higher sulfur and nitrogen tolerance than the noble metals.

2.5.1 Tungsten carbide in catalytic usages

The catalytic properties of tungsten carbide have attracted interest since Levy and Boudart (1973) drew some parallels from qualitative points of view between WC and Pt. They found that WC catalyzes the formation of water from hydrogen and oxygen at room temperature, the reduction of tungsten trioxide by hydrogen in the presence of water, and isomerization of 2,2-dimethylpropene to 2-methylbutane. This catalytic behaviour, which is typical of platinum, is not exhibited at all by tungsten.

Levy and Boudart (1973) speculated that the catalytic properties of WC resulted from electronic structure. They suggested that carbon electron increased the apparent electron to atom ratio, producing a more Pt-like electronic structure. This observation was wrongly interpreted as a speculation that there was electron transfer from carbon to tungsten d band producing a Pt like charge distribution and hence, Pt like chemical properties. Latter, the similarity between Fermi level electronic density of states (DOS) for Pt and WC was confirmed by number of spectroscopic investigations. In these investigations the XPS spectra of W, WC and Pt were compared. It was found that there were in fact similarities between the Fermi level DOS for Pt and WC but not for W and Pt or W and WC (Houston *et al.*, 1974; Bennett *et al.*, 1974). These observations support the conjecture of Levy and Boudart that the similarity in catalytic properties is indeed due to electronic factors.

Subsequent investigations demonstrated that WC was good catalyst for a wide variety of reactions that typically utilized Pt as catalysts. Thus the use of WC as heterogeneous catalyst has grown. WC catalyzed reactions studied over the past 25

years include NH_3 synthesis (Sourabh *et al.*, 2007), ethylene hydrogenation (Morena-Castilla *et al.*, 2001), hydrazine decomposition (Rodrigues *et al.*, 1997), and CO hydrogenation (Patterson *et al.*, 2003).

2.6 Chlorofluorocarbons (CFCs)

Chlorofluorocarbons (CFCs) are a class of chemicals that contain only atoms of carbon, chlorine, and fluorine. They have many desirable properties such as inertness, stability and compressibility which make them ideal for many applications.

CFCs were first introduced in the 1930s as safe replacements for refrigerants and air-conditioners. Initially CCl_3F was used as a cooling medium in refrigerators while CCl_2F_2 in air-conditioners both stationary (room) and mobile (vehicles) ones. The popularity of Freons has increased when Abplanalp, the first to use CCl_2F_2 as propellants in spray cans containing deodorants and hair spray (Wayne, 2000). Later they were widely applied in technological sprays of paints, varnishes and pharmaceuticals (e.g. CF_3CClF_2). Intense development of technology has extended the use of halocarbons, e.g. in medicine for sterilisation of surgical instruments ($\text{CCl}_2\text{FCClF}_2$), and as blowing agents in the fabrication of flexible and rigid foams (CCl_3F , CCl_2F_2 , $\text{CCl}_2\text{FCClF}_2$) used for thermal insulation in building engineering. The compounds being excellent cleaning and fat removing agents have been commonly applied in the electronics industry ($\text{CCl}_2\text{FCClF}_2$, $\text{CClF}_2\text{CClF}_2$) and also as industrial solvents (CCl_4 , CHCl_3 , CH_3CCl_3 , CH_2Cl_2 , C_2Cl_4) (Wayne, 2000).

These widespread uses eventually resulted in large emissions of CFCs into the atmosphere and because of their low chemical reactivity, CFCs typically have long atmospheric residence times, and as a consequence are distributed globally. In 1974, Molina and Rowland hypothesized that when CFCs reached the stratosphere they would break down to release chlorine atoms. The chlorine atoms would then react with stratospheric ozone, breaking it down into oxygen (Wachowski *et al.*, 2001).

CFCs have been implicated in the accelerated depletion of ozone in the Earth's stratosphere. Since stratospheric ozone absorbs much of the sun's ultraviolet radiation, decreased stratospheric ozone levels could lead to increased ground-level ultraviolet radiation. This could adversely affect crop growth, and also lead to increases in cataracts and nonmelanoma skin cancer. Because of the harmful effects on mankind, CFCs have been classified as controlled and regulated substances in Montreal Protocol. According to the agreement, their production and usage was stopped immediately in the developed countries and by 2010 in developing countries. Therefore, more efforts in research and development are aimed at the development of CFC alternatives and also in the destruction or conversion of CFCs (UNEP, 2000).

2.6.1 Remediation and Conversion of CFCs

The banning of CFCs has led to research to identify other chemicals that can be used in the same applications but without the same environmental concerns. An ideal CFC substitute is one whose properties are close to that of existing CFC, with added specification that it does not destroy the ozone layer and therefore has a low global warming potential, low toxicity and a shorter atmospheric life time ensures that the molecule is degraded in the troposphere, leaving little chance for its entry into stratosphere. The presence of hydrogen in the molecule promotes attack by hydroxyl radicals in the atmosphere leading to more rapid breakdown and shorter atmospheric lifetimes. Thus hydrochlorofluorocarbons (HCFCs) with greatly reduced atmospheric life ranging from 2-25 years are acting as intermediates for the CFCs (Rao *et al.*, 2003). Hydrofluorocarbons (HFCs) with no chlorine atoms, even though they seem to be real substitutes for CFCs, are more difficult to synthesis than CFCs.

In addition to the development of CFC alternatives, it is also important to destroy the large quantities of existing CFCs in an efficient manner. The most widely used substances in CFC family are CFC-12 (refrigerant), CFC-11 (blowing agent),

and CFC-113 (cleaning agent). Because of their ozone depletion potential in the stratospheric ozone layer, in addition to development of their alternatives and methods to destroy existing CFCs need to be established.

There are several approaches to the remediation of CFCs. These include activated carbon adsorption, thermal incineration, catalytic oxidation and hydrodehalogenation (HDH). While treatment with activated carbon can aid in recovery and recycling of halogenated solvents, it is not a viable method for destruction of CFCs. Thermal incineration (≥ 900 °C) is successful at destroying halogenated organics; however, the presence of oxygen during the process can lead to the formation of even more toxic secondary pollutants such as polyhalogenated dioxins and furans (Soderstrom and Marklund, 2002). Emission from incineration plants are major contribution to the 3000 kg of polyhalogenated dioxins and furans produced every year (Brzuzy and Hites, 1996). Catalytic oxidation allows for the use of low temperature (< 600 °C), but current catalysts have relatively low activity (Corella and Toledo, 2002).

Hydrodehalogenation (HDH) of CFCs has been identified as a better process for their transformation as yield either HCFCs or HFCs that has low or almost zero ozone depletion potential (ODP) value. In this study catalytic HDH testing was carried out on CFC-12 using the prepared tungsten carbide catalyst.

2.6.2 Hydrodehalogenation of CFCs on tungsten carbide

Catalytic hydrodehalogenation of CFCs produces HCFCs and HFCs at lower temperatures (< 300 °C) and is the most promising of the remediation technique available (Oxley *et al.*, 2004). A typical reaction mechanism on the formation of CFC-12 (CH_2F_2) through HDH of CCl_2F_2 may be represented in the following way (Rao *et al.*, 2003).



S = catalyst support

(Eq.2.1) Dissociative adsorption of hydrogen over metal surface

(Eq.2.2) Metal halogen exchange between reactant and catalyst surface.

(Eq.2.3) Formation of difluorocarbene with hydrogen.

(Eq.2.4) Associative desorption of carbene with hydrogen.

However this reaction condition and nature of support influence the formation of HCFC-22 (CHClF_2) or methane in addition to HFC-32 (CH_2F_2). Thus depending on the condition, the reaction may further proceed as follows (Rao *et al.*, 2003):



Nature of support, $\text{H}_2/\text{CFC-12}$ ratio and the reaction temperature influence the selectivity to different products and also the catalyst stability. The commonly used supports for hydrodehalogenation are either neutral supports such as activated carbon and graphite or acidic supports such as AlO_3 and AlF_3 as they expected to offer better

resistance to corrosion reaction condition (evolution of HCl and HF) during course of the reaction.

Although previously Palladium, platinum and Rhodium has been the preferred catalyst for hydrodehalogenation of CFCs, transition metal carbides, especially Molybdenum (Mo) and tungsten (W) carbides are also well known to show interesting behaviors in HDH reaction. Indeed Delannoy *et al.*, (2000) have reported that tungsten and molybdenum carbides catalyse hydrodehalogenation CFC-115 ($\text{CF}_3\text{CF}_2\text{Cl}$). It was found that selectivity towards pentafluoroethane (HFC -125) decreases in the following sequence of: $\text{WC}_2 > \text{WC}_{1-x} > \text{MoC}_{1-x}$. In another study Oxley *et al.*, (2004) used sonochemically prepared Mo_2C and W_2C to perform catalytic HDH of several halogenated organic compounds including CFC-12. They noted that the both catalysts were selective, active and stable for all substrates tested. In this study catalytic HDH reaction was performed on tungsten carbide catalyst supported on activated carbon.

2.7 Preparation of Tungsten Carbide

High surface area tungsten carbide catalyst is known to possess catalytic properties similar to ruthenium, iridium, palladium and platinum. Conventional preparation methods for carbides have been inherited from the metallurgical industry and involve the reaction of metal compounds with graphite carbon at very high temperature (1600 °C). Abdul Rahim *et al.*, (2005); Ratna (2007) synthesis tungsten carbide by reacting tungsten powder and palm kernel base activated carbon via carburization under nitrogen and vacuum condition. But the resulting carbide give a very low surface area ($15 \text{ m}^2\text{g}^{-1}$) and unsuitable for use as catalyst. A high surface area is desirable for increasing the number of available catalytic sites. Many methods have been developed for the preparation of high surface area carbides in order to optimize the catalytic efficiency of the carbides (Toth, 1971). It is also found that the catalytic properties of carbide materials strongly depend on their surface structure and

composition, which are closely associated with the preparation methods. The representative method is the temperature programmed reaction between oxide precursors and a flow of hydrogen and carbon-containing gases, such as CH₄ (Keller *et al.*, 1991), C₂H₆ (Claridge *et al.*, 2000), C₄H₁₀ (Xiao *et al.*, 2000) and CO (Lemaitre *et al.*, 1986). However resulting carbide surface is usually contaminated by polymeric carbon from the pyrolysis of carbon-containing gases and the carbon blocks the pores, covers the active sites, and difficult to remove (Liang *et al.*, 2003).

In a study conducted by Alvarez-merino *et al.*(2000), high surface area tungsten carbide catalyst supported on activated carbon has been prepared via sublimation technique followed by heat treatment at moderate temperature. Ammonium tungstate and tungsten hexacarbonyl were used as metal precursors. The results showed that the carbide catalysts give a high surface area. It also found that the catalyst prepared from solid precursors (tungsten hexacarbonyl) showed greater proportion of tungsten carbide compare to liquid precursor (ammonium tungstate), which could be due to its greater dispersion favoring the transformation of tungsten trioxide into tungsten and tungsten carbide.

In this study tungsten carbide catalysts with different metal content were prepared using tungsten hexacarbonyl W(CO)₆ precursor, which was deposited on activated carbons prepared in laboratory from palm kernel shell. Since the starting materials for the production of these carbides are abundant and cheap, it is suggested that they can be potential substitute for the rare and expensive noble metals (Vicinisvarri *et al.*, 2006).

2.8 Fourier Transform Infrared (FTIR)

Infrared (IR) spectroscopy is the subset of spectroscopy that deals with the infrared region of the electromagnetic spectrum. Simply, it is the absorption measurement of different IR frequencies by a sample positioned in the path of an IR beam. The main objective of IR spectroscopic analysis is to determine the chemical functional groups in the sample. Different functional groups absorb characteristic frequencies of IR radiation. Using various sampling accessories, IR spectrometers can accept a wide range of sample types such as gases, liquids, and solids. Thus, IR spectroscopy is an important tool for structural elucidation and compound identification.

The IR portion of the electromagnetic spectrum is commonly divided into three regions; the near-IR, mid-IR, and far-IR, named for their relation to the visible spectrum. The far-IR, ($400\text{-}10\text{ cm}^{-1}$) has low energy and requires the use of specialized optical materials and sources. It is used for analysis of organic, inorganic, and organometallic compounds involving heavy atoms. It provides useful information to structural studies such as conformation and lattice dynamics of samples. The mid-IR ($4000\text{-}400\text{ cm}^{-1}$) is used to study the fundamental vibrations and associated rotational-vibrational structure, whilst the higher energy near-IR ($14000\text{-}4000\text{ cm}^{-1}$) can excite overtone or harmonic vibrations (Lange, 1985).

Molecular bonds vibrate at various frequencies depending on the elements and the type of bonds. For any given bond, there are several specific frequencies at which it can vibrate. The vibrational frequencies are determined by the shape of the molecular potential energy surface, the masses of the atoms and eventually by the associated vibronic coupling. For a molecule to show infrared absorptions, the electric dipole moment of the molecule must change during the vibration. This is the selection rule for infrared spectroscopy.

To measure a sample, a beam of IR light is passed through the sample and the amount of energy absorbed at each wavelength is recorded. Fourier transform IR (FTIR) spectroscopy is a measurement technique which measures all wavelengths at once compared to dispersive IR spectroscopy. Instead of recording the amount of energy absorbed when the frequency of IR light is varied (monochromator), the IR light is guided through an interferometer. After passing the sample, the measured signal is the

interferogram. Performing a mathematical Fourier transform on this signal, results in a transmittance or absorbance spectrum which shows at which wavelengths the sample absorbs the IR and allows an interpretation of which bonds are present (Lange, 1985).

Fourier Transform Infrared (FTIR) technique has brought significant practical advantages to infrared spectroscopy. FTIR spectrometers are cheaper than conventional spectrometers because building of interferometers is easier than fabrication of monochromator. In addition, measurement of a single spectrum is faster for the FTIR technique because the information at all frequencies is collected simultaneously. This allows multiple samples to be collected and averaged together resulting in an improvement in sensitivity.

2.9 Nitrogen Adsorption Analysis

Gas adsorption is commonly used in surface characterization. It allows one to determine the specific surface area, pore volume and pore size distribution as well as surface properties. Nitrogen gas is used for its nonpolar and inert criteria as it is adsorbed and desorbed on porous solids.

Figure 2.2 illustrates the gas sorption process. Before performing gas sorption, the solid adsorbent under investigation must first evacuate to *ca.* 10^{-4} Torr for several hours to remove contaminants such as water and oil. Figure 2.2 (a) shows a solid particle containing cracks and pores of different sizes and shapes after its pretreatment. Once clean, the sample is brought to constant temperature by means of external bath. Then, small amounts of a gas (the adsorbate) are admitted in steps into the evacuated sample chamber. Gas molecules that stick to the surface of the solid (adsorbent) are said to be adsorbed and tend to form a thin layer that covers the entire adsorbent surface (Figure 2.2 (b)). Based on the well-known Brunauer, Emmett and Teller (B.E.T.) theory, one can estimate the number of molecules required to cover the adsorbent surface with a monolayer of adsorbed molecules, N_m . Multiplying N_m by the

cross-sectional area of an adsorbate molecule yields the sample's surface area (Asiah and Noor Khaidawati, 2005). Figure 2.2 (c) shows that the continued addition of gas molecules beyond monolayer formation leads to the gradual stacking of multiple layers. The formation occurs in parallel to capillary condensation.

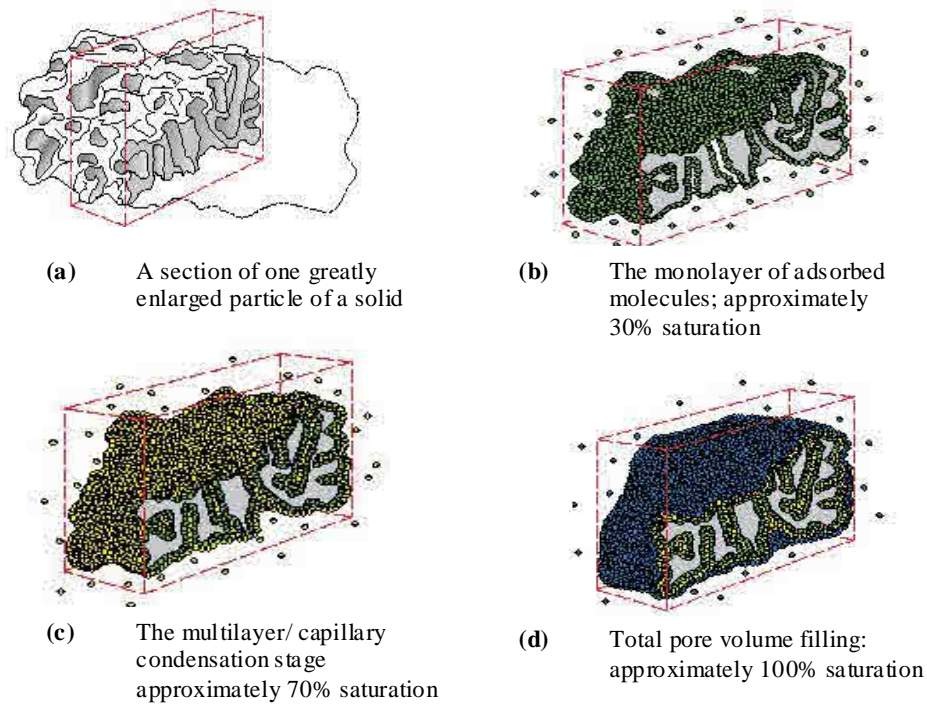


Figure 2.2: The gas sorption process

Methods such as the one by Barrett, Joyner and Halenda (B.J.H.) allow the computation of pore sizes from equilibrium gas pressures. One can therefore generate experimental curves (or isotherms) linking adsorbed gas volumes with relative saturation pressures at equilibrium, and convert them to cumulative or differential pore size distributions. As the equilibrium adsorbate pressures approach saturation, the pores become completely filled with adsorbate (see Figure 2.2 (d)). Knowing the density of the adsorbate, one can calculate the volume it occupies and, consequently, the total pore volume of the sample. If at this stage one reverses the adsorption process by withdrawing known amounts of gas from the system in steps, one can also generate desorption isotherms. The resulting hysteresis leads to isotherm

shapes that can be mechanistically related to those expected from particular pore shapes.

2.9.1 Adsorption Isotherms

An adsorption isotherm is the relation between the amount of gas adsorbed on a given surface at constant temperature and the pressure of the gas in equilibrium with it. The shape of adsorption isotherm reflects the adsorbent surface structure.

According to the BDDT classification proposed by Brunauer, Deming, Deming and Teller, there are five types isotherm shapes namely Type I, II, III, IV and V. The sixth isotherm, Type VI shape was discovered later. All six typical types of isotherm are illustrated in Figure 2.3.

Type I isotherms exhibit prominent adsorption at low relative pressures and then level off. It is usually considered to be indicative adsorption in micropores or monolayer adsorption due to adsorbate-adsorbent interactions. Type II and III isotherms refer the formation of multilayer on many macroporous solid in such a manner that the amount adsorbed gas increase gradually as the relative pressure increase. Type II and III were differentiate depending on the surface properties given solid. There maybe a pronounced stage of monolayer formation (Type II) that has monolayer coverage. Type III can be observed when lateral interaction between adsorbed molecules is strong in comparison to interaction between adsorbent surface and adsorbate due to incomplete monolayer coverage (Hussain, and Mohd Saiyudin, 2005).

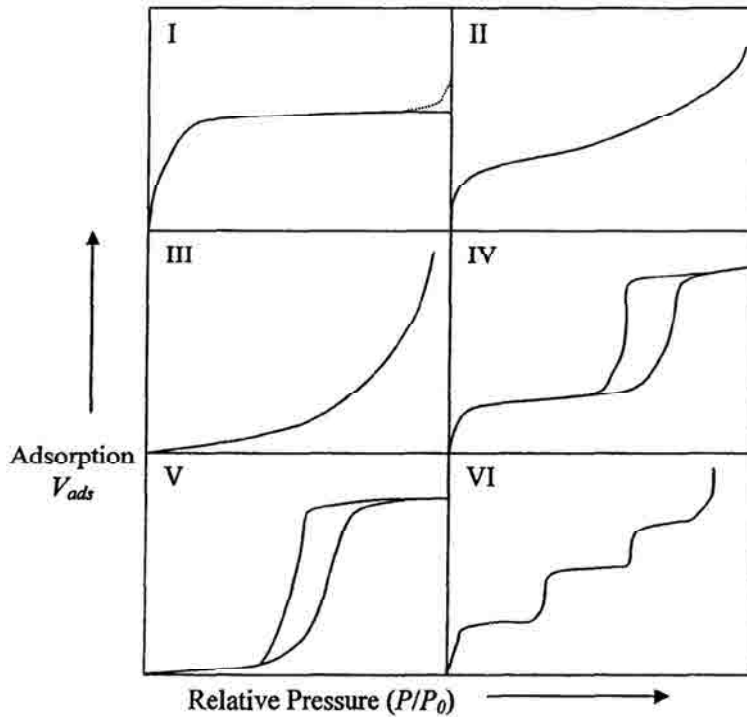


Figure 2.3: Types of BDDT physisorption isotherm

In Type IV and V isotherms, hysteresis loops are observed. The hysteresis loop indicates the presence of mesopores in the adsorbent. Type IV isotherm signifies a mesoporous material while Type V signifies a mixture of mesopores and macropores. Type VI isotherm indicates that the adsorbent surface contains few groups of energetically uniform sites. The stepped isotherm is the result of stepwise multilayer adsorption of gas molecules. However this behavior is rather rare in the study of activated carbon.

2.9.2 Brunauer, Emmett and Teller (BET) Surface Area

The data of nitrogen adsorption is very useful in the determination of the Brunauer, Emmett and Teller (BET) Surface Area (S_{BET}) of the sample. The graph of the adsorption data is plotted using BET equation (Eq.2.10).

$$\frac{P}{V(P_0 - P)} = \frac{1}{V_m C} + \frac{(C - 1) P}{V_m C P_0} \quad (\text{Eq.2.10})$$

where;

P = equilibrium pressure of nitrogen gas

P_0 = saturation pressure of nitrogen gas

V = volume of nitrogen adsorbed at pressure P

V_m = volume adsorbed when the entire surface is covered with monolayer of nitrogen molecules

C = BET constant

A plot of $P / V(P_0 - P)$ against P/P_0 will result in a straight line. By using the value of the slope (s) and intercept (i), we can calculate the value of V_m , using Eq.2.11

$$V_m = \frac{1}{s + i} \quad (\text{Eq.2.11})$$

The value of V_m can then be used to calculate the value of BET surface area (S_{BET}), Eq.2.12

$$S_{BET} = \frac{V_m}{22414} \times A_m \times N_0 \quad (\text{Eq.2.12})$$

where;

A_m = average area of one adsorbate molecule in the complete monolayer

N_0 = Avogadro number

When nitrogen is used as adsorbate, the value of A_m is $16.2 \times 10^{-20} \text{ m}^2$. By substituting the value of A_m and N_0 into Eq.2.12, we can get a simplified equation, Eq.2.13, which can be used to determine the BET surface area of the sample.

$$S_{BET} = 4.35 \times V_m \quad (\text{Eq.2.13})$$

2.9.3 The t -plot

To determine the micropore volume and micropore surface area, the method of t -plot is frequently used. In t -plot analysis method, the quantity of nitrogen adsorbed is plotted against the statistical thickness of the adsorbed film, t . Harkins- Jura equation (Eq.2.14) is used to produce the t - plot.

$$t (\text{\AA}) = \left[\frac{13.99}{0.0340 - \log P / P_0} \right]^{1/2} \quad (\text{Eq.2.14})$$

The intercept, i , of the t -plot graph can be converted to liquid volume to give the micropore volume, V_{MP} (Eq.2.15). The constant 0.001547 tells the conversion factor of nitrogen gas volume to liquid.

$$V_{MP} = i \times 0.001547 (\text{cm}^3 \text{ g}^{-1}) \quad (\text{Eq.2.15})$$

The gradient, s , of the straight line within the range of 3.5-6.0 Å gives the external surface area, S_{ext} (Eq.2.16).

$$S_{ext} = s \times 15.47(m^2 g^{-1}) \quad (\text{Eq.2.16})$$

The micropore surface area, S_{MP} is the difference between S_{BET} and S_{ext} (Eq.2.17).

$$S_{MP} = S_{BET} - S_{ext} \quad (\text{Eq.2.17})$$

2.10 Thermogravimetry Analysis (TGA)

Thermogravimetry is an analytical technique in which the mass (weight) of sample is monitored versus time or temperature while the temperature of sample is programmed under certain atmosphere. The result of detection is presented graphically as a plot of weight % versus time or temperature. Such plot is known as thermogram. From the thermogram, we are able to determine the step of reaction when sample undergoes heating, the thermal stability, the temperature at which certain reaction takes place. In this study, TGA is important in determining the optimum activation temperature for the production of activated carbon, and also to ensure that the conversion of palm kernel shell to activated carbon is complete.

The essential components of the equipment used are a recording balance, furnace, temperature programmer, sample holder, an enclosure for establishing the required atmosphere, and a means of recording and displaying the data.

Balance sensitivity is usually around one microgram, with a total capacity of a few hundred milligrams. A typical operating range for the furnace is ambient to

1000°C, with heating rates up to 100°C/min. The quality of the furnace atmosphere deserves careful attention, particularly the ability to establish an inert (oxygen-free) atmosphere, and it is useful to be able to quickly change the nature of the atmosphere. Compatibility between the materials of construction and the sample and its decomposition products, and the gaseous atmosphere, must be considered. Sample holder materials commonly available include aluminium, platinum, silica, and alumina.

Indication of the sample temperature is by a thermocouple close to the sample. Careful calibration for temperature is important, especially for kinetic studies. Various means are available for temperature calibration, which is not a trivial matter, though reproducibility is often more important than absolute accuracy. Weight calibration is readily achieved using standard weights (Heal and Haines, 2002)

Many factors influence the form of the TG curve, both sample and instrument related, some of which are interactive. The primary factors are heating rate and sample size, an increase in either of which tends to increase the temperature at which sample decomposition occurs, and to decrease the resolution between successive mass losses. The particle size of the sample material, the way in which it is packed, the crucible shape, and the gas flow rate can also affect the progress of the reaction. Careful attention to consistency in experimental details normally results in good repeatability. On the other hand, studying the effect of deliberate alterations in such factors as the heating rate can give valuable insights into the nature of the observed reactions.

2.11 Field Emission Scanning Electron Microscopy (FESEM) and Energy Dispersive X-ray Spectroscopy (EDX)

The Field Emission Scanning Electron Microscopy (FESEM) is a versatile, non-destructive technique that reveals detailed information about the morphology and particle sizes. It can produce images of sample surface up to 1000x and even 10000x magnification (Bertin, 1975).

When the electrons are liberated from a field emission source and accelerated in a high electrical field gradient. Within the high vacuum column these so-called primary electrons are focused and deflected by electronic lenses to produce a narrow scan beam that bombards the object. As a result secondary electrons are emitted from each spot on the object. The angle and velocity of these secondary electrons relates to the surface structure of the object (Oatley, 1972). A detector catches the secondary electrons and produces an electronic signal. This signal is amplified and transformed to a video scan-image that can be seen on a monitor or to a digital image that can be saved and processed further.

Another analysis that can be carried out by emitting beams of electrons is the Electron Dispersive X-ray analysis (EDX). It is a spectroscopic technique that enables us to determine the main composition of a sample. In an EDX, an X-ray beam is emitted to the surface of sample. The interaction of X-ray with the surface electrons produces X-ray lines with different photon energies. The principal of EDX is the separation of X-ray lines based on their photon energies (Bertin, 1975). Since the photon energies of X-ray lines produced are characteristics of the elements, we can determine the main composition of element in the sample.

2.12 X-ray Powder Diffraction (XRD)

X-ray powder diffraction is a non-destructive technique widely applied for the characterization of crystalline materials. It also has been traditionally used for phase identification, quantitative analysis and the determination of structure imperfections. X-rays are relatively short-wavelength, high-energy beams of electromagnetic radiation (Perego, 1998). They are sufficiently energetic to penetrate solids and suitable to probe their internal structure. XRD is the elastic scattering of x-ray photons by atoms in periodic lattice.

XRD uses single or multiphase specimens comprising a random orientation of small crystallites. Each crystallite in turn is made up of a regular, ordered array of crystal lattice. An ordered arrangement of the crystal lattice contains planes of high electron density. A monochromatic beam of X-ray photons will be scattered by these atomic electrons and when the scattered photons interfere with each other, diffraction will occur. Figure 2.4 illustrates diffraction of x-ray by crystal lattice. In general, one diffracted line will occur for each unique set of plane in the lattice. In a diffraction pattern from the crystal lattice, a number of reflections are generated, each one being associated to a lattice plane, and occurring at an angular position (2θ), depended on the related interplanar spacing, d and on x-ray wavelength (λ) in Bragg's Law (Equation 2.18)

$$n\lambda = 2d \sin \theta \quad (n = 1,2,3..) \quad (\text{Eq.2.18})$$

Where:

n = the order of the diffracted beam

λ = wavelength of the incident X-ray beam

d = distance between 2 lattice planes

θ = angle of the incident X-ray beam

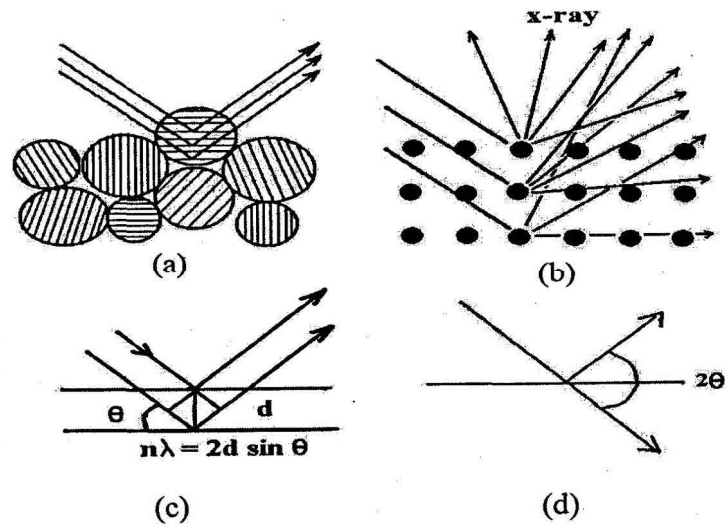


Figure 2.4: X-ray scattered by atoms in an ordered lattice interfere constructively in direction given by Bragg's Law (Richardson, 1989)

A diffraction pattern is typically in the form of a graph of diffraction angle (interplanar) spacing against diffracted line intensity. Each of these unique patterns can act as an empirical ‘‘fingerprint’’ for the identification of the various phases, using pattern recognition techniques based on a file of standard single-phase patterns.

Besides that diffraction patterns also used to identify the crystallographic phases that are presence in the sample and which are shown by a sharp and narrow diffraction lines. Basically for the amorphous phases, XRD gives either very broad and weak diffraction or no diffraction at while crystalline phases gave sharp and strong lines.

2.13 Gas Chromatography (GC)

In general, chromatography is a term that describes techniques used to separate components of mixtures. Gas chromatography is a type of chromatography in which the mobile phase is a carrier gas, usually an inert or an unreactive gas, and the stationary phase is a microscopic layer of liquid or polymer on an inert solid support, inside glass or metal tubing, called a column (Scott and Perry, 1998).

A gas chromatograph is a chemical analysis instrument for separating chemicals in complex sample. a gas chromatograph uses a flow-through narrow tube known as the column, through which different chemical constituents of sample pass in a gas stream (carrier gas, mobile phase) at different rates depending on their various chemical and physical properties and their interaction with specific column filling, called the stationary phase. As the chemicals exit the end of the column, they are detected and identified electronically. The function of the stationary phase in the column is to separate different components, causing each one to exit the column at a different time (retention time). Other parameters that can be used alter the order or the retention is the carrier gas flow rate, and the temperature.

Basically, a gas chromatograph consists of a flowing mobile phase, an injection port, a separation column containing the stationary phase, a detector, and a data recording system. Figure 2.5 shows the diagram of a gas chromatograph. The carrier gas (mobile phase) must be chemically inert. Commonly used gases include nitrogen, helium, argon, and carbon dioxide. The choice of carrier gas is often dependant upon the type of detector which is used. The carrier gas system also contains a molecular sieve to remove water and other impurities.

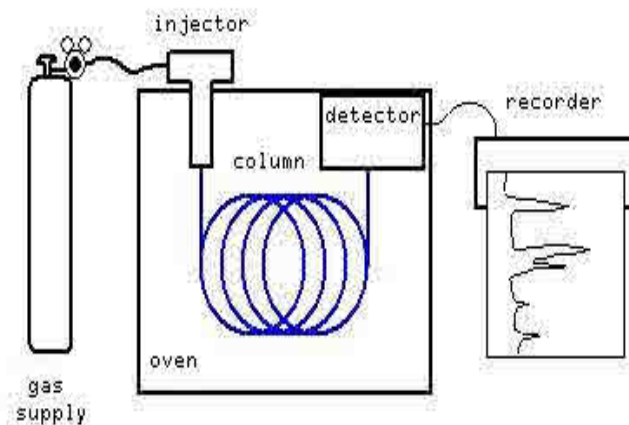


Figure 2.5: Diagram of a gas chromatograph

The most common injection method is where a microsyringe is used to inject sample through a rubber septum into a flash vapouriser port at the head of the column. The temperature of the sample port is usually about 50 °C higher than the boiling point of the least volatile component of the sample.

Generally there are two types of column, packed column and capillary column. Packed columns contain a finely divided, inert, solid support material coated with liquid stationary phase. Most packed columns are 1.5–10 m in length and have an internal diameter of 2–4 mm. On the other hand capillary columns have an internal diameter of a few tenths of a millimeter.

A number of detectors are used in gas chromatograph. The most common are the flame ionization detector (FID) and the thermal conductivity detector (TCD). Both are sensitive to wide range of components and both work over a wide range of concentrations. While TCDs are essentially universal and can be used to detect any component other than carrier gas, FIDs are sensitive primarily to hydrocarbons and are more sensitive to them than TCD. However, an FID cannot detect water. Both detectors are quite robust. Since TCD is non-destructive, it can be operated in-series before an FID (destructive), thus providing complementary detection of the same eluents (Scott and Perry, 1998).

CHAPTER 3

EXPERIMENTAL

3.1 Instrumentations

The physical characterization of the prepared activated carbons and tungsten carbide catalysts were carried out using FTIR, Nitrogen adsorption analysis, single point BET, FESEM, TGA, XRD and EDX. The hydrodehalogenation reaction of CFC-12 was analyzed using gas chromatography.

Fourier Transform Infrared (FTIR) analysis was done using Shimadzu 8300 spectrometer. The samples were well mixed with potassium bromide in 1:100 ratios, and compressed under pressure of 7 tonnes for about 5 minutes in order to form a thin transparent pallet. The FTIR spectra were recorded in a range of 4000–400 cm^{-1} .

The adsorption isotherms and data were recorded using the Micromeritics ASAP 2010. In the nitrogen adsorption analysis, dry gas nitrogen was flowed through the sample. The volume of nitrogen adsorbed on the sample at 77 K was monitored versus the gas pressure. The result was presented as an isotherm, which is a plot of volume of gas adsorbed (V_{ads}) versus relative pressure (P/P_0). From the shape of the isotherm, the type, shape and size of pores in the sample were determined.

The single point Brunauer-Emmet Teller (BET) surface area of the sample was measured at 77 K using Micromeritics Pulse Chemisorb 2705. Sample was degassed at 150°C for an hour for eliminate impurities as well as for dehydration purpose. The adsorption and desorption process were carried out for few times until constant values were obtained and the specific surface area of the sample was calculated.

The thermogram was obtained using Mettler-Toledo TG50 Analyzer. The sample was placed in a ceramic crucible in the TG analyzer. Then the sample was heated from 40°C with the rate of 10°C per minutes with nitrogen gas flow to ensure inert atmosphere.

The surface morphology and element composition of the sample was analyzed using FESEM 6701F microscope with energy of 15.0 V couple with EDX analyzer. The grounded sample was sputtered on aluminium stub that covered with carbon cement tape. The stub was place into the vacuum chamber of FESEM instrument. The morphology scanning was done in different magnification to obtain clear images.

The phase and identification of the tungsten carbide catalysts were carried out using Bruker X-ray powder diffractometer. The XRD diffractograms were recorded with $\text{CuK}\alpha$ radiation source with $\lambda = 0.15418$ nm at 40 kV and 30 mA. The 2θ range used was from 20° to 90° at a scanning speed of 0.05 per second. The identification of peaks is based on JCPDS-ICDD database incorporated in the software.

Gas chromatography of hydrodehalogenation of CFC was recorded using a Hewlett Packed model 5890. Helium gas was used as the mobile phase and column Inowax with (Polyethylene glycol) 0.25 μm thickness, 30 m length and 0.20 mm internal diameter was used as stationary phase with flame ionized detector (FID). The column was operated from 40°C up to 150°C with the rate 5°C/min.

3.2 Chemicals

Tungsten hexacabonyl, $W(CO)_6$ powders (98%) and commercial activated carbon (99.9%) with molecular weight of 351.90 gmol^{-1} and 12.01 gmol^{-1} respectively were purchased from Scharlau Chemise S.A. Zinc chloride ($ZnCl_2$) and sodium carbonate (Na_2CO_3) from MERCK were used along with concentrated hydrochloric acid (HCl), 37% w/w and concentrated sulfuric acid (H_2SO_4) 99% w/w. Dichlorodifflouromethane (CFC-12) was purchased from Zar Air-Conditioning Engineering. Nitrogen, hydrogen and helium gases used were supplied by Malaysian Oxygen Bhd. The palm kernel shells were obtained from Kulai palm oil mill.

3.3 Preparation of Activated Carbon

3.3.1 Preparation of Raw Material

The palm kernel shells collected from Kulai palm oil mill were washed with tap water repeatedly to remove the impurities and dried under the sunlight. The dried palm kernel shells were grinded using a mechanical grinder and then the particles were sieved to selected particle sizes of 1.18-2.36 mm. The particles were soaked in aqueous solution of 30% sulphuric acid for period of 24 hours. Finally the particles were thoroughly washed with distilled water to remove acid and dried under sunlight to eliminate moisture. The washing process with acid was termed as pretreatment.

3.3.2 Chemical Activation

Zinc chloride was dissolved in 100 ml of concentrated hydrochloric acid (37% w/w) and 150 mL deionized water and then impregnated into the palm kernel shells for the ratio of 1:1 and 2:1. The mixture was stirred and heated at 100-110°C on a hot plate until it is fully dried. The resulting chemically treated char was then kept in an oven overnight for dehydration purpose. The activation was carried out in two different conditions separately. Flow diagram for the preparation of activated carbon is shown in Figure 3.1

Prior to activation, the tube furnace was purged with nitrogen gas flow. The treated char was placed in a quartz tube and heated in nitrogen gas flow up to 700°C for 2 hours. When the process of activation accomplished, the prepared activated carbon was undergo washing process. First, the sample was neutralized with diluted Na_2CO_3 solution and deionized water in order to remove zinc chloride. Then the samples were washed with 2N HCl solution for 12 hours under reflux with aim of removing sulphur and some ash and washed with distilled water reflux for 6 hours. Sample was then dehydrated in oven at 100°C overnight. The sample obtained labelled as AC-1Z-N and AC-2Z-N.

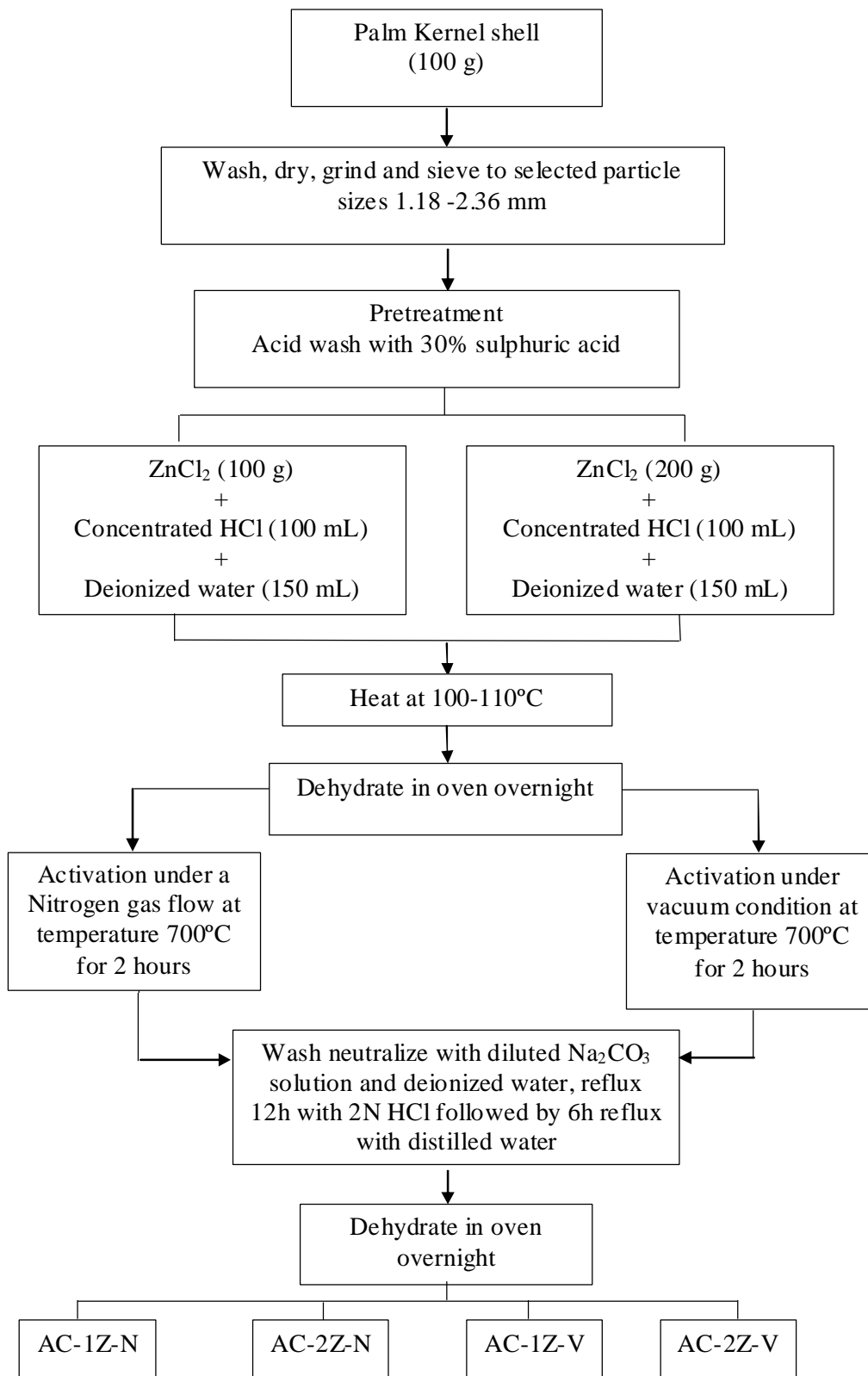


Figure 3.1: Flow diagram for the preparation of activated carbon.

As for the second activation condition about 0.5 g of treated char was placed in a quartz tube and connected to a vacuum line system. The schematic diagram of the vacuum line system used for activation under vacuum condition is as shown in Figure 3.2. The sample was heated at 700°C about 2 hours under 1×10^{-3} mbar pressure and followed by washing process. The washing process was done in the same manner as the preparation of AC-1Z-N and AC-2Z-N. The resulting sample labelled as AC-1Z-V and AC-2Z-V.

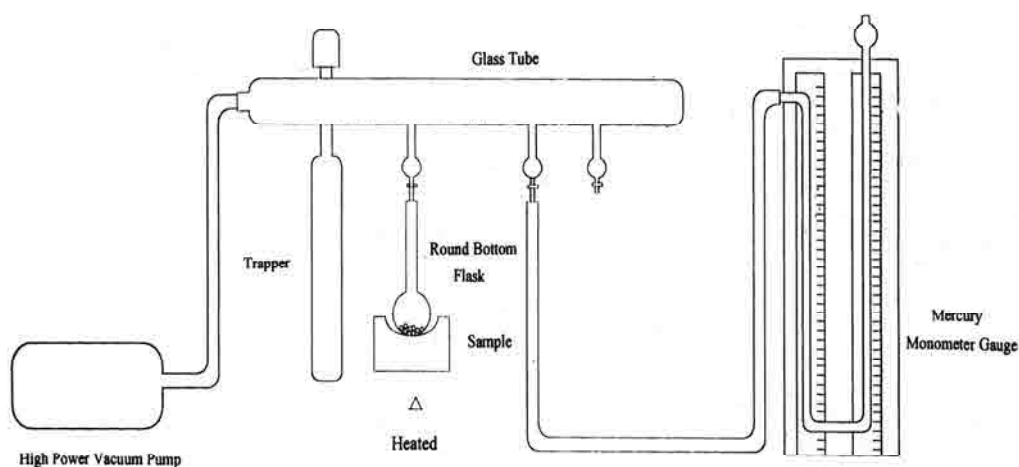


Figure 3.2: Schematic diagram of vacuum line system.

3.4 Preparation of Tungsten Carbide

There are few common methods used to prepare tungsten carbide catalyst and most used involved reaction of solid precursor, either as metal or oxide with gas phase containing reducing agent or carbonizing agent. In this research tungsten carbide catalyst was prepared without using any reducing agent. The catalyst was prepared

using tungsten hexacarbonyl and activated carbon as precursors. It is found to be a suitable method to prepared high surface area catalyst (Morena-Castilla *et al.*, 2001).

The percentage of tungsten content used for the catalyst mixture are 6 and 15 percent, whereby the weight was calculated by atomic ratio of the elements (refer Appendix 1.0). Table 3.1 shows the notation for tungsten carbide catalyst produced.

Table 3.1: Notation for tungsten carbide catalyst produced.

Notation	Type of carbon	Tungsten content (%)	Temperature of heat treatment
ACN-6-700	AC-1Z-N	6	700
ACN-15-700	AC-1Z-N	15	700
ACV-6-700	AC-1Z-V	6	700
ACV-15-700	AC-1Z-V	15	700
ACN-6-950	AC-1Z-N	6	950
ACN-15-950	AC-1Z-N	15	950
ACV-6-950	AC-1Z-V	6	950
ACV-15-950	AC-1Z-V	15	950

In preparing the catalyst, tungsten hexacarbonyl powder was mixed with the appropriate amount of activated carbon. The prepared sample was put together with stainless steel balls (20mm in diameter) in a stainless steel container, and sealed under argon atmosphere. This closed container mechanically rotated for about 2 hours using high energy ball mill, Fritsch Pulverisette 6 at a rotation speed of 200 rpm to force the carbonyl to sublime evenly onto the activated carbon.

Finally the catalyst was heated in a tube furnace. Prior to heat treatment, the furnace was purged with Helium gas to ensure the system is in inert condition. The sample was placed in a porcelain boat and an open ended quartz tube was used to support the sample boat in the furnace. The sample was heated in Helium gas flow at

700 and 950°C at the heating rate 10°C/min for period of 4 hours. Figure 3.3 shows the schematic set-up used for heat-treatment of tungsten carbide catalyst.

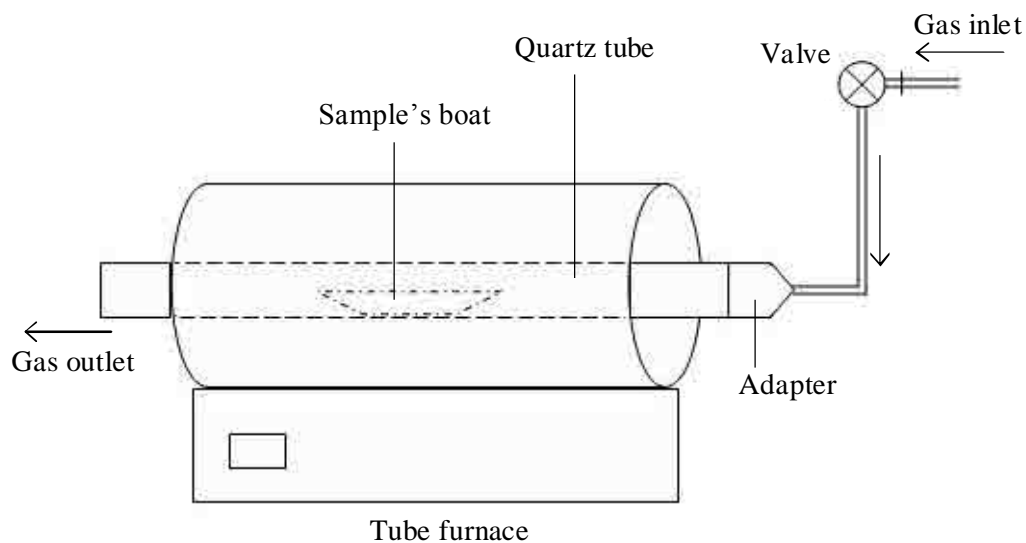


Figure 3.3: Schematic set-up used for heat-treatment of tungsten carbide catalyst.

3.5 Sample Characterization

3.5.1 Characterization of Activated Carbon

All the activated carbon samples were characterized using Fourier transform infrared (FTIR), single point BET surface area analysis, nitrogen adsorption analysis, Thermogravimetry analysis, (TGA), Field Emission scanning Electron Microscopy (FESEM) and Energy Dispersive X-ray analysis (EDX).

3.5.2 Characterization of Tungsten Carbide

Prepared catalysts were studied by various characterization techniques in order to learn about the physical properties. The outcome will be useful to determine the catalyst performance and potential in hydrodehalogenation catalytic reaction. All the tungsten carbide catalysts were characterized using X-ray diffraction, Field Emission Scanning Electron Microscopy (FESEM), and single point BET surface area analysis.

3.6 Catalytic Testing–Hydrodehalogenation reaction of dichlorodifluoromethane

Prior to the catalytic reaction, the prepared catalyst was reduced in hydrogen gas flow ($25 \text{ cm}^3/\text{min}$) using a tube furnace. The catalyst was heated at 400°C at the rate of $8^\circ\text{C}/\text{min}$ and hold at 400°C for 3 hours.

Then about 1 g of the reduced catalyst was placed in the glass micro reactor. The hydrodehalogenation reaction of dichlorodifluoromethane (CFC-12) was conducted in a glass flow system at temperature ranging from 200 to 350°C . The schematic set-up for the hydrodehalogenation catalytic reaction is shown in Figure 3.4. The flow of CFC-12 and hydrogen gas was metered using a flow controller at the rate of $2.5 \text{ cm}^3/\text{min}$ and $25 \text{ cm}^3/\text{min}$ respectively.

The composition of the product evolved at the reactor outlet was collected in gas collector and were analyzed using gas chromatography with FID detector and inowax column.

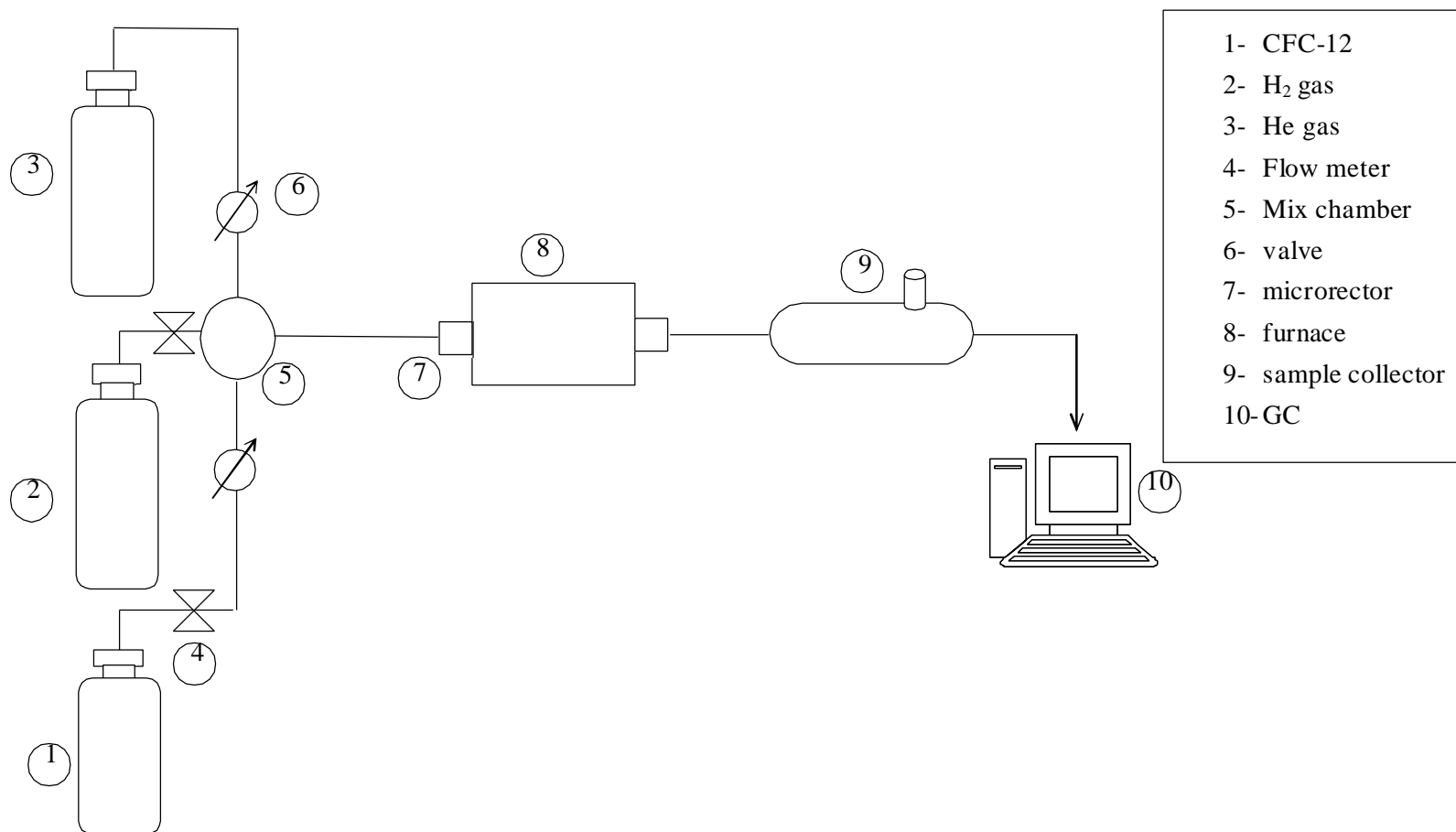


Figure 3.4: Schematic set-up for hydrodehalogenation catalytic reaction

CHAPTER 4

RESULTS AND DISCUSSION

3.2 General

The results in this study are divided into three parts. The first being the results of the characterization of activated carbon followed by the characterization of tungsten carbide catalyst. The last part is on the catalytic testing of tungsten carbide catalyst for the hydrodehalogenation of dichlorodifluoromethane (CCl_2F_2 , CFC-12).

4.2 Characterization of activated carbons

Four types of activated carbon were prepared from palm kernel shell by chemical activation using ZnCl_2 under both nitrogen and vacuum conditions. The activation process was carried out at different impregnation ratio (i.e. ZnCl_2 to palm kernel shell mass ratio). The activated carbons prepared were labelled as in Table 4.1.

Table 4.1: Sample notation for activated carbon

Notation	Description
com-AC	Commercial activated carbon
AC-1Z-N	Activated under nitrogen flow with impregnation ratio of 1:1
AC-2Z-N	Activated under nitrogen flow with impregnation ratio of 2:1
AC-1Z-V	Activated under vacuum condition with impregnation ratio of 1:1
AC-2Z-V	Activated under vacuum condition with impregnation ratio of 2:1

4.2.1 Fourier transform infrared spectroscopy

Analysis using FTIR helps to identify the presence of functional groups in the raw palm kernel shell and the activated carbon. This technique provides information on the effect of the activation process that has been carried out and also provides evidence of the phase transformation occurred after the activation.

Figure 4.1 shows the spectra of raw palm kernel shell (raw-PKS), commercial activated carbon (com-AC), and samples activated in vacuum condition, AC-1Z-V and AC-2Z-V. Figure 4.2 shows the raw-PKS and com-AC spectra along with samples activated in nitrogen gas flow, AC-1Z-N and AC-2Z-N.

From the combined spectra on both Figure 4.1 and 4.2, it can be observed that the FTIR spectrum of raw-PKS shows many peaks belonging to different functional groups. This spectrum is quite similar to that of pistachio-nut (Lua and Yang, 2005), which is a type of lignocellulosic material. Lignocellulosic materials are biomass composed primarily of lignin and cellulose. Agricultural residues such as palm kernel shell, trees and grasses are examples of lignocellulosic biomass.

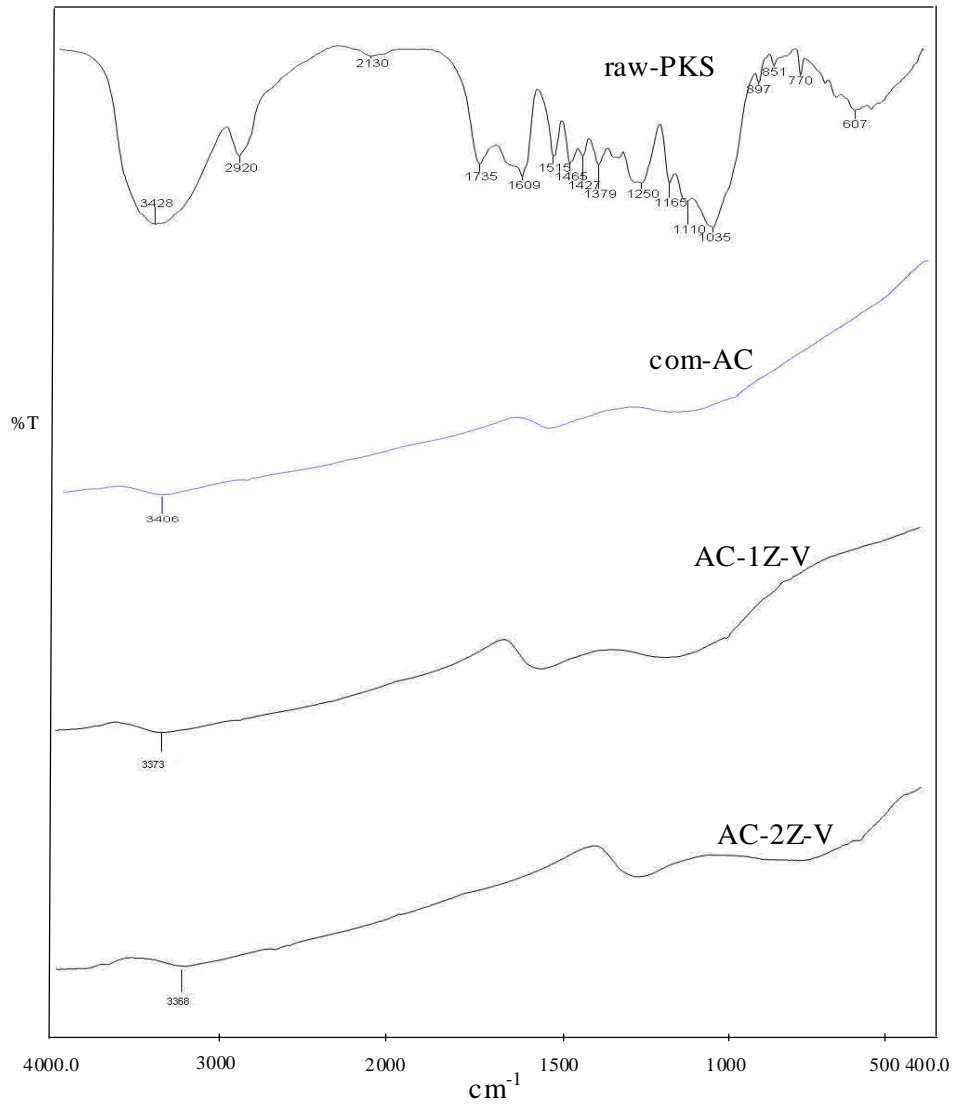


Figure 4.1: FTIR spectra of raw palm kernel shell, commercial activated carbon and samples activated in vacuum condition

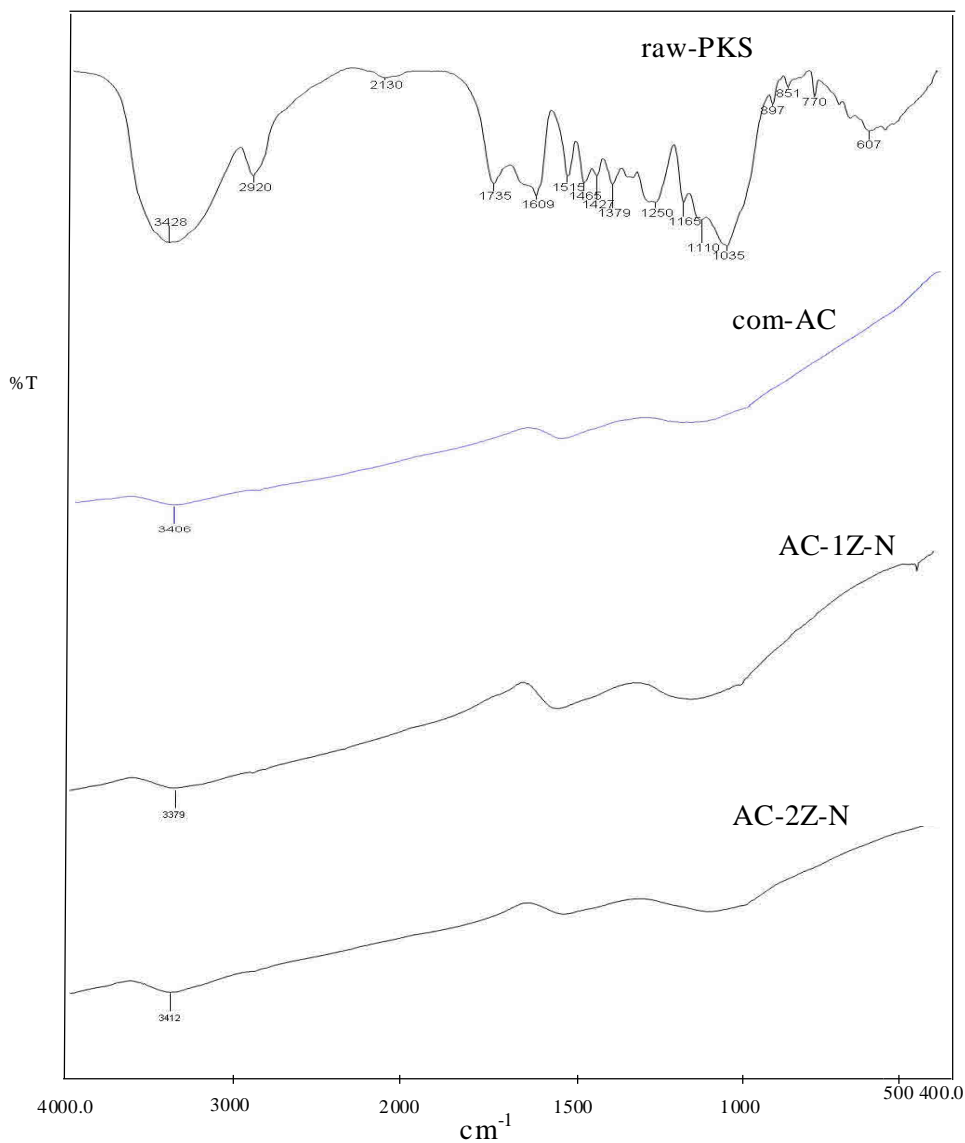


Figure 4.2: FTIR spectra of raw palm kernel shell, commercial activated carbon and samples activated in nitrogen flow

In the raw-PKS spectrum the strong peak appeared at 3428 cm^{-1} and is related to the hydroxyl group. Usually, the location of the hydrogen-bonded OH groups in the range of 3200-3650 cm^{-1} is assigned to alcohols and phenols (Stuart, 2004.). The band located at 2920 cm^{-1} corresponds to the C-H sp^3 stretching in the methyl and methylene groups. This band is contrary to C-H vibrations bands for $-\text{CH}_3-$ and

$-\text{CH}_2=$, which are located around 1379 cm^{-1} and 1465 cm^{-1} , and is very useful in identifying the methyl and methylene groups. While the presence of weak band at 2130 cm^{-1} is attributed to $\text{C}\equiv\text{C}$ vibrations in the alkyne groups. Another peak is observed at 1735 cm^{-1} which represents the stretching of $(\text{C}=\text{O})$ carbonyl groups. The raw-PKS spectrum also reveals a band at 1609 cm^{-1} , 1515 cm^{-1} and 1427 cm^{-1} corresponding to the stretching of $\text{C}=\text{C}$ in aromatic compounds. A peak at 1250 cm^{-1} and a subsequent small rise at 1165 cm^{-1} could be assigned to the stretching of $\text{C}-\text{O}$ in esters, ethers or phenol groups. A small shoulder at 1110 cm^{-1} and a relatively intense band at 1035 cm^{-1} could be attributed to the $(\text{R}-\text{OH})$ alcohol groups. From the analysis, it can be suggested that the main oxygen groups present in the raw-PKS are carbonyl groups, ethers, esters, alcohols and the phenol groups.

Unlike the spectrum showed by raw-PKS, spectra for all the prepared activated carbons, AC-1Z-V, AC-2Z-V, AC-1Z-N and AC-2Z-N illustrate less adsorption peaks. During the carbonization process most of the functional group elements were removed by pyrolytic decomposition of the raw-PKS, and the carbonized product was formed, having a structure more or less disordered elementary graphite-like crystallites with poorly developed porous structure. During the activation process the spaces between elementary crystallites become cleared of less organized carbonaceous compounds and at the same time, carbon is also removed (Mowla *et al.*, 2003). In addition, acid washing would result in the decomposition of some carbonyl groups and the subsequent release of their by-products as volatile matter, remaining activated carbon with different properties than the parent biomass material (Lua and Yang, 2005).

Basically all the samples showed weak and broad peaks around $3350\text{--}3450\text{ cm}^{-1}$ belonging to the hydroxyl groups. The intensity of the peak decreases with the formation of activated carbon, suggesting the expected loss of hydroxyl groups through volatilization during the activation process. Although the samples were prepared with different chemical ratio in nitrogen gas flow and vacuum condition there was a similarity in the absorption patterns.

Both figures show apparent decrease in the broad $\text{C}-\text{O}$ peak around $1000\text{--}1300\text{ cm}^{-1}$ and $\text{C}=\text{C}$ adsorption band around $1500\text{--}1650\text{ cm}^{-1}$. This is another evidence

of functionality loss in activated carbon samples. The spectra for prepared activated carbon and commercial activated carbon showed a great similarity. Table 4.2 summarized the vibration wave number data incorporating functional groups from the FTIR spectrum of raw-PKS.

Table 4.2: Vibration wavenumber and functional groups of the samples.

Sample	Peak (cm ⁻¹)	Functional group
raw-PKS	3428	O—H stretching
	2920	C—H (sp ³) stretching
	2130	C≡C stretching
	1735	C=O stretching
	1609, 1515 and 1427	C=C stretching (aromatic)
	1379 and 1465	C—H bending (-CH ₃ and -CH ₂)
	1250 and 1165	C— O Stretching (esters, ethers or phenol groups)
	1110 and 1035	C— O stretching (alcohol groups)
	897, 851, 770 and 607	C—H out of plane bending in benzene derivative
	AC-1Z-V	3368
AC-2Z-V	3373	O—H stretching
AC-1Z-N	3412	O—H stretching
AC-2Z-N	3379	O—H stretching

4.2.2 Nitrogen adsorption analysis

Nitrogen adsorption analysis was carried out to study the effect of impregnation ratio (ZnCl₂ to palm kernel shell) and the activation condition on the texture of activated carbon. The textural properties of the all prepared activated carbon namely AC-1Z-N, AC-1Z-V, AC-2Z-N and AC-2Z-V were measured using Micrometric ASAP 2010 apparatus by means of nitrogen adsorption at 77 K. From the analysis, the BET single point surface area of all the prepared activated carbons was determined. The BDDT adsorption isotherm and pore size distribution plot were used to evaluate the porosity of the activated carbon. In addition, empirical *t*-plot was applied to nitrogen adsorption isotherms to obtained more information about the pore

texture.

4.2.2.1 Single point BET surface area

The single point BET surface area analysis at temperature of 77 K was performed to determine the surface area. All the data collected, including the raw-PKS are presented in the form of a bar chart in Figure 4.3.

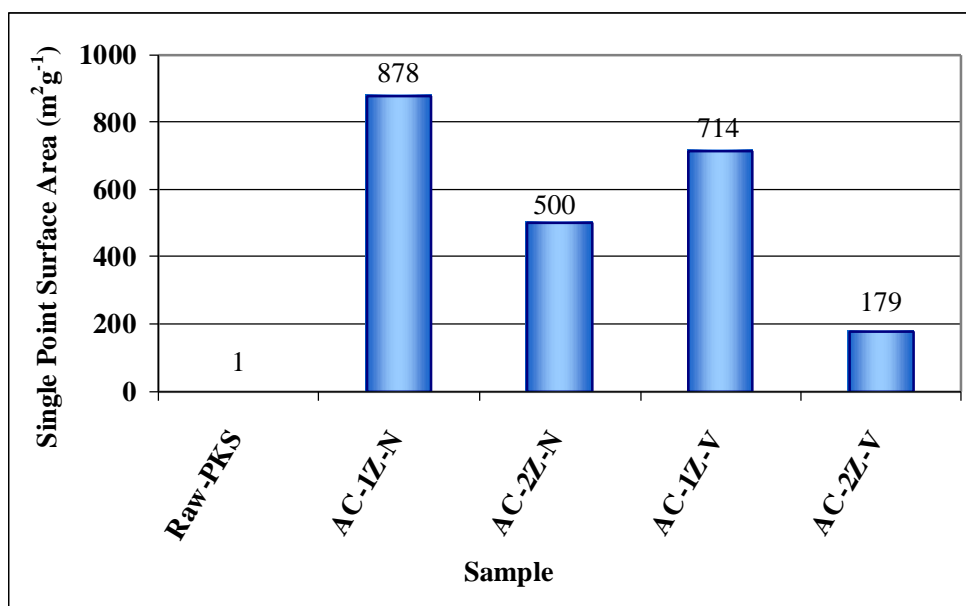


Figure 4.3: Single point BET surface area of raw-PKS and prepared activated carbons.

The result showed that initially the surface area of the raw-PKS is 1 m²g⁻¹. However after the activation process the surface area of all the activated carbons increased drastically and exhibited extensively higher surface area than the raw-PKS. The highest surface area was obtained in AC-1Z-N with 878 m²g⁻¹ followed by AC-1Z-V with 714 m²g⁻¹. The AC-2Z-N exhibits moderate surface area of 500 m²g⁻¹. Among the prepared activated carbon AC-2Z-V has the lowest surface area of 179 m²g⁻¹, which is not in the range of activated carbon surface area. Typically, the surface area of an activated carbon ranged from 400 – 1500 m²g⁻¹ (Knozinger *et al.*,

1999).

From the results obtained, the activated carbon prepared with impregnation ratio (ZnCl_2 to palm kernel shell) of 1:1 gave significantly higher surface area. These results strongly suggest that the chemical activating agent ZnCl_2 has contributed to the increase in the surface area by creating new pores and enlarging the diameter of existing pores. However, the surface area of the activated carbon decreases when the impregnation ratio increases to 2:1. When the chemical ratio increases the strong inhibition of tar formation by ZnCl_2 chemical promotes substantial release of volatiles from the carbon structure and contributes to substantial increase in widening of pores. Therefore, the creation of larger pores becomes more dominant resulting in a decrease in microporosity which resulted in the low surface area. (Suhas *et al.*, 2007; Lua and Yang 2005).

Besides the impregnation ratio, the activation condition also plays an important role in the preparation of activated carbon. In this study the carbon activated in nitrogen flow (AC-1Z-N and AC-2Z-N) have considerably higher surface area. This result suggests that the volatiles were quickly removed away from the pores and the sample surface under nitrogen flow ($300 \text{ cm}^3 \text{ min}^{-1}$), thereby reducing the possibility of volatile deposition on the pores and sample surface which will otherwise clog the pores and reduce the surface area (Lua *et al.*, 2000).

The above findings lead to the conclusion that the impregnation ratio and the activation condition have a notable influence on the process yield. However, the single point BET surface area should not be taken as the only parameter to evaluate the physical properties of activated carbon. Thus, the pore texture of all the prepared activated carbons was further studied.

4.2.2.2 BDDT Isotherms and Pore Size Distribution

Nitrogen adsorption analysis is also known as pore texture analysis. It gives a

complete physical characterization including the surface area, type of pore, pore volume and diameter of pores. Hence, in this study all the prepared activated carbon samples were sent for nitrogen adsorption analysis. By using the data of nitrogen adsorption, the BDDT isotherms and pore size distribution graphs were plotted. The shape of BDDT isotherm can provide qualitative information on the adsorption process and the extent of the surface area available to the adsorbate.

The BDDT isotherms for the activated carbon prepared in nitrogen gas flow and vacuum condition with different chemical ratios are displayed in Figure 4.4 and 4.6. The amount of nitrogen adsorbed was plotted against the relative pressure, P/P_0 of nitrogen where P is vapor pressure and P_0 is saturated vapor pressure. Referring to Figure 4.4 it is obvious that the BDDT isotherms of AC-1Z-N and AC-1Z-V are very similar in shape. These are type I isotherm, which represent microporous solid, according to IUPAC classification. The isotherms exhibit a pronounced increase in the volume of nitrogen adsorbed for low relative pressure and a weak increase at higher relative pressure, almost horizontal plateau indicating the dominant presence of micropores in the samples (Asiah and Noor Khaidawati, 2005). In both isotherms of AC-1Z-N and AC-1Z-V a very narrow hysteresis loop can be observed at relative pressure higher than 0.4, indicating the presence of mesopores. Thus, small amount of mesopores is believed to be present and this statement is supported by the pore size distribution plot.

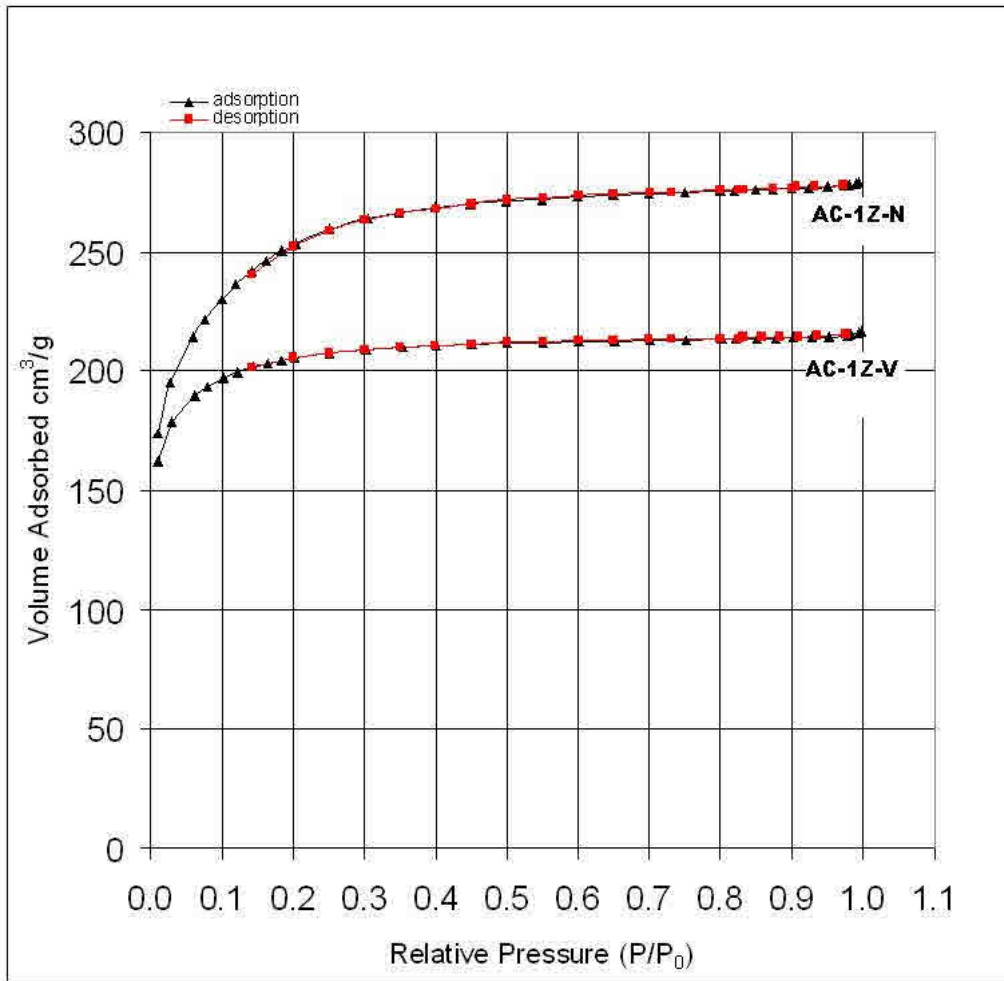


Figure 4.4: BDDT isotherm of AC-1Z-N and AC-1Z-V.

The pore size distribution plots of AC-1Z-N and AC-1Z-V are shown in Figure 4.5 and 4.6. The general trend of pore size distribution graph is similar under both nitrogen flow and vacuum condition. Referring to Figure 4.5, there is a small shoulder at a pore diameter of 120 Å implying that small amount of mesopores might be present in AC-1Z-N. While, for AC-1Z-V two shoulder type of peaks observed in the mesopores region. A small shoulder occurred at 120 Å another shoulder at 38 Å. As the pore diameter decrease to 20 Å, the graphs tend to increase sharply. This indicates the presence of micropores. It can thus be suggested that activated carbons prepared with impregnation ratio of 1:1 in nitrogen flow and vacuum condition are microporous material that contain a very small amount of mesopores.

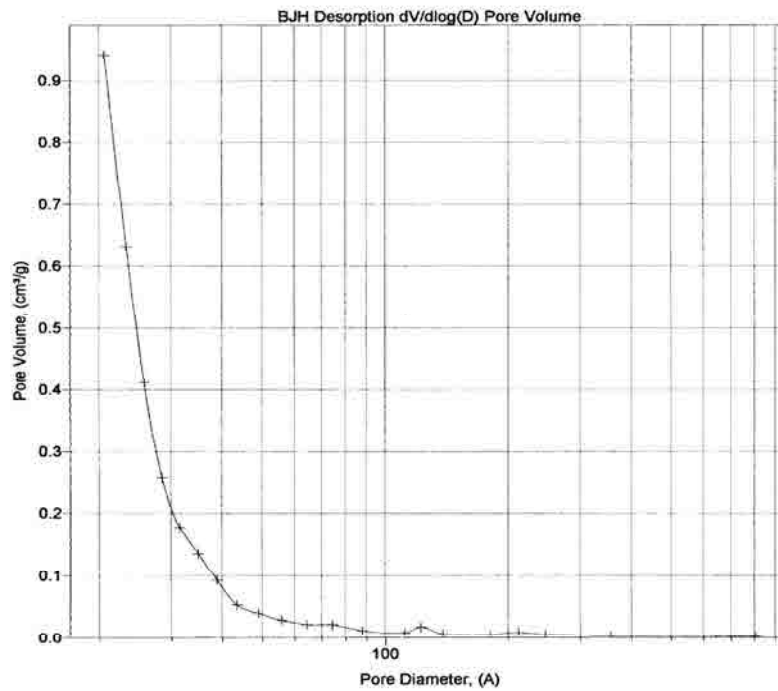


Figure 4.5: Pore size distribution graph of AC-1Z-N.

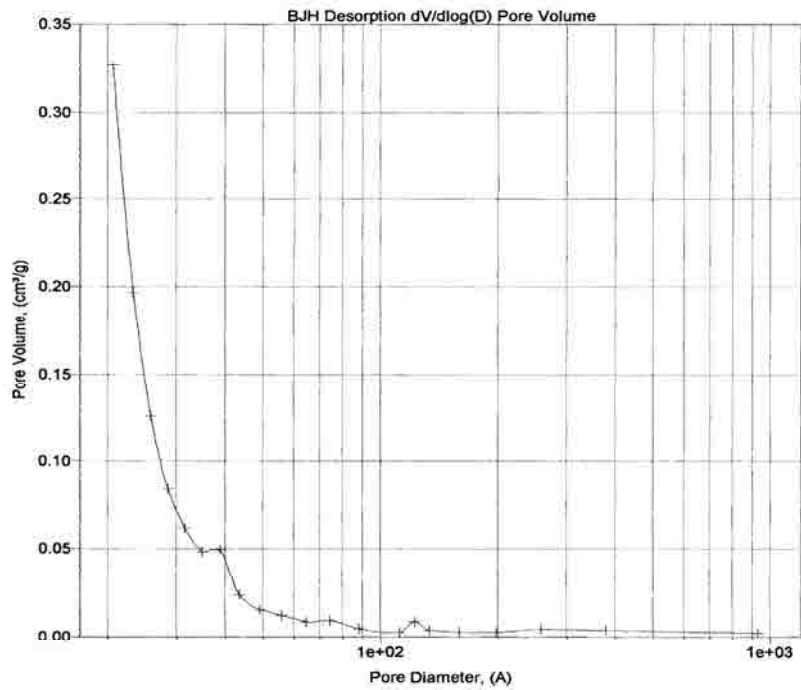


Figure 4.6: Pore size distribution graph of AC-1Z-V

On the other hand, when the impregnation ratio increases to 2:1, the BDDT isotherms begin to change considerably. Figure 4.7 shows the BDDT isotherms of AC-2Z-N and AC-2Z-V. It can be seen clearly that the isotherms are also type I isotherms similar to AC-1Z-N and AC-1Z-V. The isotherms exhibit the high uptake of nitrogen gas at low relative pressure. However the widening of hysteresis loop becomes obvious in BDDT isotherms of AC-2Z-N and AC-2Z-V. The presence of hysteresis loop at relative pressure higher than 0.4 indicates the formation of mesopores. In the BDDT isotherm of AC-2Z-N it was found that the hysteresis loop does not close up at relative pressure of 0.4, but expands to low pressure of 0.15. The hysteresis loop which occurs at relative pressure less than 0.4 is defined as low pressure loop (LPH). This phenomenon is due to the swelling of activated carbon particles during the adsorption process. The swelling distorts the structure of activated carbon by prising apart weak junctions and open up cavities which were previously inaccessible to adsorbate molecules. Since the distortion is not elastic, some molecules become trapped and can escape very slowly or possibly not at all during the desorption process (Figueiredo and Moulijn, 2005)

The fact that mesopores are present in AC-2Z-N and AC-2Z-V is supported by pore size distribution. Figure 4.8 and 4.9 present the pore size distribution graph for AC-2Z-N and AC-2Z-V. In the pore size distribution graph of AC-2Z-N a sharp peak is observed at 35 Å and a small shoulder around 48 Å. Whereas, For AC-2Z-V besides a sharp peak at 35 Å, there are 2 extra broad peaks are observed at 120 Å and 210 Å. This indicated that different size of mesopores is presence in the samples. The occurrence of mesopores peaks confirm to the presence of hysteresis loop at high pressure in nitrogen adsorption. As the pore diameter decrease to 20 Å the graphs tend to increase sharply, which signifies the presence of micropores. These results show that AC-2Z-N and AC-2Z-V contain both mesopores and micropores.

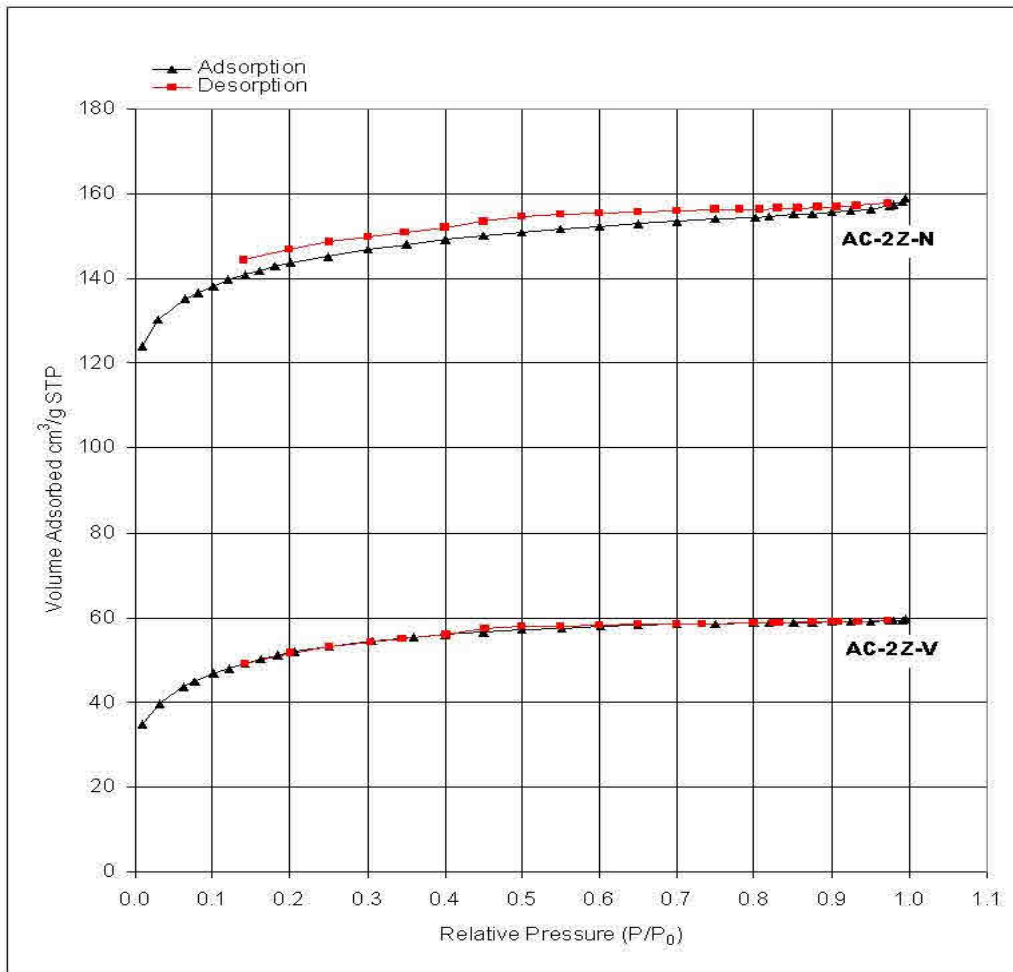


Figure 4.7: BDDT isotherm of AC-2Z-N and AC-2Z-V

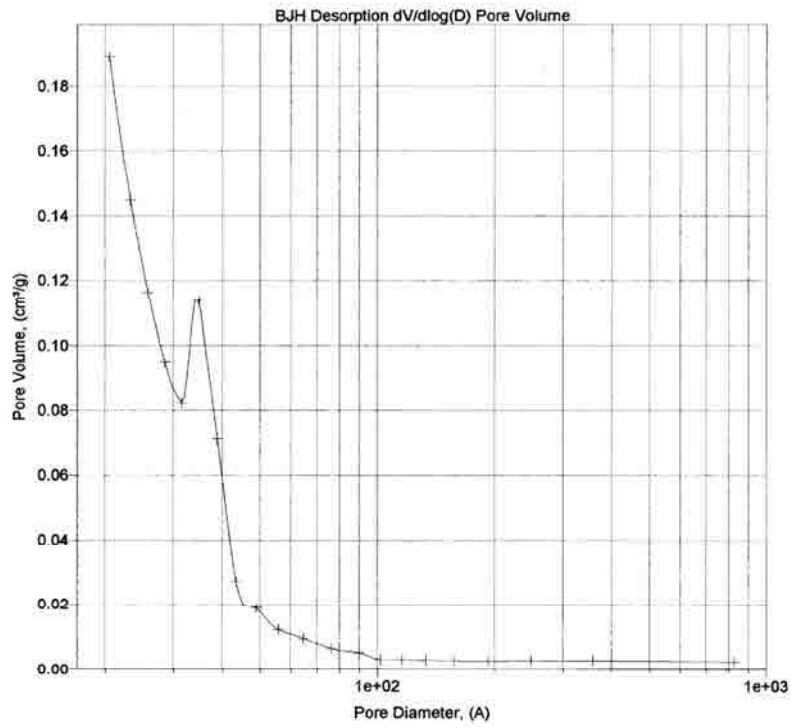


Figure 4.8: Pore size distribution graph of AC-2Z-N

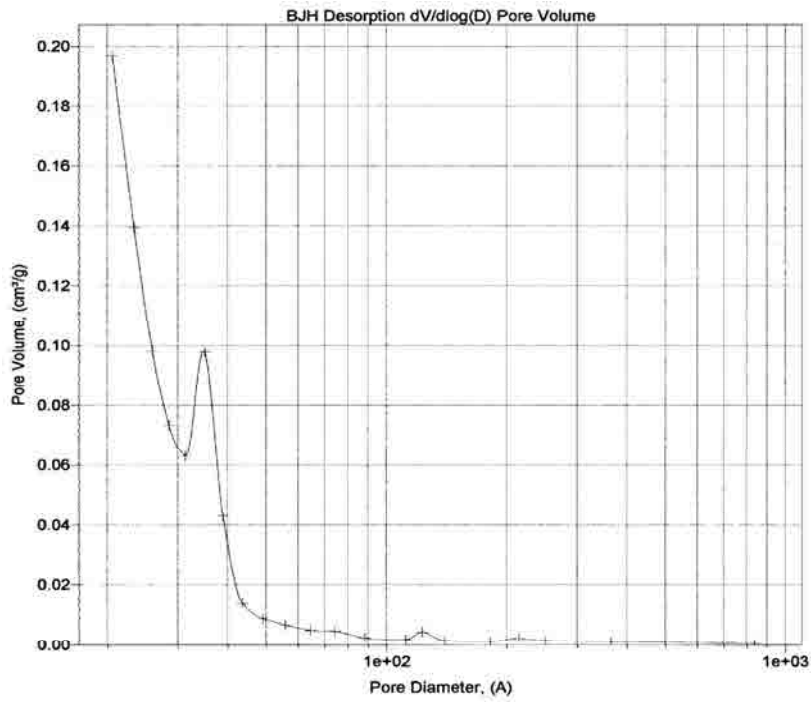


Figure 4.9: Pore size distribution graph of AC-2Z-V

From the above discussion above, it can be suggested that the impregnation ratio plays a fairly important role in the formation of mesopores which is parallel to the observation of opening of the hysteresis loop (Figure 4.7). In addition, the activation condition influences the adsorption capacity of resulting activated carbon. The amount of adsorbed nitrogen is indicative of the adsorption capacity of activated carbon. In general, From BDDT isotherms it can be suggested that the activated carbons prepared in nitrogen flow possess higher adsorption capacity compare to vacuum activation. This is most probably due to in the vacuum condition; reduce pressure results in a decrease in temperature. Hence, the sample temperature would lower than 700°C set for the furnace. A lower temperature would mean reduced release of volatiles, giving a weak pore formation, resulting low adsorption capacity (Lua and Yang 2005).

4.2.2.3 The t -plot

The t -plot of Harkin-Jura is one of the empirical methods used to compare experimental isotherm with the standard obtained on suitable nonporous reference solid (Asiah and Noor Khaidawati, 2005). In this study, Harkin-Jura equation and nitrogen adsorption data were used to produce the t -plot (refer Appendix 6.0 to Appendix 9.0). The gradient of the straight line gives the external surface area, S_{ex} , whereas the intercept gives micropore volume. The micropore surface area was calculated by subtracting the external surface area from the total BET surface area. The data for all the prepared activated carbons were tabulated in Table 4.3. From the table, it can be seen that the activated carbons prepared with impregnation ratio of 1:1 in both nitrogen atmosphere and vacuum condition (AC-1Z-N and AC-1Z-V) have average pore diameter 1.95 nm and 1.92 nm respectively. Typically micropores are pores with diameter range between 1 to 20 nm (Marsh and Rodriguez-Reinoso, 2006). This shows that majority of the pores in these activated carbon structure are micropores. This statement is supported by the BDDT isotherm (Figure 4.4), where the both isotherms of AC-1Z-N and AC-1Z-V are of type I isotherm.

Table 4.3: Surface area and pore volume of activated carbon

Sample	AC-1Z-N	AC-1Z-V	AC-2Z-N	AC-2Z-V
BET surface area, S_{BET} (m^2g^{-1})	884	699	486	181
Average pore diameter (nm)	1.95	1.92	2.02	2.04
Micropore volume, V_{MP} (cm^3g^{-1})	0.36	0.28	0.19	0.05
Micropore surface area, S_{MP} (m^2g^{-1})	786	585	405	119
External surface area, S_{ex} (m^2g^{-1})	98	114	81	62

Note: $S_{MP} = S_{BET} - S_{EXT}$

On the other hand, the pore diameter for AC-2Z-N and AC-2Z-V increase to 2.02 nm and 2.04 nm respectively, indicate the presence of mesopores. This is most probably when the impregnation ratio of 1:1; the initial weak inhibition of tar formation by ZnCl_2 influence the release of volatiles to produces predominantly micropores in the carbon structure, with limited development of mesopores or macropores. However, when the ratio increases to 2, strong inhibition of tar formation by the ZnCl_2 chemical promotes substantial release of volatile from carbon structure. This then contributed to the increase in the pore widening. The micropores can be subsequently converted to mesopores and even macropores (Mohanty *et al.*, 2005). Therefore, increasing the impregnation ratio in nitrogen flow and vacuum condition resulted in reduced micropore volume. It can be observed that the AC-1Z-N has $0.36 \text{ cm}^3\text{g}^{-1}$, whereas the micropore volume decreased to $0.28 \text{ cm}^3\text{g}^{-1}$ in AC-2Z-N.

This result is supported by the value of micropore surface area and the external surface area. The micropore surface area of AC-1Z-N and AC-1Z-V is higher than their external surface area. This implies that the high surface area of in AC-1Z-N and AC-1Z-V is probably contributed mainly by micropores. While for AC-2Z-V, which has lowest BET surface area of $181 \text{ m}^2\text{g}^{-1}$, shows that more than one third of the total BET surface area is contributed by the external surface area. ($62 \text{ m}^2\text{g}^{-1}$). This indicated that even though micropores are present, they are possibly present in small amount and their contributions are comparatively small. This result is in agreement with the

BDDT isotherms where the opening of hysteresis loop implies the presence of mesopores in the activated carbons prepared with the impregnation ratio of 2:1.

In summary, the activated carbon prepared in nitrogen flow with the impregnation ratio of 1:1 produced high surface area micropores carbon. As the activated carbons prepared in this study are intended for gas phase reaction, the presence of microporosity is critical. Hence, AC-1Z-N, AC-1Z-V and AC-2Z-N were selected for further analysis.

4.2.3 FESEM analysis of activated carbons.

The FESEM analysis was employed to study the surface morphology and the porosity of the activated carbon. The FESEM micrographs also provide information on the structural changes in the palm kernel shell anatomy during the activation process.

Figure 4.10 shows the micrograph of raw-PKS. The surface of raw-PKS is dense and planar without any cracks and crevices. This would account for its poor or negligible BET surface area (Figure 4.3). The wood-grain could be seen clearly on the surface since oil palm shell is a typical type of lignocellulosic materials.

Figure 4.11 shows the micrograph of AC-1Z-N at 150x magnification. In contrast, for the AC-1Z-N, there were no more lignocellulosic structures on surface but many cavities over the surface, forming a system of advanced pore network. The frame work development was so rapid, resulting in too much cavities and leads to crack formation. Due to this well developed pores, the AC-1Z-N possessed high BET surface area ((Figure 4.3). Figure 4.12 shows the micrograph of AC-1Z-N at higher magnification 7500x. The micrograph magnifies the internal cavities which are now clearly visible. Direct measurement from the micrograph shows that the average pore diameter is 1 μ m. The surface of the AC-1Z-N seems to be clearer and smoother than

raw-PKS surface due to the removal of volatile compounds and impurities during the activation process and followed by hydrochloric acid –wash.

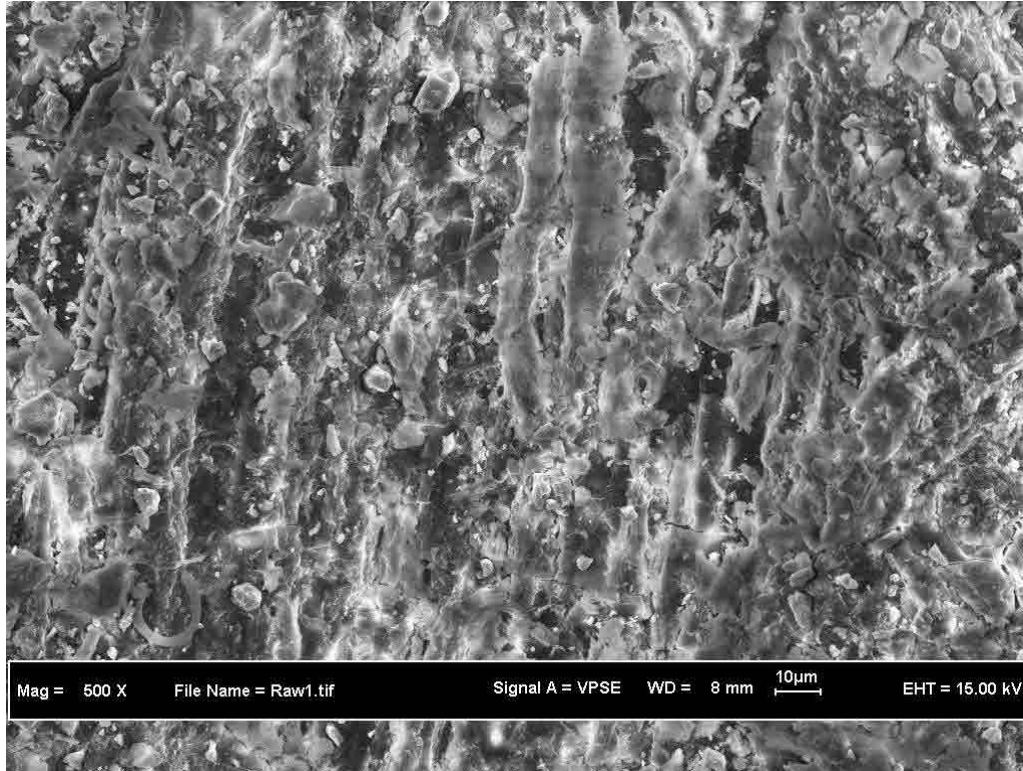


Figure 4.10: Micrograph of raw-PKS with magnification of 500x

Figure 4.13 shows the micrograph of AC-1Z-V with magnification of 150x. Cavities with different size and different shape could be observed. It can be seen that there were more solidified areas in appearance compare to AC-1Z-N where the surface is full of cavities. At higher magnification (Figure 4.14) the presences of internal cavities can be observed. It can also be seen that some small white particles are scattered on the surface of the carbon, probably due to the presence of remaining $ZnCl_2$ residues or some other impurities.

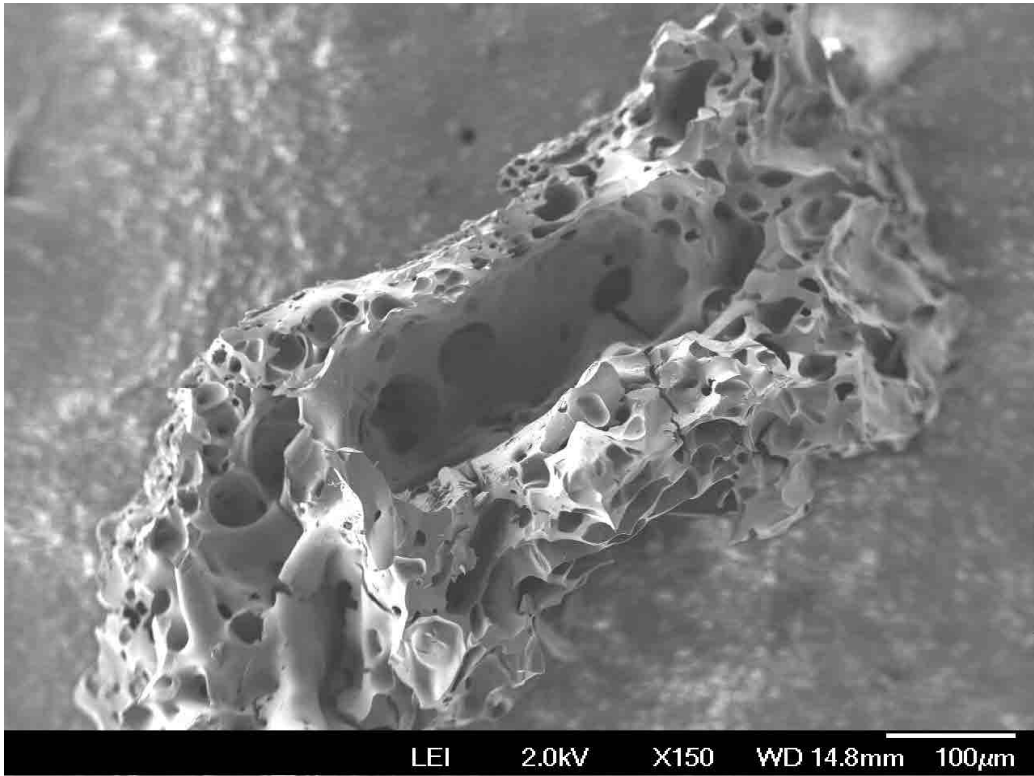


Figure 4.11: Micrograph of AC-1Z-N with magnification of 150x.

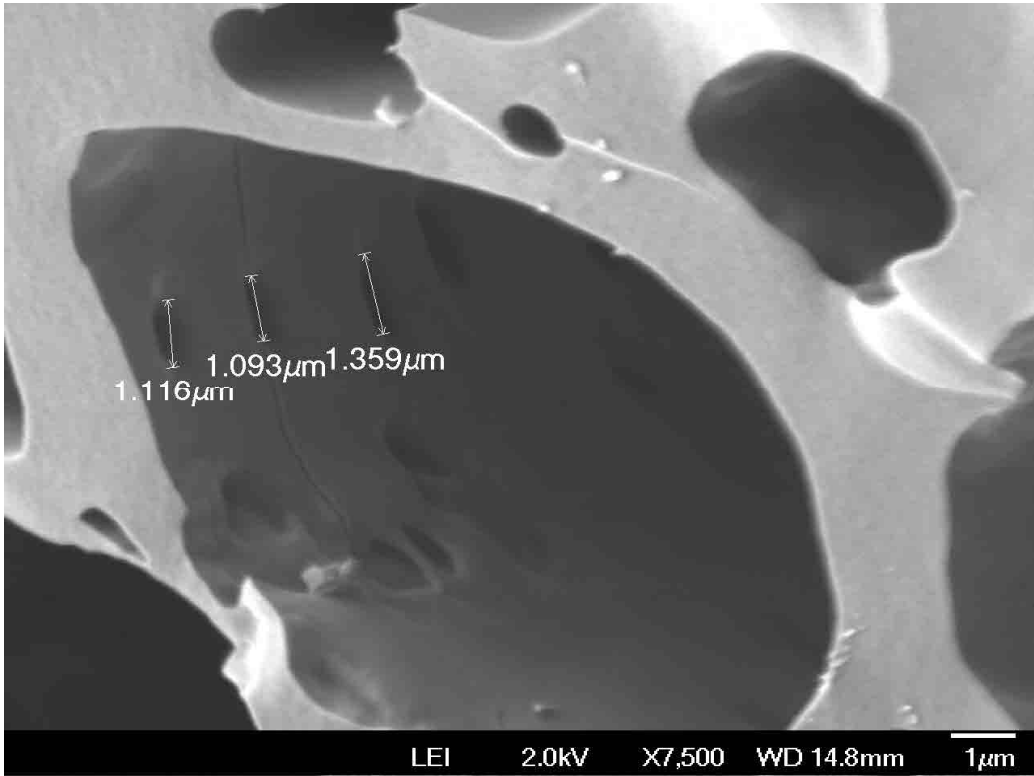


Figure 4.12: Micrograph of AC-1Z-N with magnification of 7500x.

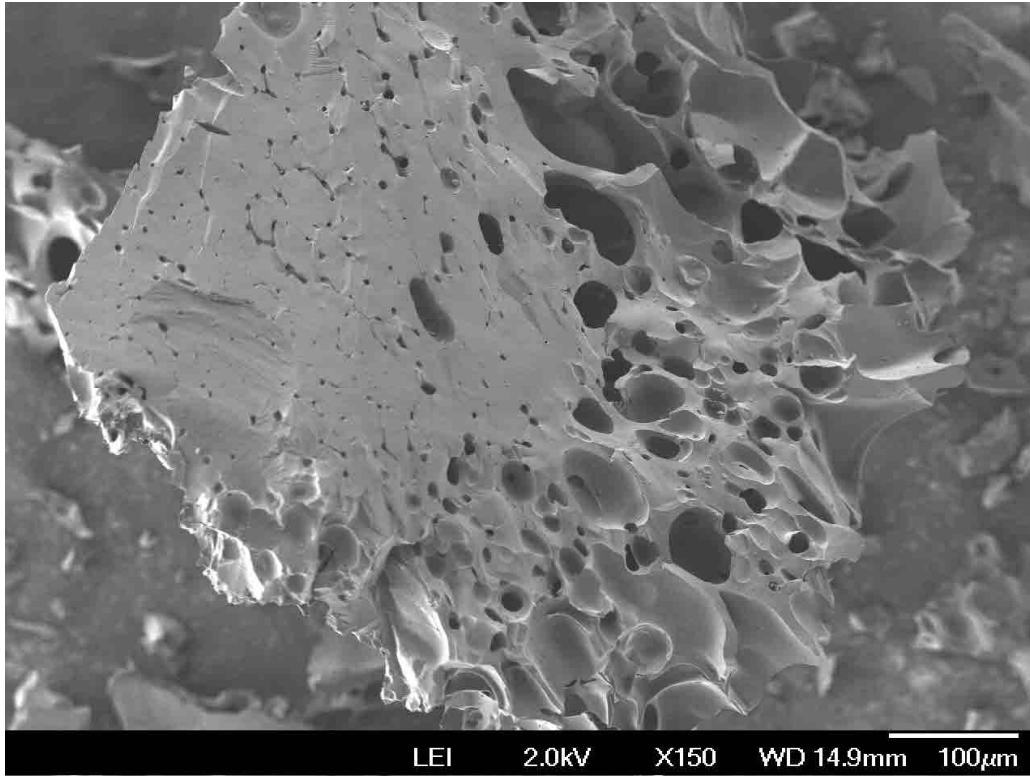


Figure 4.13: Micrograph of AC-1Z-V with magnification of 150x.

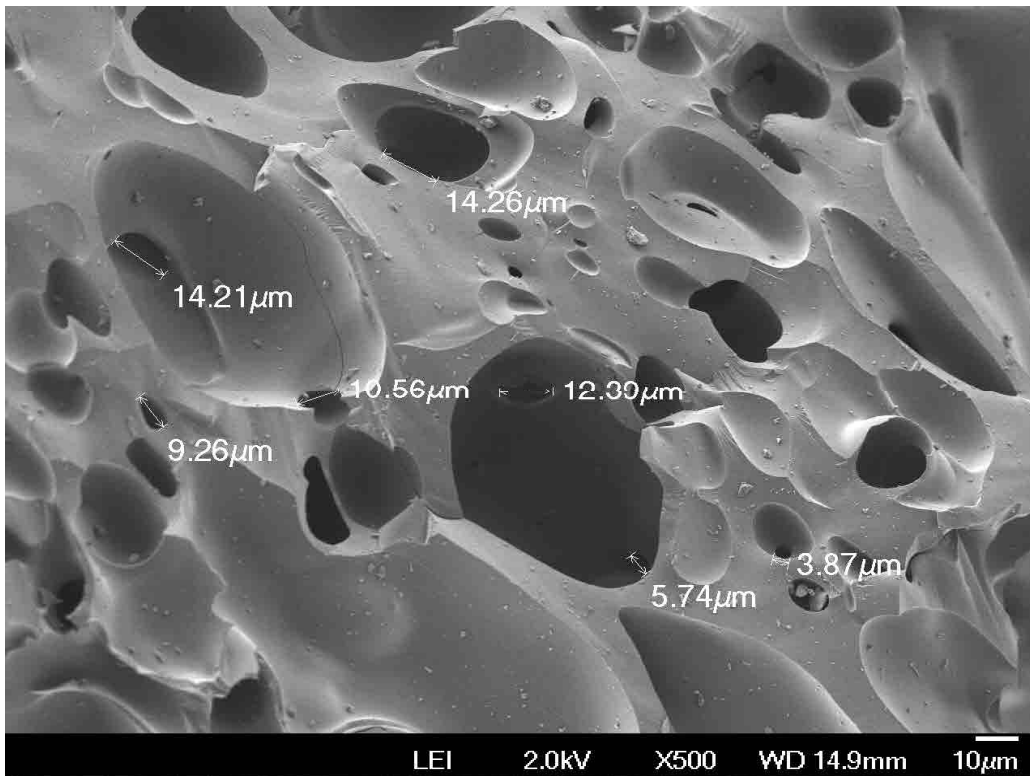


Figure 4.14: Micrograph of AC-1Z-V with magnification of 500x.

Figure 4.15 and 4.16 present the FESEM micrograph of AC-2Z-N at different magnification. Unlike the previous activated carbons (Figure 4.11 and 4.13), when the impregnation ratio increase, the solid surface of palm kernel shell has transformed to less dense and uneven textures with bigger cavities, resembling a mixture of wood shavings. The formation of pores in activated carbons resulted from the evaporation of $ZnCl_2$ during activation, leaving the space previously occupied by the $ZnCl_2$. As the impregnation ratio increased to 2, the intense release of volatile from carbon structure contributes to substantial increase in the widening of the pores. This finding is parallel to the micropore surface area obtained earlier in subtopic 4.2.2.3. The result showed that the micropore surface area had decreased when the impregnation ratio increases to 2.

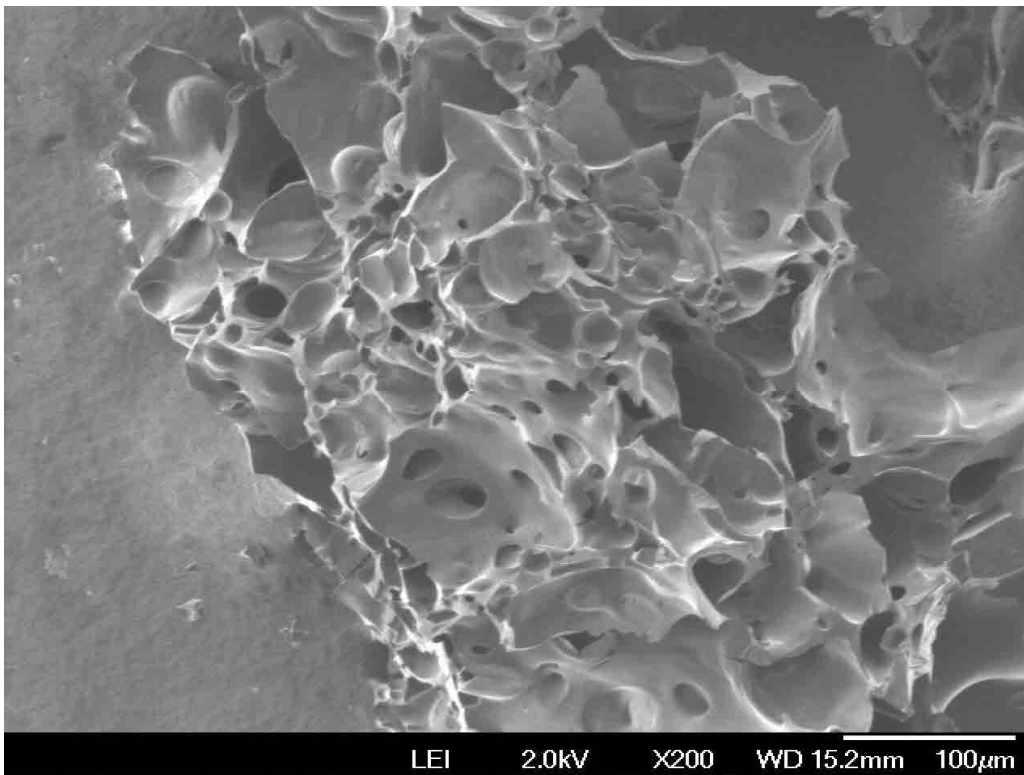


Figure 4.15: Micrograph of AC-2Z-N with magnification of 200x

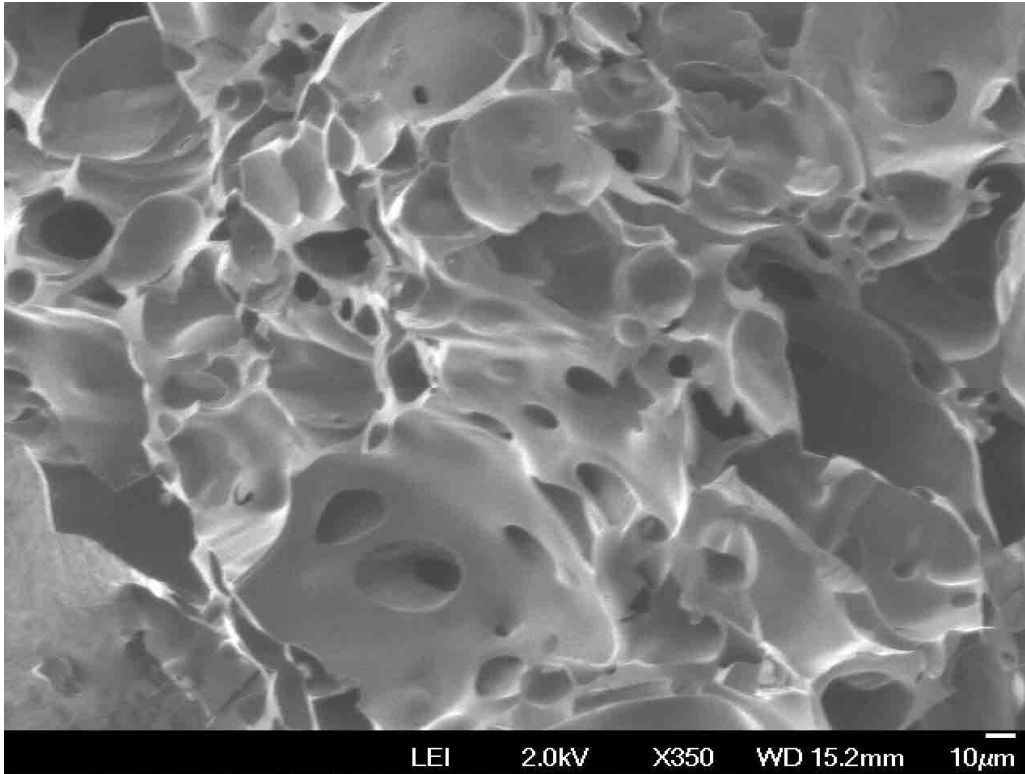


Figure 4.16: Micrograph of AC-2Z-N with magnification of 350x.

4.2.4 Energy Dispersive X-ray analysis (EDX)

Energy Dispersive X-ray (EDX) analysis was carried out during on the surface of activated carbons. The value or the data obtained with EDX analysis is only a rough estimation of the surface elemental composition. It should not be regarded as an absolute composition of the activated carbon.

The surface composition of three activated carbon samples namely AC-1Z-N, AC-1Z-V and AC-2Z-N, are tabulated in Table 4.4. Among the three samples, AC-1Z-N showed the highest percentage of carbon, 97.23% followed by AC-2Z-N and AC-1Z-V. The presence of zinc and chlorine elements was detected in all the samples,

most probably due to the incomplete washing process to eliminate the activating agent used.

Table 4.4: EDX analysis of activated carbons.

Sample	Mass %		
	Carbon	Chlorine	Zinc
AC-1Z-N	97.23	0.59	2.19
AC-1Z-V	90.42	2.32	7.20
AC-2Z-N	92.59	2.15	5.26

For AC-1Z-V the percentages of zinc and chlorine elements are higher compared to AC-1Z-N and AC-2Z-N. This again suggests that the lower pressure in vacuum condition gave rise to a lower activation temperature than the furnace temperature for the nitrogen gas. This lower activation temperature release less volatiles together with $ZnCl_2$, which is in agreement with to FESEM results obtained in previous subtopic 4.2.3.

On the other hand, it can be seen clearly that the percentages of zinc and chlorine increased as the impregnation ratio increased to 2:1, suggesting that more $ZnCl_2$ remained impregnated on the activated carbon surface.

4.2.5 Thermogravimetry analysis

In this study, thermogravimetry analysis was carried in order to determine the thermal stability of raw palm kernel shell and prepared activated carbons. Three samples: raw-PKS, AC-1Z-N and AC-1Z-V were subjected to measure in temperature range of 40 -1000°C at a heating rate 10°C/min under air flow and nitrogen gas flow.

4.2.5.1 Thermogravimetry analysis of raw palm kernel shell

The TGA of raw palm kernel shell (raw-PKS) was conducted in air flow with the temperature range of 40 - 850°C. Figure 4.17 shows three stages of thermal decomposition behavior of raw-PKS. The first stage range from 40 - 200°C, presents 15% weight loss due to the moisture release.

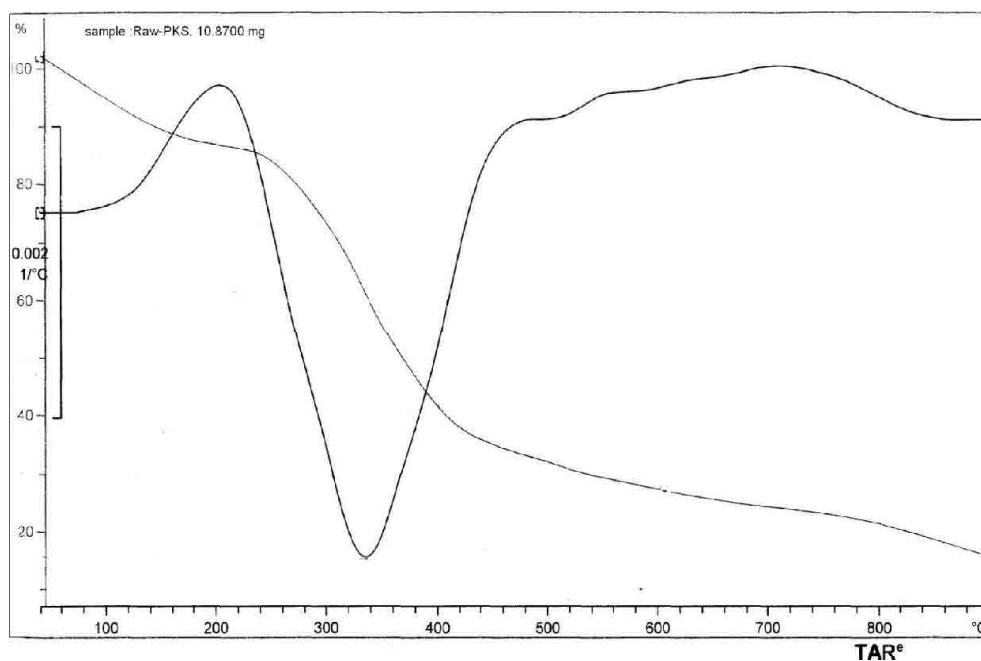


Figure 4.17: TGA/DTG curves of raw-PKS

In the temperature range of 200 - 500°C, a weight loss of 55% is observed. Such weight loss is attributed to the decomposition or oxidation of the organic compounds such as lignin and cellulose in the raw-PKS. Naturally palm kernel shell contains about 30% of cellulose, 47% of hemicellulose and 53% of lignin (Daud and Ali, 2004).

On the other hand, there are no significant changes in weight when the sample was heated above 500°C. It is believed that the organic compounds in raw-PKS were oxidized completely at 500°C, which is typical of lignocellulosic materials (Hu *et al.*, 2000; 2001 and Boonamnuayvitaya *et al.*, 2005). Therefore in this study, a

temperature of 700°C was used as the activation temperature for the preparation of activated carbon. The activation temperature was 200°C higher than 500°C to ensure the complete decomposition of organic compounds and liberation of volatiles.

4.2.5.2 Thermogravimetry analysis of activated carbons in air flow

Figure 4.18 and 4.19 show the weight loss TG/DTG curves of AC-1Z-N and AC-1Z-V. Generally both activated carbons exhibit similar pattern of weight loss. The weight loss process of activated carbons may be divided into three main stages, namely stage I, stage II and stage III. The percentage loss at each stage and their respective temperature range are summarized in Table 4.5.

The weight loss at stage I can be assigned to the dehydration of activated carbons. This could be explained by the hygroscopic nature of activated carbon that adsorbs moisture from atmosphere. The weight loss of AC-1Z-N and AZ-1Z-V is approximately 15% and 27% respectively. The results show that AC-1Z-V has higher percentage of moisture content. This is most probably due to the presence of zinc chloride residues in AC-1Z-V as shown in EDX results obtained in earlier subtopic 4.2.4. The presence of zinc chloride which acts as the dehydrating agent adsorbed more water molecules in the air during the sample preparation resulted to high moisture content.

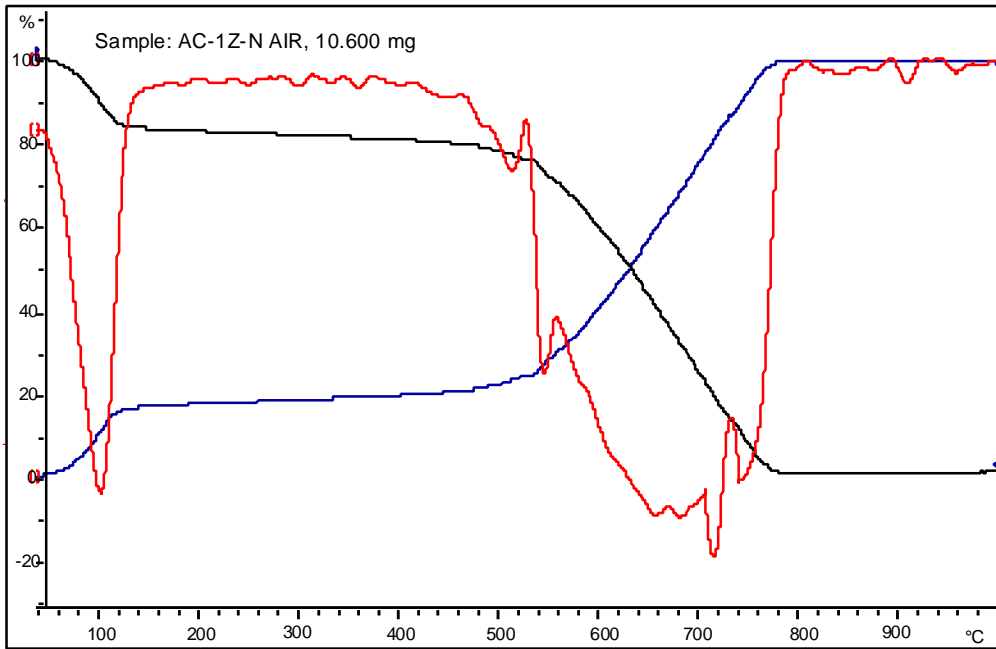


Figure 4.18: TGA/DTG curves of AC-1Z-N in air flow.

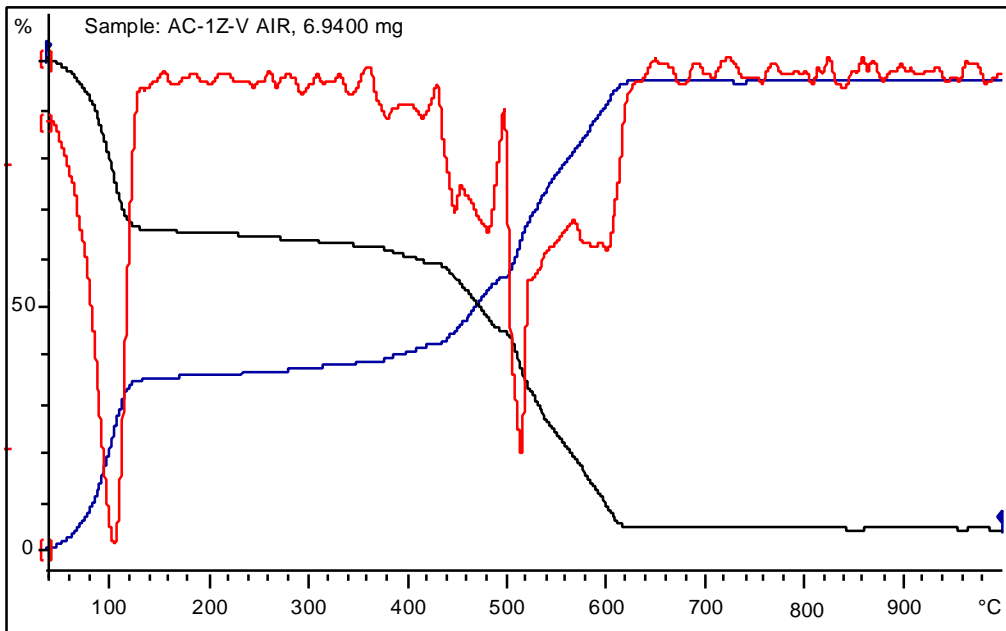


Figure 4.19: TGA/DTG curves of AC-1Z-V in air flow.

Table 4.5: Percentage of weight loss of AC-1Z-N and AC-1Z-V in air flow.

Activated carbon	Weight loss (%)			
	Stage I	Stage II	Stage III	Residue
	40-140°C	140-400°C	400-840°C	840-1000°C
AC-1Z-N	15	4	80	1
AC-1Z-V	27	5	59	4

On the other hand, the weight loss in stage II is ascribed to the decomposition of low temperature volatile organic functional groups present in the activated carbon samples. Stage II occurs within the temperature range of 140°C to 400°C. The weight loss of AC-1Z-N and AC-1Z-V is approximately 4% and 5% respectively. It can be seen that the difference in volatile matters was not distinct. Referring to the Figure 4.18 and 4.19, the weight loss was gradual and different from the raw-PKS (Figure 4.17), where a large peak appeared between 200 - 500°C corresponding to the decomposition of volatile organic compounds. Thus, it can be suggested that the ZnCl₂ impregnation and activation process has a significant effect on the pyrolysis behavior of palm kernel shell.

At temperature higher than 400°C, the weight was lost significantly, shown by a broad peak. The evolution obviously represents the combustion of carbon in the air. Thus, the weight loss in this stage might be a rough indication of the carbon content of activated carbons. The weight loss in this stage is 80% and 59% for AC-1Z-N and AC-1Z-V respectively. It was found that the raw-PKS are high in volatile matter content and low in fixed carbon content. However, after the activation process the volatile matter of the activated carbons has decreased whilst the carbon content increased. The chemical activating agent, ZnCl₂ causes hydrogen and oxygen atoms in the palm kernel shell to be stripped away as water rather than as hydrocarbons or oxygenated organic compounds. As a result, the carbon content increase. The results also show that the carbon content in AC-1Z-N is higher than AC-1Z-V, probably due to the lower temperature in vacuum condition.

As the temperature increase to 1000°C, the weight of activated carbons is almost stable. The remaining weight of the activated carbons was approximately 1% and 4% respectively for AC-1Z-N and AC-1Z-V. This heavy remaining weight can be explained by the presence of the unreacted activating agent impregnated during carbonization and the inorganic constituent was left on the carbon surface irremovable during washing process.

4.2.5.3 Thermogravimetry analysis of activated carbons in nitrogen flow

Figure 4.20 and 4.21 shows the TG and DTG curves of AC-1Z-N and AC-1Z-V in nitrogen flow. The weight loss process was divided into two stages. The percentage of weight loss at each stage is summarized in Table 4.6.

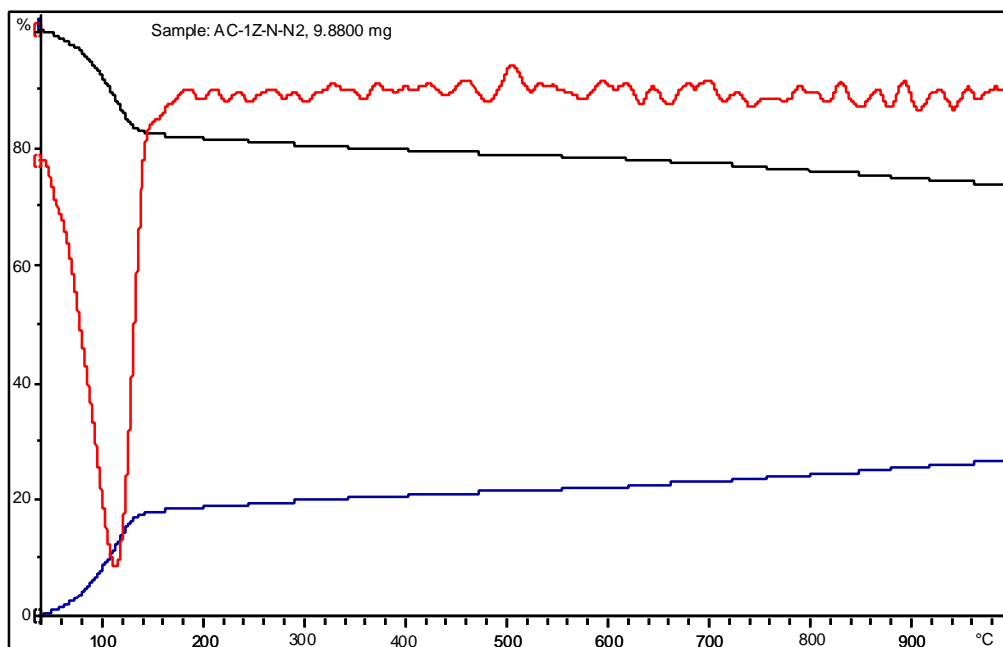


Figure 4.20: TGA/DTG curves of AC-1Z-N in nitrogen flow.

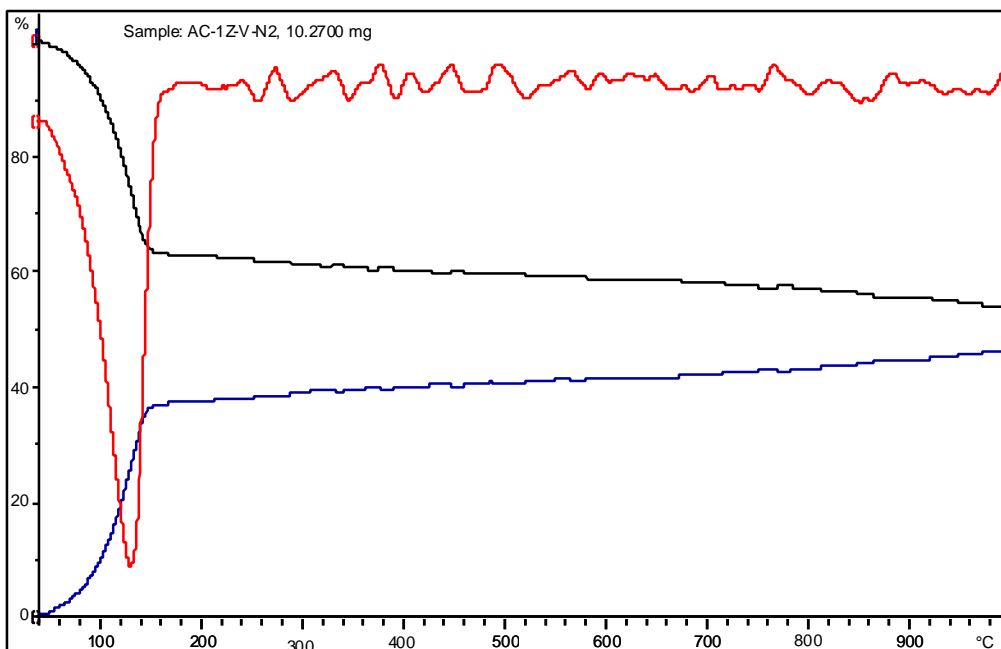


Figure 4.21: TGA and DTG curves of AC-1Z-V in nitrogen flow.

The weight loss observed in stage I corresponds to the dehydration of activated carbons. In this stage AC-1Z-N and AC-1Z-V is 18% and 30% respectively. This result is consistent with the TGA results obtained in air flow, which has been discussed in details in previous subtopic 4.2.5.2.

Table 4.6: Percentage of weight loss of AC-1Z-N and AC-1Z-V in nitrogen flow.

Activated carbon	Weight loss (%)	
	Stage I 40-200°C	Stage II 200-1000°C
AC-1Z-N	18	7
AC-1Z-V	30	11

In the stage II, when the temperature increases up to 1000°C, the weight loss was gradual. The profile suggests that the weight loss in this stage can be approximately described by the decomposition of volatile organic functional groups.

Referring to the Figure 4.20 and 4.21 AC-1Z-N exhibited the lowest percentage of weight loss with only 7%, whereas AC-1Z-V showed 11% of weight loss. This is as expected activation in nitrogen flow converted more volatiles into pure carbons, resulting in activated carbon with high thermal stability. Meanwhile, AC-1Z-V contained large amount of organic functional groups, suggesting that conversion of volatile matters was incomplete in vacuum condition.

4.3 Tungsten carbide catalyst

The tungsten carbide catalysts were produced using the previously prepared activated carbon. As the catalyst in this study is intended for gas phase catalytic reaction, the maximum possible surface area is sought. Hence, AC-1Z-N and AC-1Z-V with high surface area were selected and used as carbon source as well as catalyst support for the carbide catalyst.

The catalysts were prepared with two different metal content namely, 6% and 15% tungsten using tungsten hexacarbonyl as precursors. The catalysts so prepared were heat treated at 700°C and 950°C in helium flow. The samples then characterized using XRD, SEM, EDX and single point BET. The effect of tungsten content, type of activated carbon and the temperature of heat treatment on the formation of tungsten carbide were investigated. Notations for samples prepared are shown in Table 4.7.

Table 4.7: Notation for the samples prepared

Notation	Type of carbon	Tungsten content (%)	Temperature of heat treatment (°C)
ACN-6-700	AC-1Z-N	6	700
ACN-15-700	AC-1Z-N	15	700
ACV-6-700	AC-1Z-V	6	700
ACV-15-700	AC-1Z-V	15	700
ACN-6-950	AC-1Z-N	6	950
ACN-15-950	AC-1Z-N	15	950
ACV-6-950	AC-1Z-V	6	950
ACV-15-950	AC-1Z-V	15	950

4.3.1 X-ray diffraction (XRD)

4.3.1.1 XRD analysis of tungsten carbide catalyst supported on AC-1Z-N

The chemical state of metallic compound phase was studied by XRD after the supported catalysts were heat treated in helium flow at different temperatures. The diffractogram patterns of AC-6-700 and AC-6-950 illustrated in Figure 4.22. The XRD pattern of ACN-6-700 shows three major peaks of tungsten carbide, WC at 2θ values of approximately 31.398, 35.656 and 48.229°. The minor peaks were identified as tungsten trioxide, WO_3 and tungsten semicarbide, W_2C . The presence of WO_3 peaks indicates that the reduction of tungsten oxide was not complete at 700°C. Meanwhile, the formation of W_2C is possibly due to the incomplete transformation into tungsten carbide.

When the sample was heat treated at 950°C (ACN-6-950), the diffractogram peaks corresponding to metallic tungsten oxide in the form of WO_3 and WO_2 can still be found. However W_2C and WC were the predominant phases. The main peaks of W_2C were observed at 2θ values of 34.351, 38.346, 39.521, 52.875 and 61.543°. While the presence of WC peaks was seen at 2θ values of 31.403, 35.651 and 48.335°. Besides the existence of the carbide and oxide, metallic tungsten was detected at 41.592 and 73.122° of 2θ values. From the results obtained, it can be assumed that the reduction proceed via the formation of tungsten trioxide, tungsten dioxide, tungsten, tungsten semicarbide and tungsten carbide (Kim and Kim *et al.*, 2004).

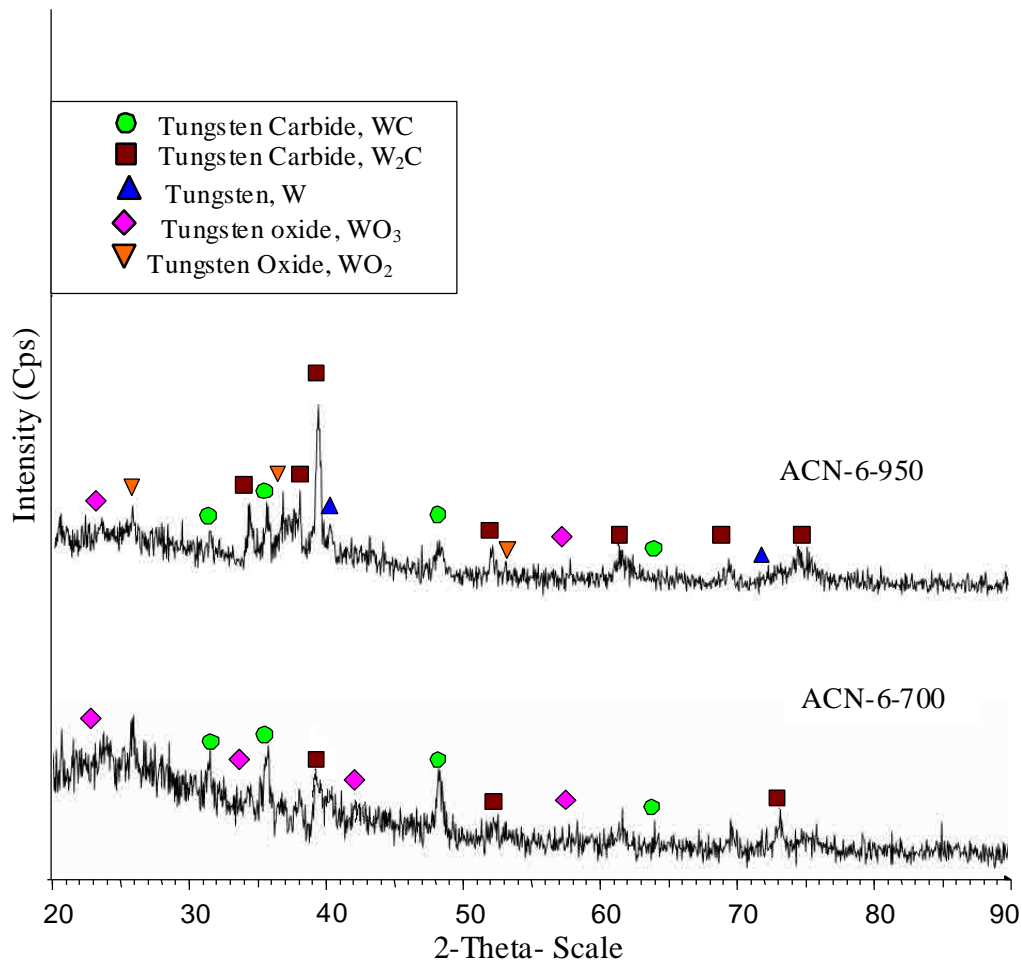


Figure 4.22: X-ray diffractogram of samples with 6 percent of tungsten content supported on AC-1Z-N

Figure 4.23 shows the diffractogram patterns of ACN-15-700 and ACN-15-950 respectively. Similar to the previous samples, the presence of tungsten carbide, tungsten semicarbide and tungsten oxide are also observed in ACN-15-700. Nonetheless, the major peaks observed are still tungsten carbide.

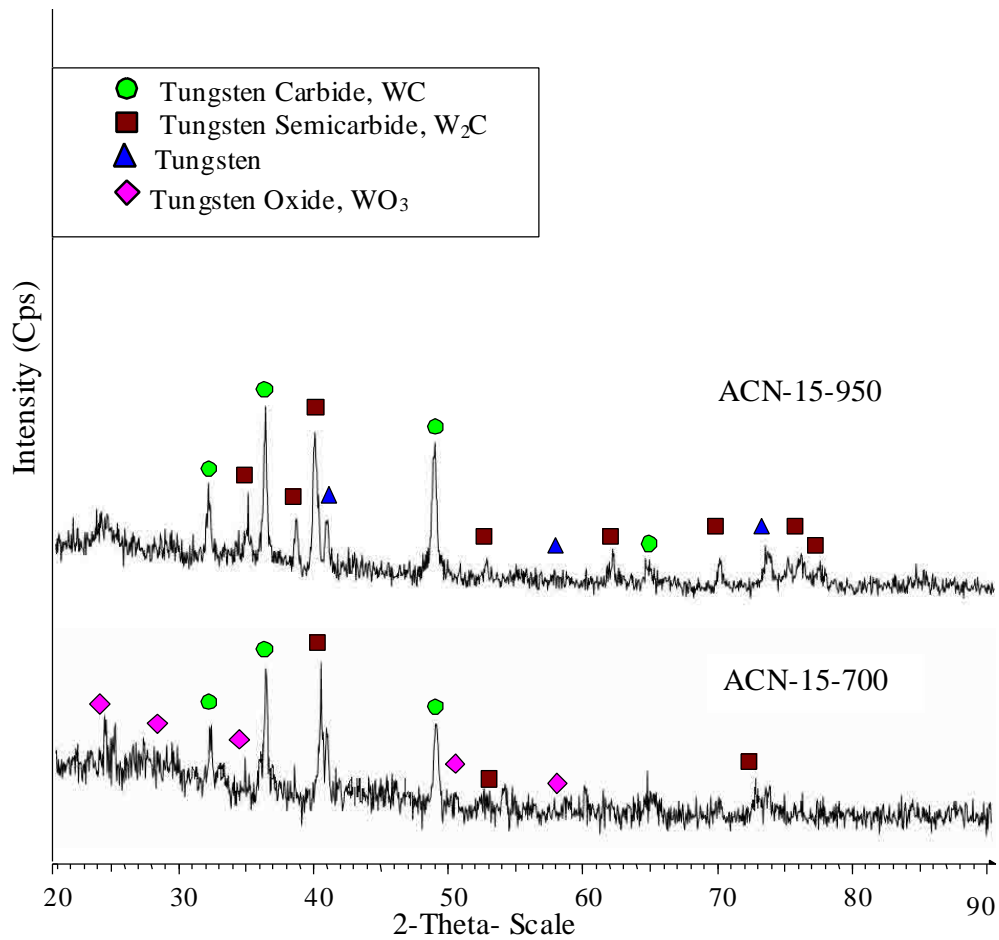


Figure 4.23: X-ray diffractogram of samples with 15 percent of tungsten content supported on AC-1Z-N

On the other hand, when the temperature is increased to 950°C the tungsten oxide phases became invisible and only a mixture of metallic tungsten carbide, tungsten semicarbide and tungsten can be obtained. It was presumed that the tungsten oxide was reduced by the carbon support to metallic tungsten at 950°C and that is

reacted with the carbon support yielding different carbides. The major peaks of tungsten carbide peaks were observed at 2θ values of 31.430, 35.617, 48.252 and 64.296 °. While the 2θ values of tungsten semicarbide peaks are 34.351, 37.947, 39.323, 52.110, 61.546, 69.571 and 75.600 °.

Table 4.8 shows the relative intensity of peaks after heat treatment in helium flow at different temperature. The formation of tungsten carbide is the highest for ACN-15-950 followed by ACN-15-700, ACN-6-700 and ACN-6-950 with relative intensity of 100.0, 81.9, 75.5 and 53.1 respectively. In the case of AC-6-950, the relative intensity of tungsten carbide peaks is lower than AC-6-700 due to substantial amount of tungsten is in the form of semicarbide. It is noteworthy that samples with 15 percent tungsten content has better formation of WC than 6 percent tungsten, possibly due to the mobility of tungsten species increased in larger proportion when the tungsten content increased (Alvarez-Merino et al., 2000).

Table 4.8: Relative intensity of main peaks for AC-1Z-N supported catalysts

Sample	ACN-6-700	ACN-6-950	ACN-15-700	ACN-15-950
Tungsten carbide, WC	75.5	53.1	81.9	100.0
tungsten semicarbide, W ₂ C	70.4	100.0	96.4	87.0
Tungsten oxide, WO ₃	100.0	43.2	61.3	-
Tungsten oxide, WO ₂	-	51.0	-	-

Meanwhile, the intensity of tungsten oxide peaks reduced as the tungsten content and temperature increased. From the data obtained it can be seen clearly that ACN-6-700 forms the highest tungsten oxide with relative intensity of 100. This is in agreement with Moreno-Castilla *et al.*, (2001) where the formation of tungsten oxide decrease when the tungsten content increased.

4.3.1.2 XRD analysis on tungsten carbide catalyst supported on AC-1Z-V

In this sub-topic, XRD analysis was carried out on the tungsten carbide samples supported on AC-1Z-V. The diffractogram patterns obtained from the XRD analysis for ACV-6-700 and ACV-6-950 are depicted in Figure 4.24. The diffractogram shows the presence of tungsten carbide. For ACV-6-700 the WC peaks were identified at 2θ values of 31.655, 36.207 and 48.700 °. Meanwhile, for ACV-6-950 the WC peaks were appeared at 2θ values of 31.291, 36.214 and 48.552 °. However, in both samples the major peaks were identified as zinc tungsten oxide (ZnWO_4) and the remaining peaks were identified as WO_3 .

The formation of ZnWO_4 is due to the carbon source used, AC-1Z-V which is the chemically activated carbon using ZnCl_2 . The presence of zinc particle is observed from the micrograph of the activated carbon, AC-1Z-V (see Figure 4.14) as indicated by the EDX result (Table 4.4). The zinc ions were not removed entirely during the washing process of the activated carbon after impregnated on the surface of the carbons.

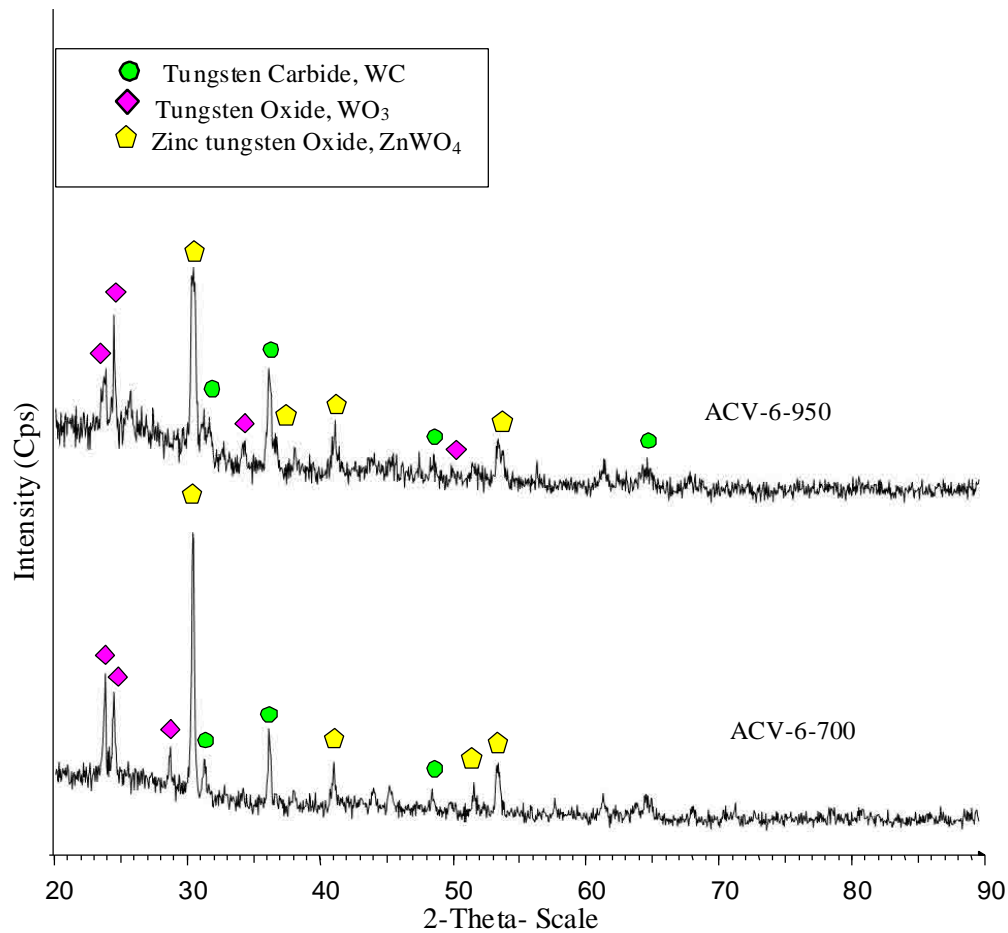


Figure 4.24: X-ray diffractogram of samples with 6 percent of tungsten content supported on AC-1Z-V

Figure 4.25 shows the diffractogram patterns for samples with 15 percent tungsten content. In both samples, major peaks were identified as tungsten dioxide. No tungsten trioxide peaks were observed, which means tungsten trioxide was reduced to tungsten dioxide during the heat treatment. Meanwhile, minor peaks were identified as tungsten carbide. The existence of ZnWO₄ can also be seen in these samples.

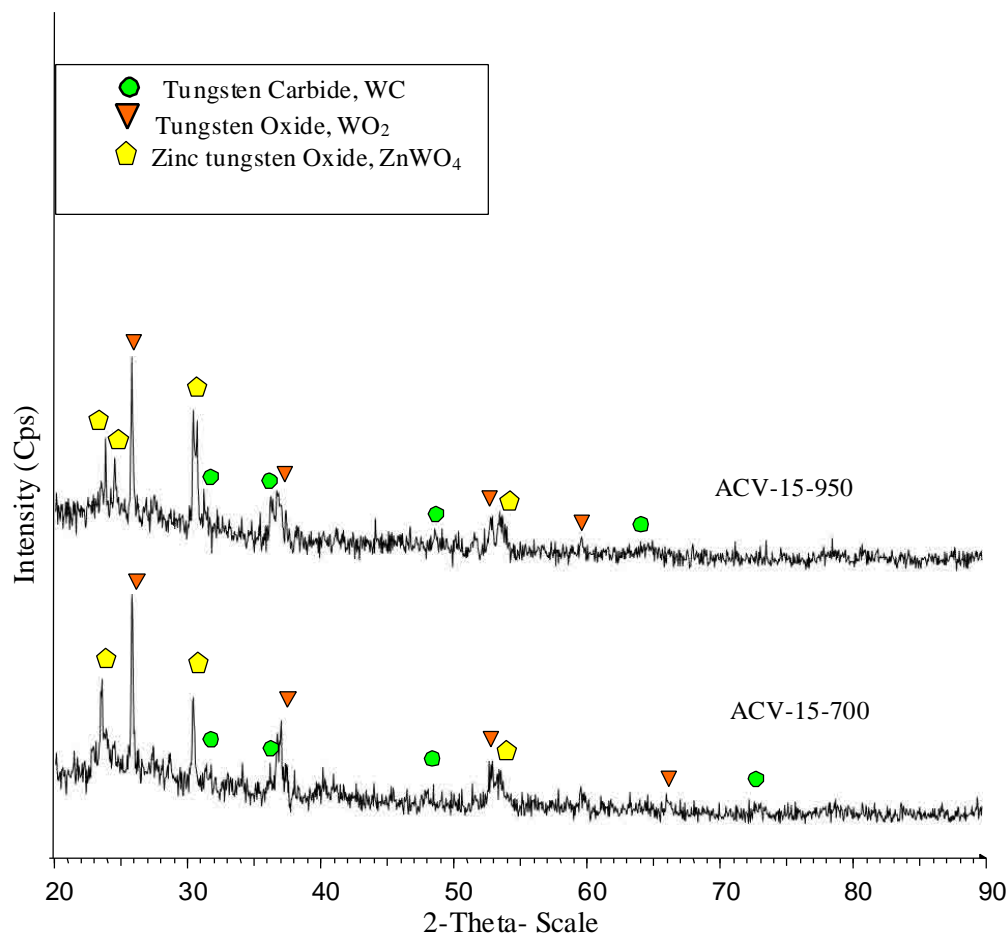


Figure 4.25: X-ray diffractogram of samples with 15 percent of tungsten content supported on AC-1Z-V

The relative intensity of the main peaks is shown in Table 4.9. From the data obtained, ACV-6-950 shows the highest tungsten carbide formation while ACV-15-700 shows the lowest relative intensity of tungsten carbide peak. However, there is no exact pattern observed towards the formation of WC indicates that the tungsten content and the heat treatment temperature affected the WC formation. This can be explained by the presence of zinc residues in the carbon source, which reacted with tungsten and formed ZnWO₄. As a result the formation of tungsten carbide is reduced compared to the previous samples prepared from AC-1Z-N.

From the results obtained, it can be seen that the intensity of ZnWO₄ peaks reduced when the tungsten content increased. This is possibly due to the substantial

amount of tungsten exists in the form of tungsten dioxide. The table clearly showed that the 6 percent tungsten content formed tungsten trioxide, whereas 15 percent tungsten formed tungsten dioxide. The formation of WO_3 and WO_2 in the case of the AC-1Z-V supported catalysts is a function of tungsten content. The ratio of O/W decrease as the tungsten increase and become 2.

Table 4.9: Relative intensity of main peaks for AC-1Z-V supported catalysts

Sample	ACV-6-700	ACV-6-950	ACV-15-700	ACV-15-950
Tungsten carbide, WC	36.5	58.2	32.4	42.0
Tungsten oxide, WO_3	54.4	80.3	-	-
Tungsten oxide, WO_2	-	-	100.0	100.0
Zinc tungsten oxide, $ZnWO_4$	100.0	100.0	64.6	57.5

4.3.2 Field Emission Scanning Electron Microscopy

The surface morphology of the samples was studied using Field Emission Scanning Electron Microscopy (FESEM). In subtopic 4.3.1.1, it had been shown that the catalyst sample supported on AC-1Z-N with 15 percent tungsten content and heat treated at 950°C gives better formation of tungsten carbide. While the XRD results in previous subtopic show that the presence of Zinc tungsten oxide, $ZnWO_4$ in all the catalyst supported on AC-1Z-V. However, ACV-15-950 was selected to compare the surface morphology with ACN-15-950. Figure 4.26 and 4.27 show the FESEM micrographs of ACN-15-950 and ACV-15-950 respectively.

From the micrograph, morphology changes were observed in the structure of catalysts as compared to the AC-1Z-N (see Figure 4.11) and AC-1Z-V (see Figure 4.13). It can be seen clearly that the tungsten species particles are well dispersed on the surface of activated carbon. Pores which are clearly seen in activated carbon supports (Figure 4.11 and Figure 4.13) were unnoticeable after catalyst preparation.

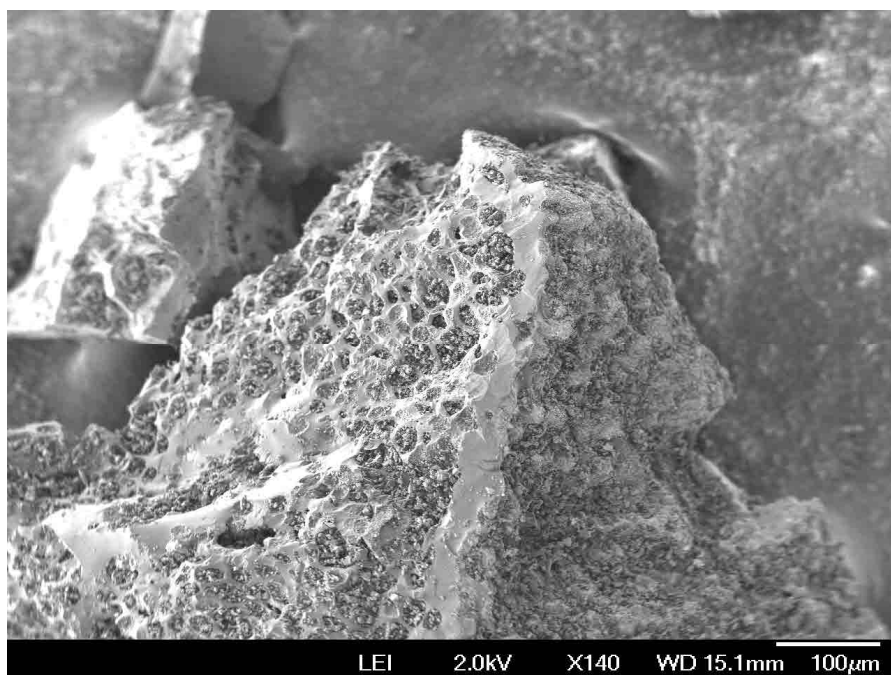


Figure 4.26: Micrograph of ACN-15-950 with magnification of 140x

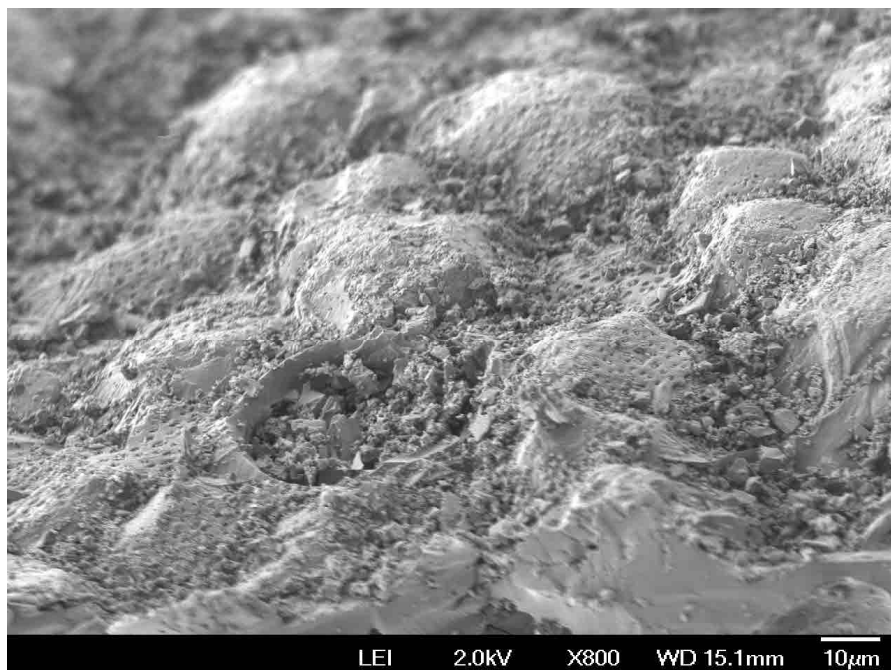


Figure 4.27: Micrograph of ACV-15-950 with magnification of 800x

The EDX analysis was carried out on the samples. Figure 4.28 and Figure 4.29 show the EDX analysis for ACN-15-950 and ACV-15-950 respectively. From the results, the presence of zinc peaks in ACV-15-950 is in agreement with XRD results (see subtopic 4.3.1.2), whereby the carbon source used is chemically activated carbon using ZnCl_2 . The intensity of the carbon peak it is clearly shown that the carbon from the support dominated the surface area, meaning that the catalyst is either not distributed evenly, or have been entered into the carbon pores due to the high surface area and porosity.

The presence of oxygen peak in ACV-15-950 probably comes from tungsten oxide phases, which is in agreement with XRD result (Figure4.25).The oxygen peak in ACN-15-950 may be contributes by the water molecules or functional groups adsorbed on the catalyst surface during the sample preparation as there is no peak of tungsten oxide detected in the XRD analysis (Figure 4.23).

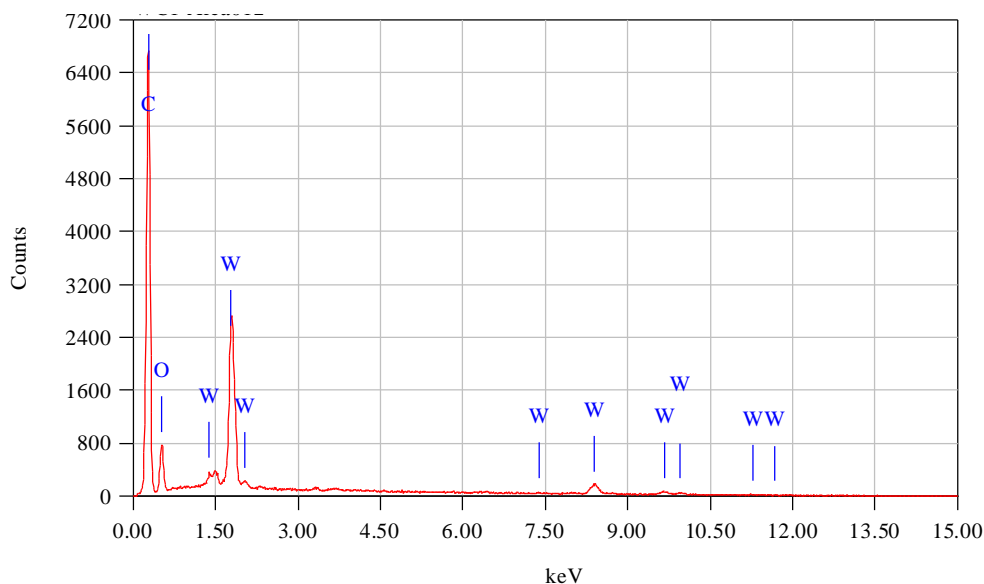


Figure 4.28: EDX of ACN-15-950

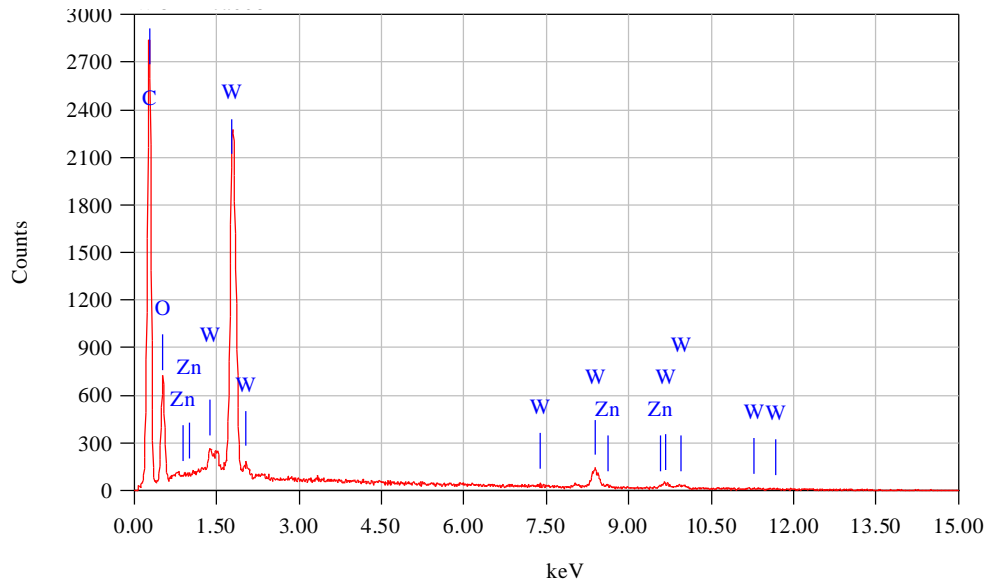


Figure 4.29: EDX of ACV-15-950

4.3.3 Single point BET surface area

BET analysis was done to study the effect of tungsten content on the surface of the catalysts. All the tungsten carbide catalysts supported on AC-1Z-N were subjected to single point BET analysis. Table 4.10 shows the comparison of surface area for catalysts with 6% and 15% tungsten content were heat treated at 700°C and 950°C.

Table 4.10: Single point BET surface area of samples

Sample	BET surface area (m ² g ⁻¹)
Activated carbon (AC-1Z-N)	878
ACN-6-700	744
ACN-6-950	630
ACN-15-700	594
ACN-15-950	354

The surface area decreased with the increased in tungsten content. The highest surface area was obtained in ACN-6-700 with 744 m²g⁻¹ followed by ACN-6-950 with 630 m²g⁻¹. While ACN-15-700 and ACN-15-950 give 594 m²g⁻¹ and 354 m²g⁻¹ respectively.

For ACN-6-700, the surface area of the sample is mainly contributed by the activated carbon. As the tungsten content increased to 15% the surface area decreased. This might be due to the pore structure in activated carbons which consists of an interconnected network of pores of different size; micro, meso and macropores. Gas molecules during the BET analysis can only reach microporosity by passing through meso and macropores. However, when large metal content are deposited on an activated carbon there is the possibility of blocking the entrance of large pores, which would also block the access to a portion of smaller pores. Therefore, the higher the tungsten content the more micropores are blocked and the lower the surface area (Alvarez-Merino *et al.*, 2000; Perez-Cadenas *et al.*, 2003).

The results also show that the surface area decreased as the temperature of heat treatment increased. The tungsten particles were sintered when the treatment temperature increased resulting in the loss of surface area (Moreno-Castilla *et al.*, 2001).

4.4 Hydrodehalogenation of CFC-12

Catalytic hydrodehalogenation of dichlorodifluoromethane (CCl_2F_2 , CFC-12) was carried out using the previously prepared tungsten carbide catalyst. From the finding earlier, it is also deduced that the samples with 15 percent tungsten content heat treated at 950°C shows better formation of tungsten carbide. It is also deduced that catalyst supported on AC-1Z-N is better than catalyst supported on AC-1Z-V. In order to choose the optimally prepared catalyst for the hydrodehalogenation reaction, ACN-15-950 was selected due to its considerably high surface area and the absence of tungsten oxide species which is inactive in hydrodehalogenation reaction.

The hydrodehalogenation reaction in the system was carried out in the microreactor whereby the mixed gas of CFC-12 and H_2 as well as He as carrier gas were passed over the tungsten carbide catalyst. The catalyst was placed in a reactor furnace. The reaction temperature was increased from 200 to 350°C and the composition of the products was analysis using gas chromatography.

Figure 4.30 shows the GC chromatogram of CFC-12 gas. A sharp peak was observed at the retention time (R_t) of 1.936 minutes. Figure 4.31 shows the GC chromatograms of product mixture obtained from hydrodehalogenation of CFC-12 at different temperature. All the chromatograms show a similar pattern with three main peaks. It was found that besides the existence of the CFC-12 peak, two extra peaks were identified around R_t value of 2.5 and 3.5 minutes. Although the identification of the products was not done, the presence of these two peaks is significant enough to prove that CFC-12 was successfully hydrodehalogenated with the prepared catalyst, ACN-15-950.

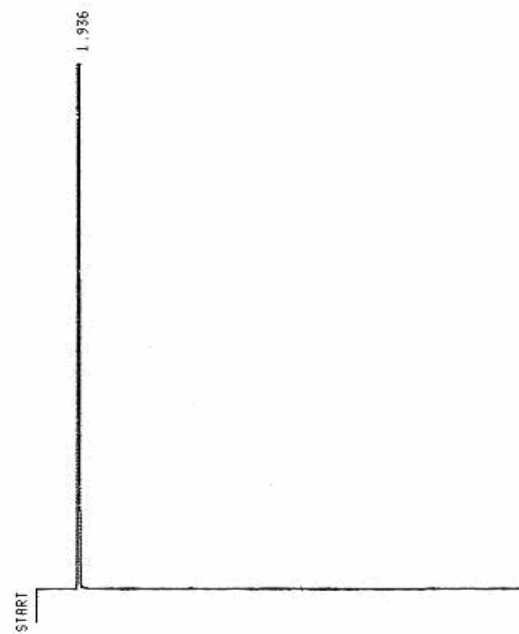


Figure 4.30: Chromatogram of CFC-12 gas.

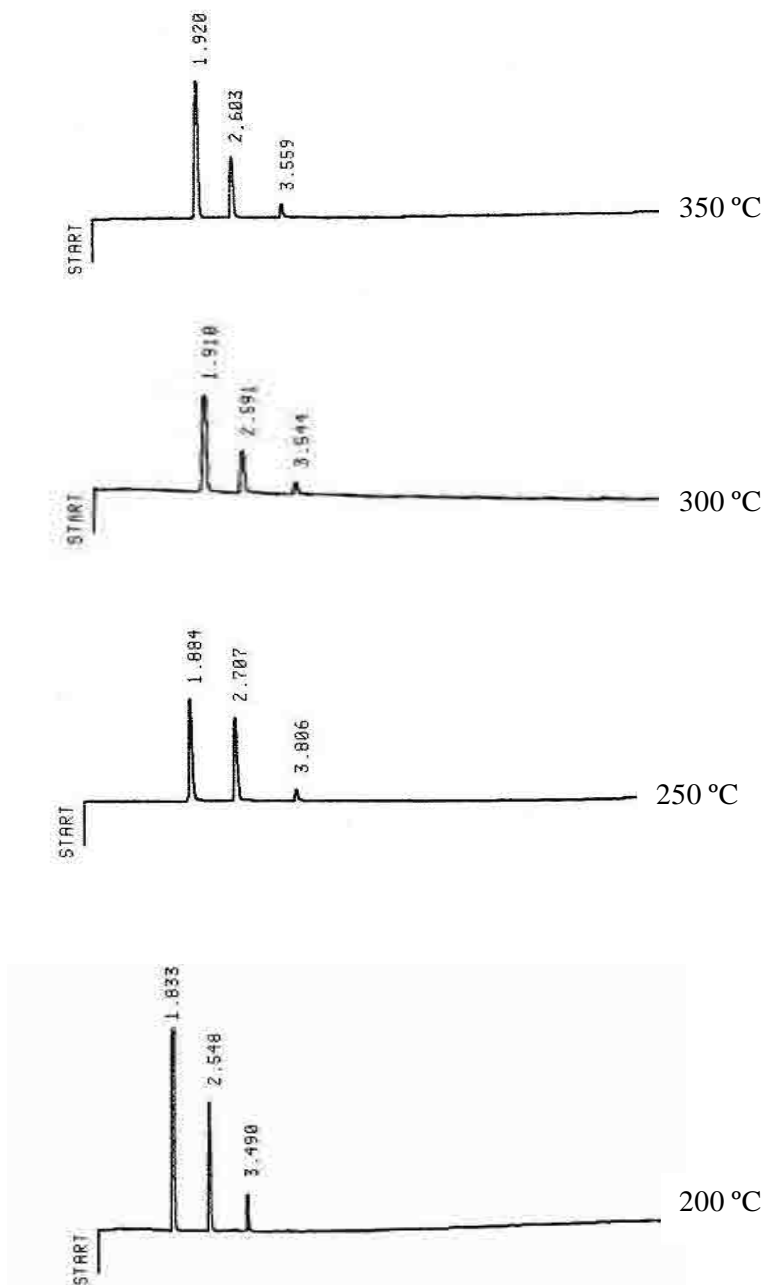


Figure 4.31: Chromatograms of product mixture at different temperature.

Figure 4.32 presents the conversion of CFC-12 at different reaction temperatures. It is clear that the conversion increase with the reaction temperature. At 200°C about 93% of conversion was detected. When the reaction temperature is increased to 250°C the conversion of CFC-12 increased to 96% over ACN-15-950. The highest conversion was recorded at the reaction temperature of 350°C with 98%.

It was found that the catalyst shows a rapid deactivation in the early stages of the reaction. This deactivation is most probably attributed to a site blocking phenomenon due to a strong deposit of polymeric carbon and of hydrofluorocarbon polymers (Delonnoy *et al.*, 2000). However, the high conversion of CFC-12 showed by AC-15-950 suggests that it could be an alternative catalyst for catalytic hydrodehalogenation of CFCs.

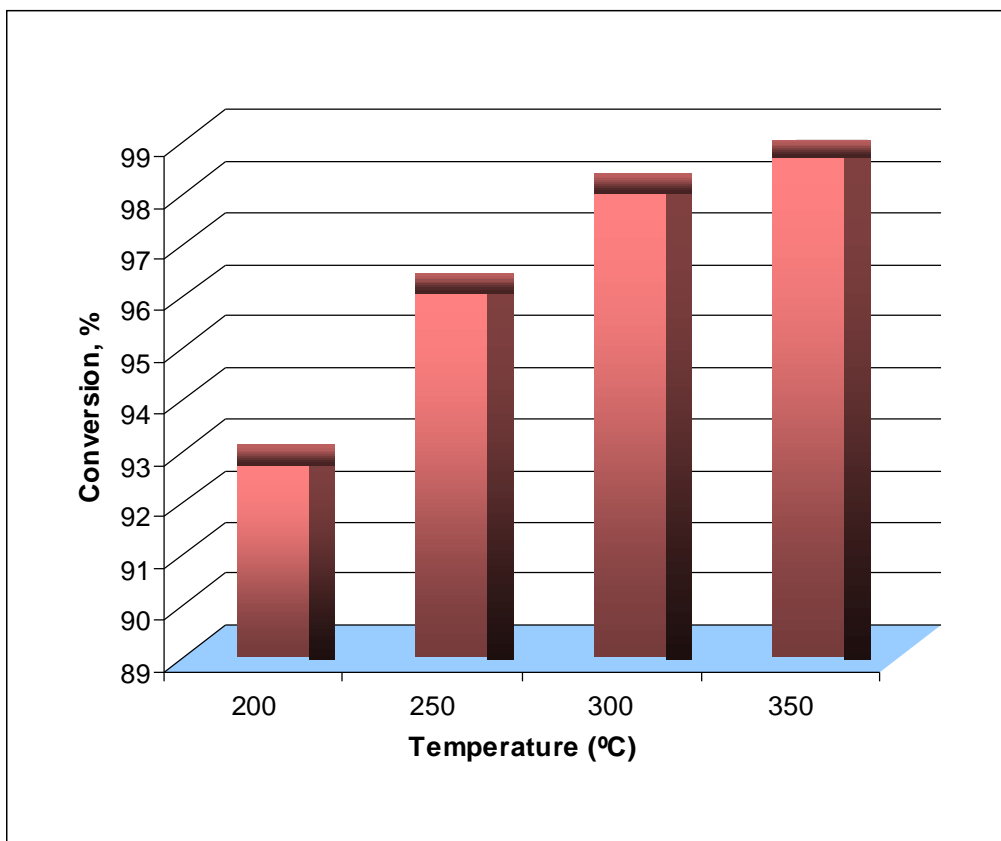


Figure 4.32: Conversion of CFC-12

CHAPTER 5

CONCLUSION

In conclusion, this study has achieved all the stated objectives. Four types of carbons were successfully prepared and characterized. The study showed that the ratio of ZnCl_2 to palm kernel shell and condition of activation process influenced the physical properties of an activated carbon.

The FTIR results indicated that all the reacted palm kernel shells were successfully converted into carbon after 2 hours of activation. Single point BET surface area of all the carbons prepared were obtained and AC-1Z-N showed the highest surface area with $878 \text{ m}^2\text{g}^{-1}$. This supported by FESEM micrographs, which shows a well developed internal cavities and clean surface compare to AC-1Z-V. Nitrogen adsorption analysis shows that AC-1Z-N indeed has high micropore surface area and micropore volume with average pore diameter of 1.95 nm. It was found that activation under nitrogen flow, the characteristics of the carbons produced are better than those under vacuum condition. The results showed that at ZnCl_2 impregnation ratio of 1:1, the activated carbon were predominantly micropores, while when the ratio increased to two the micropore volume declined.

In this study AC-1Z-N is found to be the optimal activated carbon prepared and it showed that palm kernel shells can be a better source of high surface area activated carbon.

This research also has succeeded in preparing tungsten carbide catalyst using the previously prepared activated carbon AC-1Z-N and AC-1Z-V. The results showed

that the type of carbon support, tungsten content and temperature of heat treatment influence the formation of tungsten carbide. From XRD analysis it was found that tungsten carbide supported on AC-1Z-N showed better formation of tungsten carbide. The catalyst supported on AC-1Z-N with 15 percent tungsten content and heat treated at 950 °C was found to be the high tungsten carbide formation. It also observed that Zn ions were present in all the samples prepared from AC-1Z-V.

Finally the catalytic hydrodehalogenation of CFC-12 has successfully carried out using the optimal prepared tungsten carbide, ACN-15-950, which give a positive results. However, the catalyst shows a rapid deactivation in the early stages of the reaction. It was suggested that it could be an alternative routes for the traditional catalyst used, Pd/C for it showed similarity towards the hydrodehalogenation of CFC-12.

REFERENCES

- Ahmad, A.L., Loh, M.M., Aziz, J.A. (2007). Preparation and characterization of activated carbon from oil palm wood and its evaluation on Methylene blue adsorption. *Dyes and Pigments*, **75**, 263-272.
- Ahmadpour, A. and Do, D.D. (1997). The preparation of activated carbon from macadamia nutshell by chemical activation. *Carbon*, **12**, 1723-1732.
- Almansa, C., Molina-Sabio, M. and Rodriguez-Reinoso, F. (2004). Adsorption of methane into ZnCl₂-activated carbon derived discs. *Microporous and Mesoporous Materials*, **76**, 185-191.
- Alvarez-Merino, M.A., Carrasco-Marin, F., Fierro, J.L.G. and Moreno-Castilla, C. (2000). Tungsten catalysts supported on activated carbon. I. Preparation and characterization after their heat treatment in inert atmosphere. *Journal of Catalysis*, **192**, 363-373.
- Alvim-Ferraz, M.C.M. and Gaspar, C.M.T.B (2003). Micropore size distribution of activated carbons impregnated after carbonization. *Journal of Porous Materials*, **10**, 47-55.
- Asiah, H. and Noor Khaidawati, M.S.(2005). *Introduction to surface and colloid chemistry*. Johor:Universiti Teknologi Malaysia.
- Auer, E., Freud, A., Pietsch, J. and Tacke, T. (1998). Carbons as supports for industrial metal catalysts. *Applied Catalysts A: General*, **173**; 259-271.

- Azevedo, D.C.S., Araujo, J.C.S., Bastos-Neto, M., Torres, A.E.B., Jaguaribe, E.F. and Cavalcante, C.L. (2007). *Microporous and Mesoporous Materials*, **100**, 361-364.
- Bandosz, J.T. (2006) *Activated Carbon Surfaces in Environmental Remediation*. Academic Press.
- Bertin, E.P. (1975). *Principle and Practice of X-ray Spectroscopic Analysis*. New York Plenum Press.
- Boonamnuayvitaya, V., Sae-ung, S. and Tanthapanichakoon (2005). Preparation of activated carbons from coffee residue for the adsorption of formaldehyde. *Separation and Purification Technology*, **42**, 159-168.
- Brzuzy, L.P. and Hites, R.A. (1996). Global mass balance for polychlorinated dibenzo-p-dioxins and dibenzofurans. *Environ. Sci. technol*, **30**, 1797-1804.
- Cameron, D.S., Cooper, S.J., Dodgson, I.L., Harrison, B., and Jenkins, J.W. (1990). Carbons as supports for precious metal catalyst. *Catalysis Today*, **7**, 113-137.
- Caturla, F., Molina-Sabio, M. and Rodriguez-Reinoso, F (1991). Preparation of activated carbon by chemical activation with ZnCl₂. *Carbon*, **29**, 999-1007.
- Chen, J.G. (1996). Carbide and Nitride Overlayers on Early Transition Metal Surfaces: Preparation, Characterization, and Reactivities. *Chemical Reviews*, **96**(4), 1477-1498
- Claridge, J.B., York, A.P.E., Brungs, A.J., Green, M.L.H. (2000). Study of the temperature-programmed reaction synthesis of early transition metal carbide and nitride catalyst materials from oxide precursors. *Chem. Mater.*, **12**(1), 132-142.

- Corella, J. and Toledo, J.M. (2002). Testing total oxidation catalysts for gas cleanup in waste incineration at pilot scale. *Ind. Eng. Chem. Res.*, **41**, 1171-1181
- Daud, W.M.A.W., Ali, W.S.W. and Sulaiman, M.Z. (2000). The effects of carbonization temperature on pore development in palm-shell-activated carbon. *Carbon*, **38**, 1925-1932.
- Daud, W.M.A.W and Ali, W.S.W. (2004). Comparison of activated carbon produced from palm kernel shell and coconut shell. *Bioresorce Technology*, **93**, 63-69.
- Daud, W.M.A.W., Ali W.S.W. (2004). Comparison on pore development of activated carbon produced from palm kernel shell and coconut shell. *Biosource Technology*, **93**, 63-69.
- Delannoy, L., Giraudon, J.-M., Granger, P., Leclercq, L and Leclercq, G. Group VI transition metal carbides as alternatives in the hydrodechlorination of chlorofluorocarbons. *Catalysis today*, **59**, 231-240.
- Figueiredo, J.L. Moulijn. J.A. (2005) *Carbon and Coal Gasification: Science and technology*. Springer.
- Galiatsatou, P., Metaxas, M. and Kasselouri-Rigopoulou, V. (2001). Mesoporous activated carbon from agricultural byproducts. *Microchimica Acta*, **136**, 147-152.
- Gao, L. and Kear, B.H. (1997). Synthesis of nanophase WC powder by a displacement reaction process. *Nanostructured Materials*, **9**, 205-208.
- Gergova, K., Petrov, N. and Eser, S. (1994). Adsorption properties and microstructure of activated carbons produced from agricultural by products by steam activation. *Carbon*, **32**, 693-702.
- Hagen, J. (2006). *Industrial Catalysis: A Practical Approach*. Wiley-VCH.

- Houston, J.E., Iaromare, G.E. and Park, R.L (1974). Surface Electronic Properties of Tungsten, Tungsten Carbide, and Platinum. *Science*, **185**, 258-260.
- Hu, Z., Srinivasan M.P., Ni, Y. and Shi, X.F. (2000). Mesoporous high surface area activated carbon produced from coconut shell. *Adsorption Science and Technology: Proceedings of the Second Pacific Basin Conference*, 269-273.
- Hu, Z., Srinivasan M.P. and Ni, Y. (2001). Novel activation process for preparing highly microporous and mesoporous activated carbons. *Carbon*, **39**, 877-886.
- Hussain, A. and Mohd Saiyudin, N.K.W. (2005). *Introduction to Surface and Colloid Chemistry*. Monograph 1st ed. Universiti Teknologi Malaysia.
- Ioannidou, I. and Zabaniotou, A. (2007). Agricultural residues as precursors for activated carbon production-A Review. *Renewable and Sustainable Energy Reviews*, **11**, 1966-2005.
- Jankowska, H., Swatkowski, A. and Choma, J. (1991). *Active Carbon*. Poland: Ellis Horwood.
- Jaroniec M., Gilpin R.K., Rainier J. and Choma J. (1996). Characterization of microporous carbons by using TGA curves measured under controlled conditions. *Thermochimica Acta*, **272**, 65-73.
- Kawser Md., j. and Farid Nash, A. (2000). Oil Palm Shell as a source of phenol. *Journal of Oil Palm Research*, **12** (1), 86-94.
- Keller, V., Cheval, M., Vayer, M., Ducros, R. and Maire G. (1991). Tungsten carbides as substitutes of platinum in heterogeneous catalysis. I. The effect of surface composition on reaction of Methycyclopentane on tungsten carbides. *Catalysis Letter*, **10**, 137-148.

- Khalili, N.R., Campbell, M., Sandi, G. and Golas, J. (2000). Production of micro- and mesoporous activated carbon from paper mill sludge. I. Effect of zinc chloride activation. *Carbon*, **38**, 1905-1915.
- Kim, J.C. and Kim, B.K. (2004). Synthesis of nanosized tungsten carbide powder by the chemical vapor condensation process. *Scripta Materialia*, **50**, 969-972.
- Kinoshita, K. (1987). *Carbon, Electrochemical and Physicochemical Properties*. Wiley-Interscience.
- Knozinger, H., Ertl, G and Weitkamp, J. (1999). *Preparation of Solid Catalysts*. Willey-VCH.
- Landau, M.V. (1997). Deep hydrotreating of middle distillates from crude and shale oils. *Catalysis Today*, **36** (4), 393-429.
- Lange N.A. (1985). *Handbook of Chemistry*. 13th ed. New York: McGraw Hill.
- Lemaitre, J., Vidick, B. and Delmon, B.(1986). Control of the catalytic activity of tungsten carbides. I: Preparation of highly dispersed tungsten carbides. *Journal of Catalysis*, **99**, 415-427.
- Levy, R.B and Boudard, M. (1973). Platinum-like of tungsten carbide in surface catalysis. *Science*, **181**, 547-549.
- Liang, C., Tian, F., Wei, Z., Xin, Q. and Li, C. (2003). The synthesis of nanostructured W₂C on ultrahigh surface area carbon materials via carbothermal hydrogen reduction. *Nanotechnology*, **14**, 955-958.
- Lua, A. C. and Guo, J (1998). Preparation and characterization of chars from oil palm waste. *Carbon*, **36** (11), 1663-1670.

- Lua, A.C., Lau, F.Y. and Guo, J. (2000). Preparation and characterization of activated carbon from oil-palm shells. *Sustainable Energy and Environmental Technologies: Proceeding of the third Asia Pacific Conference*, 425-429.
- Lua, A. C. and Yang, T. (2004). Effect of activation temperature on the textural and chemical properties of potassium hydroxide activated carbon prepared from pistachio-nut shell. *Journal of Colloid and interface Science*, **274**, 594-601
- Lua, A.C. and Yang, T. (2005). Characteristics of activated carbon prepared from pistachio-nut shell by zinc chloride activation under nitrogen and vacuum conditions. *Journal of Colloid and Interface Science*, **290**, 505-513.
- Manocha, M.S (2003). Porous Carbons. *Sadhana*, **28**, 335-348.
- Marsh, H. and Rodriguez-Reinoso, F. (2006). *Activated carbon*. Elsevier.
- Minkova, V., Razvigorova, M., Goranova, M., Ljutzkanov, L. and Angelova, G. (1991). Effect of water vapour on the pyrolysis of solid fuels. I. Effect of water vapour during the pyrolysis of solid fuels on the yield and composition of the liquid products. *Fuel*, **70**, 713-719.
- Mohanty, K., Das, D. and Biswas, M.N. (2005). Adsorption of phenol from aqueous solutions using activated carbons prepared from *Tectona grandis* sawdust by $ZnCl_2$ activation. *Chemical Engineering Journal*, **115**, 121-131.
- Molina-Sabio M. and Rodriguez-Reinoso F. (2004). Role of chemical activation in the development of carbon porosity. *Colloids and Surface A: Physicochem. Eng. Aspects*, **241**, 15-25.
- Morena-Castilla, C., Alvarez-Merino, M.A., Carrasco-Marin, F., and Fierro, J.L.G. (2001). Tungsten and tungsten carbide supported on activated carbon: surface structures and performance for ethylene hydrogenation. *Langmuir*, **17**, 1752-1756.

- Mowla, D., Do, D.D., Katsumi Kaneko. (2003). Adsorption of water vapor on activated carbon: A brief overview. *Chemistry and Physics of Carbon*, **28**, 230- 241.
- Oatley, C.W. (1972). *The scanning Electron Microscopy*. Cambridge: Cambridge University Press, 66-78.
- Oxley, J.D., Mdleleni, M.M, and Suslick K.S. (2004). Hydrodehalogenation with sonochemically prepared Mo₂C and W₂C. *Catalysis Today*, **88**, 139-151.
- Oyama S.T. and Keiffer R.(1992). Carbides. In: Kirk-Othmer. *Encyclopedia of Chemical Technology*. 4th ed. New York: John Wiley & Sons.
- Oyama, S.T. (1996). *Chemistry of Transition Metal Carbides and Nitrides*.Springer.
- Patterson, P.M, Das, T.K, Davis, B.B. (2003).Carbon monoxide hydrogenation over molybdenum and tungsten carbides. *Applied Catalysis A:General*, **251**, 449-455.
- Perego, G. (1998). Characterization of heterogeneous catalyst by X-ray diffraction techniques. *Catalysis Today*, **41**, 251-259.
- Perez, M.C., Martinez de Lecea, C.S. and Solano, L.A. (1997). Platinum supported on activated carbon cloths as catalyst for nitrobenzene hydrogenation. *Applied catalysis A: General*, **151**, 461-475.
- Perez-Cadenas, A.F., Moreno-Castilla, C., Maldonad-Hodar, F.J. and Fierro, J.L.G. (2003). Tungsten oxide catalysts supported on activated carbons: Effect of tungsten precursor and treatment on dispersion, distribution, and surface acidity of catalysts. *Journal of Catalysis*, **217**, 30-37.
- Ponec V., Knor Z. and Cemy S. (1974). *Adsorption on Solid*. Butterworth: London.

- Putun A.E., Ozbay, N., Onal, E.P. and Putun, E. (2005). Fixed-bed pyrolysis of cotton stalk for liquid and solid products. *Fuel Process Technology*, **86**, 1207-1219.
- Prauchner, J.M., Rodriguez-Reinoso, F. (2007). Preparation of granular activated carbons for adsorption of natural gas. *Microporous and Mesoporous Materials*, **xxx**, xxx-xxx.
- Radovic, R.L. (2001). *Chemistry and Physics of Carbon: A Series of Advances*. CRC Press.
- Rao, P.K., Rao, K.S. and Padmasri, A.H. (2003). Transformation of chlorofluorocarbons through catalytic hydrodehalogenation. *CATTECH*, **7**(6), 218-225.
- Ratna, S.D.D., (2007). *Preparation and characterization of tungsten carbide from carbon of palm kernel shells*. Universiti Teknologi Malaysia. Master Thesis.
- Richardson, J.T. (1989). *Principal of Catalyst Development*. Plenum Press, New York and London. 194.
- Rodrigues, J.A., Cruz, G.M., Buglia, G., Boudart, M. and Djega-Mariadassou. (1997). Nitride and carbide of molybdenum and tungsten as substitutes of iridium for the catalysts used for space communication. *Catalysis Letter*, **45**, 1-3.
- Rodriguez-Reinoso, F. and Solano, A.L. (1989). Microporous structure of activated carbons as revealed by adsorption methods. In: Thrower, A. (Ed.), *Chemistry and Physics of Carbon P*, **21**, 2-141.
- Rodriguez-Reinoso F., Molina-Sabio M. and Gonzalez M.T. (1995). The use of steam and CO₂ as activating agents in the preparation of activated carbons. *Carbon*, **33**, 15-23.
- Rodriguez-Reinoso, F. (1997). The role of carbon materials in heterogeneous catalysis. *Carbon*, **36** (3), 159-175.

- Scott, R.P.W. and Perry, J.A. (1998). *Introduction to Analytical Gas Chromatography*. CRC press.
- Soderstrom, G. and Marklund, S.(2002). The influence of bromine in the formation of halogenated dioxins in combustion processes. *Environ. Sci. Technol*, **36**, 1959.
- Sourabh S., Pansare, Walter T., James G. and Goodwin Jr.(2007). Ammonia decomposition on tungsten carbide. *Catalysis Communications*, **8**, 649-654.
- Stiles, B.A. (1987). *Catalyst Supports and Supported Catalysts*. Butterworths.
- Stuart, B (2004). *Infrared spectroscopy: Fundamental and applications*. John Wiley and Sons. 71-94.
- Suhas, P.J.M., Carrott, M.M.L., Carrott, R. (2007). Lignin-from natural adsorbent to activated carbon: A review. *Bioresource Technology*, **98**, 2301-2312.
- Toth L.E. (1971). *Transition Metal Carbides and Nitrides*. New York: Academic Press.
- Wachowski, L., Kirszensztenjn, P. and Foltynowicz. (2001). Ecological replament of ozone-depleting substances. *Polish Journal of Enviromental Studies*, **10**, 415-435.
- Winterbottom, J.M., King, M.B. (1999). *Reactor Design for Chemical Engineers*. CRC Press.
- Xiao, T., York, A.P.E., Williams, V.C., Al-Megren, H., Hanif, A., Zhou, X., Green, M. L. H. (2000). Preparation of molybdenum Carbides using butane and their catalytic performance. *Chem Mater*, **12**(12), 3896-3905.

- Youssef, A.M., Radwan, N.R.E., Adbel-Gawad, I. and Singer and G.A.A. (2005).
Colloids and Surfaces A: Physicochem. Eng. Aspects, **252**, 143-151.
- Yu, K., Gu, Z., Ji, R., Lan-Lan, L., Ding, F., Zhang, C. and Liu, S. (2007). Effect of pore size on the performance of mesoporous material supported chiral Mn(III) salen complex for the epoxidation of unfunctionalized olefins. *Journal of Catalysis*, **252**, 312-320.
- Zhong-rui, L., Yi-Lu, F., Jiang, M., Tian-duo, H., Liu, t. and Ya-ning, X. (2001). Active carbon supported Mo–K catalysts used for alcohol synthesis. *Journal of Catalysis*, **199**, 155-161.

Appendix 1.0

Calculation of weight used from atomic weight percentage ratio of tungsten and activated carbon support in tungsten carbide preparation

Example : W6/AC-N with ratio tungsten to activated carbon 6: 94

Weight of tungsten carbide catalyst prepared = 3 g

$$\begin{aligned}\text{Weight of W} &= 6 \% \times 3 \text{ g} \\ &= 0.18 \text{ g}\end{aligned}$$

$$\begin{aligned}\text{Weight of tungsten salt} &= \frac{0.18 \text{ g}}{\text{RAM W}} \times \text{RMM W(CO)}_6 \\ \text{W(CO)}_6 &= \frac{0.18 \text{ g}}{183.84 \text{ g/mole}} \times 351.902 \text{ g/mole} \\ &= \mathbf{0.34455 \text{ g}}\end{aligned}$$

$$\begin{aligned}\text{Weight of AC-N} &= \frac{0.18 \text{ g}}{6 \%} \times 94 \% \\ &= \mathbf{2.82 \text{ g}}\end{aligned}$$

Appendix 2.0

Nitrogen Adsorption Data of AC-1Z-N

Full Report Set

ASAP 2010 V3.01 G

Unit 1

Serial # 2017

Page 24

Sample: AC-N
 Operator: Abd Rahim Ali
 Submitter: Vicinisvarri
 File Name: C:\ASAP2010\DATA\002-048.SMP

Started: 09/29/06 16:43:30 Analysis Adsorptive: N2
 Completed: 09/29/06 20:24:40 Analysis Bath: 77.35 K
 Report Time: 10/02/06 08:20:31 Thermal Correction: No
 Sample Weight: 0.1460 g Smoothed Pressures: No
 Warm Freespace: 29.1704 cm³ Cold Freespace: 90.8741 cm³
 Equil. Interval: 5 secs Low Pressure Dose: None

Summary Report

Area

Single Point Surface Area at P/Po 0.20413110 :	878.2365	m ² /g
BET Surface Area:	883.9791	m ² /g
Langmuir Surface Area:	1197.0332	m ² /g
Micropore Area:	40.1634	m ² /g
BJH Adsorption Cumulative Surface Area of pores between 17.000000 and 3000.000000 A Diameter:	222.1902	m ² /g
BJH Desorption Cumulative Surface Area of pores between 17.000000 and 3000.000000 A Diameter:	229.6586	m ² /g

Volume

Single Point Total Pore Volume of pores less than 3107.7747 A Diameter at P/Po 0.99375448:	0.431426	cm ³ /g
Micropore Volume:	-0.033147	cm ³ /g
BJH Adsorption Cumulative Pore Volume of pores between 17.000000 and 3000.000000 A Diameter:	0.143205	cm ³ /g
BJH Desorption Cumulative Pore Volume of pores between 17.000000 and 3000.000000 A Diameter:	0.147337	cm ³ /g

Pore Size

Average Pore Diameter (4V/A by BET):	19.5220	A
BJH Adsorption Average Pore Diameter (4V/A):	25.7806	A
BJH Desorption Average Pore Diameter (4V/A):	25.6619	A

APPENDIX 3.0

Nitrogen Adsorption Data of AC-1Z-V

Full Report Set

ASAP 2010 V3.01 G

Unit 1

Serial # 2017

Page 24

Sample: AC-Z
 Operator: Abd Rahim Ali
 Submitter: Vicinivarri
 File Name: C:\ASAP2010\DATA\002-047.SMP

Started: 09/29/06 10:29:58 Analysis Adsorptive: N2
 Completed: 09/29/06 14:23:20 Analysis Bath: 77.35 K
 Report Time: 09/29/06 15:02:16 Thermal Correction: No
 Sample Weight: 0.2254 g Smoothed Pressures: No
 Warm Freespace: 28.6876 cm³ Cold Freespace: 90.1184 cm³
 Equil. Interval: 5 secs Low Pressure Dose: None

Summary Report

Area

Single Point Surface Area at P/Po 0.20302473 :	713.6364	m ² /g
BET Surface Area:	698.5024	m ² /g
Langmuir Surface Area:	931.1868	m ² /g
Micropore Area:	231.1881	m ² /g
BJH Adsorption Cumulative Surface Area of pores between 17.000000 and 3000.000000 A Diameter:	73.7950	m ² /g
BJH Desorption Cumulative Surface Area of pores between 17.000000 and 3000.000000 A Diameter:	77.2626	m ² /g

Volume

Single Point Total Pore Volume of pores less than 6541.0301 A Diameter at P/Po 0.99705245:	0.335265	cm ³ /g
Micropore Volume:	0.087639	cm ³ /g
BJH Adsorption Cumulative Pore Volume of pores between 17.000000 and 3000.000000 A Diameter:	0.050412	cm ³ /g
BJH Desorption Cumulative Pore Volume of pores between 17.000000 and 3000.000000 A Diameter:	0.053223	cm ³ /g

Pore Size

Average Pore Diameter (4V/A by BET):	19.1991	A
BJH Adsorption Average Pore Diameter (4V/A):	27.3252	A
BJH Desorption Average Pore Diameter (4V/A):	27.5545	A

APPENDIX 4.0

Nitrogen Adsorption Data of AC-2Z-N

Full Report Set

ASAP 2010 V3.01 G

Unit 1

Serial # 2017

Page 24

Sample: AC-Z2
 Operator: Abd Rahim Ali
 Submitter: Vicinisuarri
 File Name: C:\ASAP2010\DATA\002-095.SMP

Started: 12/27/06 17:03:47 Analysis Adsorptive: N2
 Completed: 12/27/06 23:42:09 Analysis Bath: 77.35 K
 Report Time: 01/03/07 09:06:54 Thermal Correction: No
 Sample Weight: 0.1130 g Smoothed Pressures: No
 Warm Freespace: 28.5221 cm³ Cold Freespace: 88.4187 cm³
 Equil. Interval: 5 secs Low Pressure Dose: None

Summary Report

Area

Single Point Surface Area at P/Po 0.20085906 :	499.8609	m ² /g
BET Surface Area:	485.6073	m ² /g
Langmuir Surface Area:	645.3548	m ² /g
Micropore Area:	279.1015	m ² /g
BJH Adsorption Cumulative Surface Area of pores between 17.000000 and 3000.000000 A Diameter:	67.0752	m ² /g
BJH Desorption Cumulative Surface Area of pores between 17.000000 and 3000.000000 A Diameter:	64.5258	m ² /g

Volume

Single Point Total Pore Volume of pores less than 3730.7821 A Diameter at P/Po 0.99480743:	0.245721	cm ³ /g
Micropore Volume:	0.118547	cm ³ /g
BJH Adsorption Cumulative Pore Volume of pores between 17.000000 and 3000.000000 A Diameter:	0.054244	cm ³ /g
BJH Desorption Cumulative Pore Volume of pores between 17.000000 and 3000.000000 A Diameter:	0.047941	cm ³ /g

Pore Size

Average Pore Diameter (4V/A by BET):	20.2403	A
BJH Adsorption Average Pore Diameter (4V/A):	32.3479	A
BJH Desorption Average Pore Diameter (4V/A):	29.7189	A

APPENDIX 5.0

Nitrogen Adsorption Data of AC-2Z-V

Sample: AC-Z1
 Operator: Abd Rahim Ali
 Submitter: Vicinisvarri
 File Name: C:\ASAP2010\DATA\002-114.SMP

Started: 01/05/07 11:39:55 Analysis Adsorptive: N2
 Completed: 01/05/07 16:35:03 Analysis Bath: 77.35 K
 Report Time: 01/10/07 08:10:01 Thermal Correction: No
 Sample Weight: 1.0000 g Smoothed Pressures: No
 Warm Freespace: 29.1508 cm³ Cold Freespace: 90.6385 cm³
 Equil. Interval: 5 secs Low Pressure Dose: None

 Summary Report

Area

Single Point Surface Area at P/Po 0.20592648 :	179.1060	m ² /g
BET Surface Area:	180.5782	m ² /g
Langmuir Surface Area:	246.2972	m ² /g
Micropore Area:	1.9539	m ² /g
BJH Adsorption Cumulative Surface Area of pores between 17.000000 and 3000.000000 A Diameter:	54.5470	m ² /g
BJH Desorption Cumulative Surface Area of pores between 17.000000 and 3000.000000 A Diameter:	57.0360	m ² /g

Volume

Single Point Total Pore Volume of pores less than 3625.6481 A Diameter at P/Po 0.99465532:	0.092129	cm ³ /g
Micropore Volume:	-0.010157	cm ³ /g
BJH Adsorption Cumulative Pore Volume of pores between 17.000000 and 3000.000000 A Diameter:	0.037349	cm ³ /g
BJH Desorption Cumulative Pore Volume of pores between 17.000000 and 3000.000000 A Diameter:	0.038465	cm ³ /g

Pore Size

Average Pore Diameter (4V/A by BET):	20.4075	A
BJH Adsorption Average Pore Diameter (4V/A):	27.3888	A
BJH Desorption Average Pore Diameter (4V/A):	26.9758	A

APPENDIX 6.0

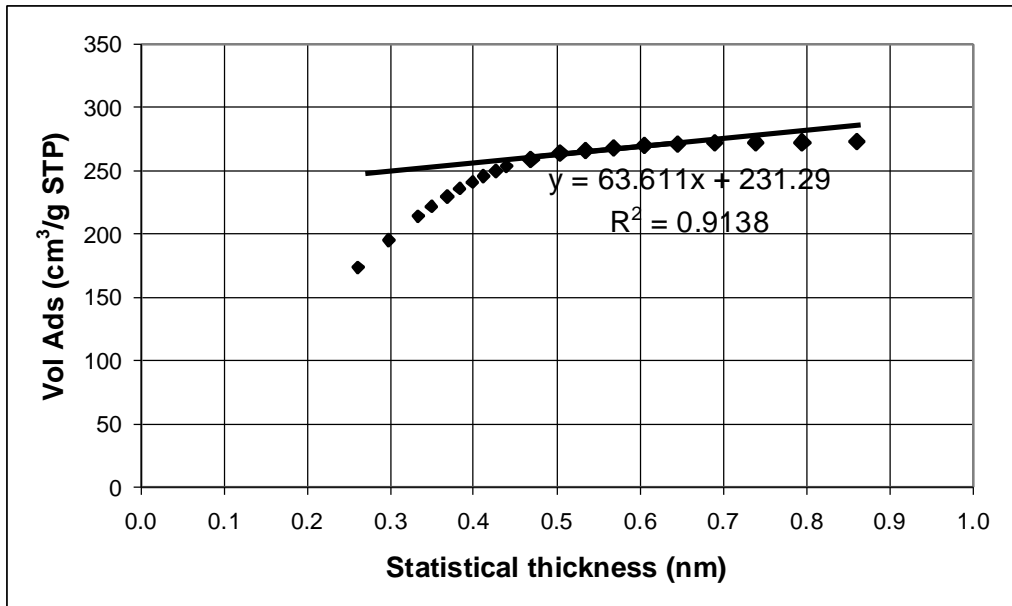
t-Plot Analysis of AC-1Z-N

Harkin-Jura equation:

$$t(\text{\AA}) = \left[\frac{13.99}{(0.0340 - \log P / P_o)} \right]^{1/2}$$

Data :

<i>P/P_o</i>	0.0340-log(<i>P/P_o</i>)	<i>t</i> (nm)	V_{ads}(cm³g⁻¹)
0.009745770	2.045184	0.261543	173.9976
0.028634526	1.577110	0.297836	195.5121
0.059679388	1.258176	0.333456	214.2914
0.076875622	1.148211	0.349058	221.7777
0.100405806	1.032242	0.368144	230.2261
0.120893893	0.951596	0.383427	236.3384
0.141594462	0.882954	0.398052	241.5948
0.162450542	0.823279	0.412226	246.1643
0.183576117	0.770184	0.426198	250.1135
0.204131104	0.724091	0.439554	253.4904
0.250134881	0.635826	0.469072	259.3094
0.304687142	0.550146	0.504278	264.0002
0.348863334	0.491345	0.533600	266.5389
0.399267142	0.432736	0.568587	268.4961
0.449261002	0.381501	0.605565	269.9432
0.499556191	0.335416	0.645828	271.0830
0.549478738	0.294049	0.689761	272.0813
0.59974597	0.256033	0.739199	272.8856
0.64943923	0.221461	0.794803	272.8856
0.69956040	0.189175	0.859958	273.5986



Calculation :

$$t\text{-Plot equation: } y = 63.61x + 231.29$$

$$\text{Intercept, } i = 231.29$$

$$\begin{aligned} \text{Micropore volume, } V_{MP} &= 231.29 \times 0.001547 \text{ cm}^3/\text{g} \\ &= 0.3578 \text{ cm}^3/\text{g} \end{aligned}$$

$$\text{Slope, } s = 63.61$$

$$\begin{aligned} \text{External surface area, } S_{ex} &= 63.61 \times 0.1 \times 15.47 \text{ m}^2/\text{g} \\ &= 98.40 \text{ m}^2/\text{g} \end{aligned}$$

$$\text{BET surface area, } S_{BET} = 883.9791 \text{ m}^2/\text{g}$$

$$\begin{aligned} \text{Micropore surface area} &= 883.9791 - 98.40 \text{ m}^2/\text{g} \\ &= 785.57 \text{ m}^2/\text{g} \end{aligned}$$

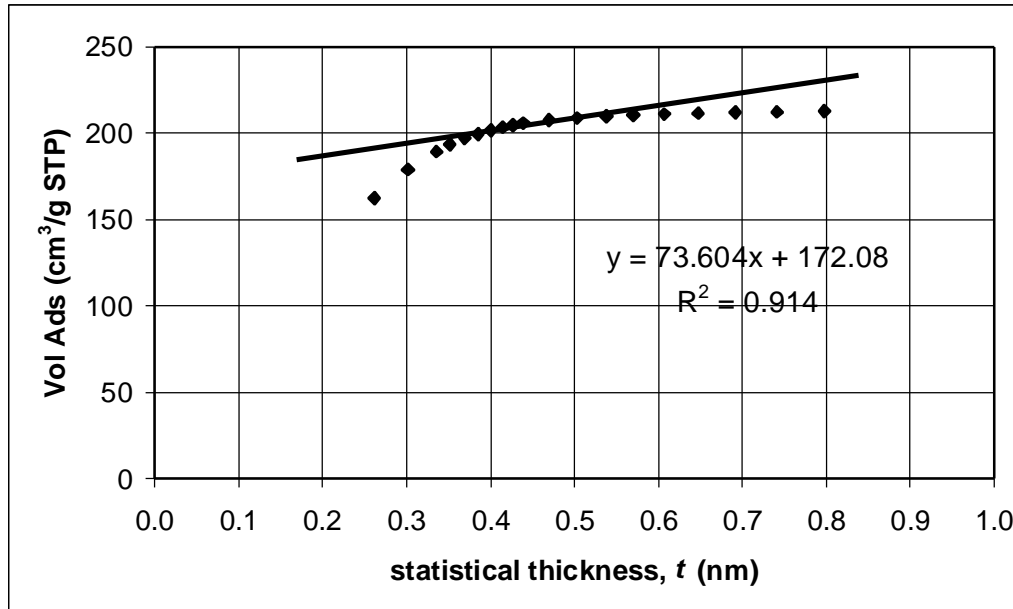
APPENDIX 7.0***t*-Plot Analysis of AC-1Z-V****Harkin-Jura equation**

$$t(\text{\AA}) = \left[\frac{13.99}{(0.0340 - \log P / P_o)} \right]^{1/2}$$

Data:

P/P_o	$0.0340 - \log(P/P_o)$	$t(\text{nm})$	$V_{ads}(\text{cm}^3\text{g}^{-1})$
0.009598230	2.051809	0.261120	162.2812
0.030940146	1.543478	0.301064	178.9416
0.061937125	1.242049	0.335614	189.5982
0.079974776	1.131047	0.351697	193.5397
0.102049407	1.025190	0.369408	197.1282
0.122923975	0.944363	0.384892	199.7114
0.144217589	0.874982	0.399861	201.8031
0.164582825	0.814341	0.414482	203.4110
0.183889143	0.769444	0.426403	204.6620

0.203024732	0.726451	0.438839	205.6950
0.250633323	0.634961	0.469392	207.5935
0.303341592	0.552068	0.503399	209.0090
0.354268511	0.484667	0.537263	209.9832
0.400697376	0.431184	0.569610	210.6509
0.450935519	0.379886	0.606852	211.2188
0.501099792	0.334076	0.647122	211.6944
0.551336040	0.292584	0.691487	212.0767
0.601419765	0.254822	0.740952	212.4143
0.651603741	0.220016	0.797409	212.7023



Calculation:

t -Plot equation: $y = 73.60x + 172.08$

Intercept, i = 172.08

Micropore volume, V_{MP} = $172.08 \times 0.001547 \text{ cm}^3/\text{g}$
= $0.2662 \text{ cm}^3/\text{g}$

Slope, s = 63.45

External surface area, S_{ex} = $73.604 \times 0.1 \times 15.47 \text{ m}^2/\text{g}$
= $113.8653 \text{ m}^2/\text{g}$

BET surface area, S_{BET} = $698.5024 \text{ m}^2/\text{g}$

Micropore surface area = $698.5024 - 113.8653 \text{ m}^2/\text{g}$

$$= 584.6371 \text{ m}^2/\text{g}$$

Appendix 8.0

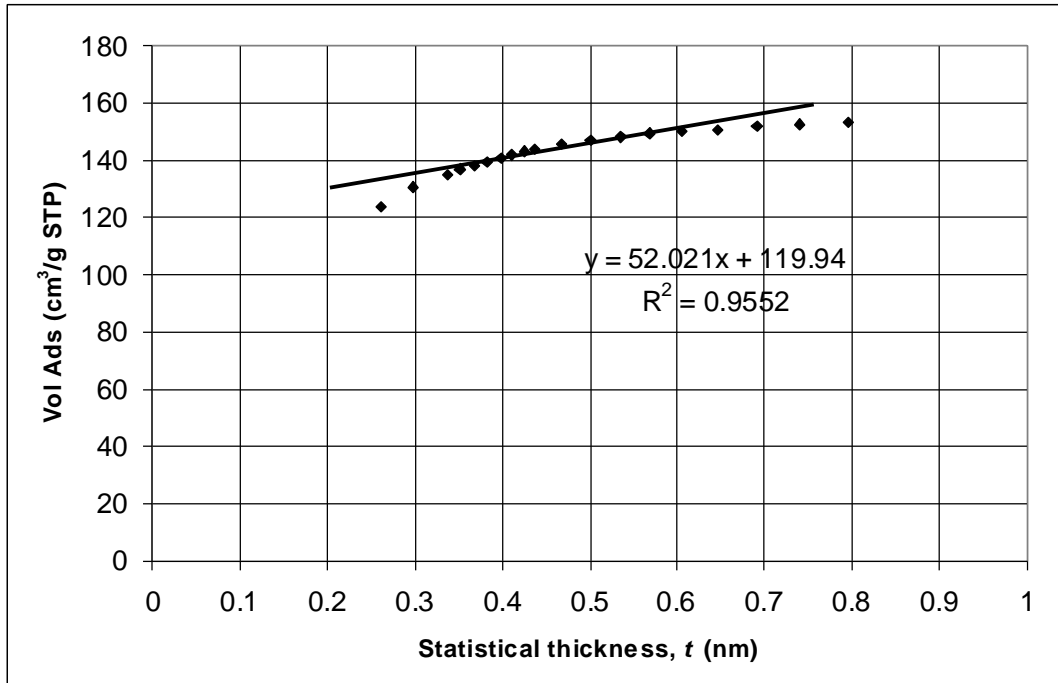
t-Plot Analysis of AC-2Z-N

Harkin-Jura equation:

$$t(\text{\AA}) = \left[\frac{13.99}{(0.0340 - \log P / P_0)} \right]^{1/2}$$

Data:

P/P_0	$0.0340 - \log(P/P_0)$	$t(\text{nm})$	$V_{ads}(\text{cm}^3 \text{g}^{-1})$
0.009817579	2.041996	0.261747	123.9698
0.028716995	1.575861	0.297954	130.3478
0.064571799	0.223957	0.790363	135.1238
0.080810386	1.126533	0.352401	136.6074
0.100680500	1.031055	0.368356	138.1701
0.120763012	0.952066	0.383332	139.6766
0.141254766	0.883997	0.397817	140.8537
0.161293722	0.826383	0.411451	141.8953
0.180937247	0.776472	0.424469	142.8319
0.200859060	0.731109	0.437439	143.6869
0.250054181	0.635966	0.469021	145.3370
0.301078459	0.555320	0.501923	146.8095
0.351310661	0.488309	0.535256	148.0501
0.400107051	0.431823	0.569188	149.1366
0.450210661	0.380584	0.606294	150.0833
0.500190677	0.334864	0.646360	150.8794
0.550085885	0.293569	0.690325	151.6417
0.600174262	0.255723	0.739647	152.3420
0.650214407	0.220943	0.795735	152.9243



Calculation :

t -Plot equation: $y = 52.021x + 119.94$

Intercept, i = 119.94

Micropore volume, V_{MP} = $119.94 \times 0.001547 \text{ cm}^3/\text{g}$
 = $0.18555 \text{ cm}^3/\text{g}$

Slope, s = 52.021

External surface area, S_{ex} = $52.021 \times 0.1 \times 15.47 \text{ m}^2/\text{g}$
 = $80.4765 \text{ m}^2/\text{g}$

BET surface area, S_{BET} = $485.6073 \text{ m}^2/\text{g}$

Micropore surface area = $485.6073 - 80.4765$
 = $405.1323 \text{ m}^2/\text{g}$

Appendix 9.0

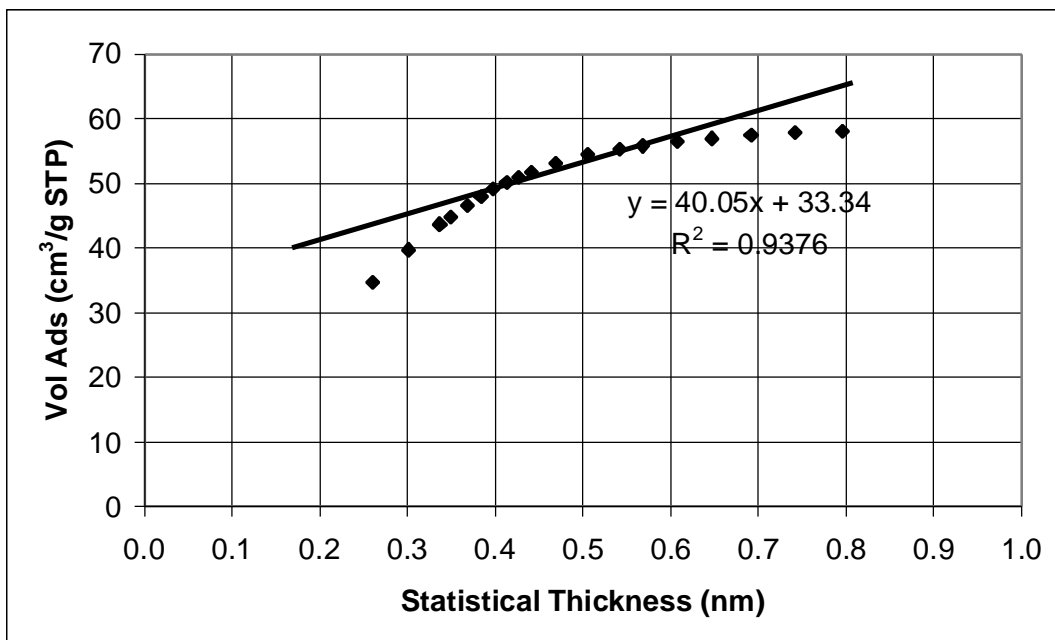
t-Plot Analysis of AC-2Z-V

Harkin-Jura equation:

$$t(\text{\AA}) = \left[\frac{13.99}{(0.0340 - \log P / P_0)} \right]^{1/2}$$

Data:

<i>P/P₀</i>	0.0340- <i>log(P/P₀)</i>	<i>t</i> (nm)	Vads(cm ³ g ⁻¹)
0.009595220	2.051945	0.261111	34.7249
0.030673138	1.547242	0.300697	39.7328
0.063517098	1.231109	0.337101	43.7101
0.076957289	1.147750	0.349128	44.9137
0.100652107	1.031177	0.368334	46.6964
0.121095418	0.950872	0.383573	47.9950
0.142012239	0.881674	0.398341	49.1378
0.163188768	0.821310	0.412720	50.1338
0.184387727	0.768268	0.426729	51.0296
0.205926480	0.720288	0.440713	51.8132
0.250877720	0.634538	0.469548	53.1468
0.307050488	0.546790	0.505823	54.3826
0.360013087	0.477682	0.541177	55.2662
0.399842130	0.432111	0.568998	55.8312
0.451176387	0.379654	0.607037	56.4460
0.501018152	0.334147	0.647054	56.9838
0.551694028	0.292302	0.691820	57.4556
0.601867349	0.254499	0.741422	57.8314
0.649990502	0.221093	0.795466	58.1204



Calculation :

t-Plot equation: $y = 40.05x + 33.34$

Intercept, *i* = 33.34

Micropore volume, V_{MP} = $33.34 \times 0.001547 \text{ cm}^3/\text{g}$
= $0.0516 \text{ cm}^3/\text{g}$

Slope, *s* = 40.05

External surface area, S_{ex} = $40.05 \times 0.1 \times 15.47 \text{ m}^2/\text{g}$
= $61.9574 \text{ m}^2/\text{g}$

BET surface area, S_{BET} = $180.5782 \text{ m}^2/\text{g}$

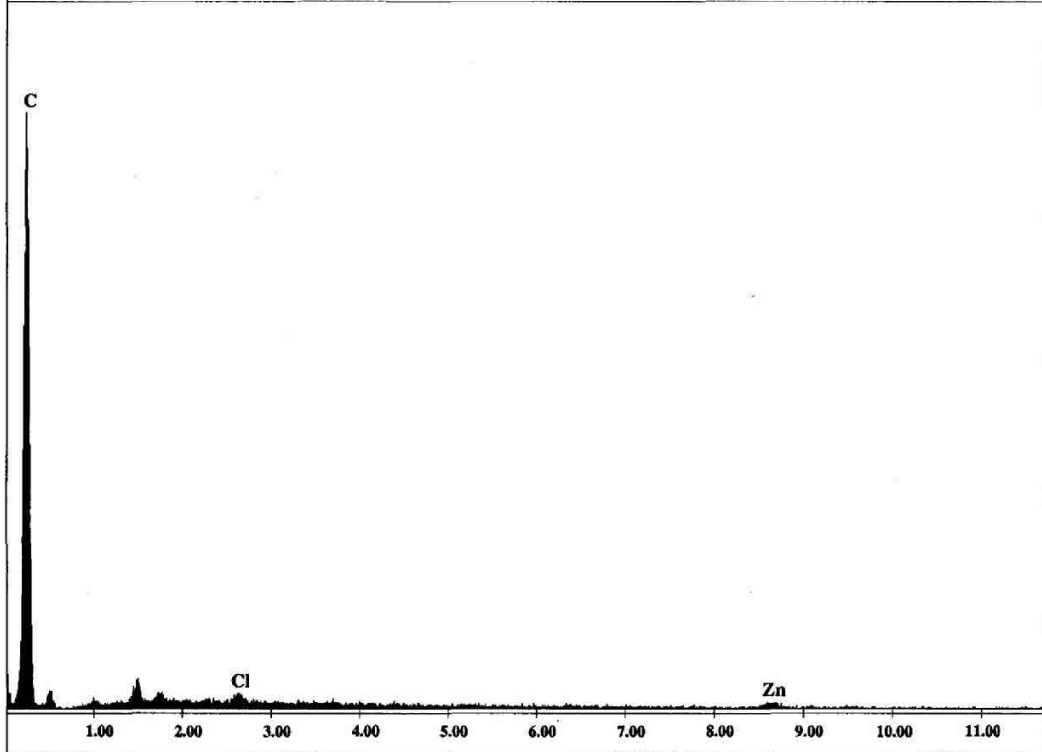
Micropore surface area = $180.5782 - 61.9574 \text{ m}^2/\text{g}$
= $118.6208 \text{ m}^2/\text{g}$

APPENDIX 10.0
EDX Spectrum of AC-1Z-N

kV:30.0 Tilt:0.0 Take-off:36.3 Det Type:SUTW+ Res:131 Tc:100

FS : 1704 Lsec : 34

30-Aug-2006 17:00:30



EDAX ZAF Quantification (Standardless)

Element Normalized

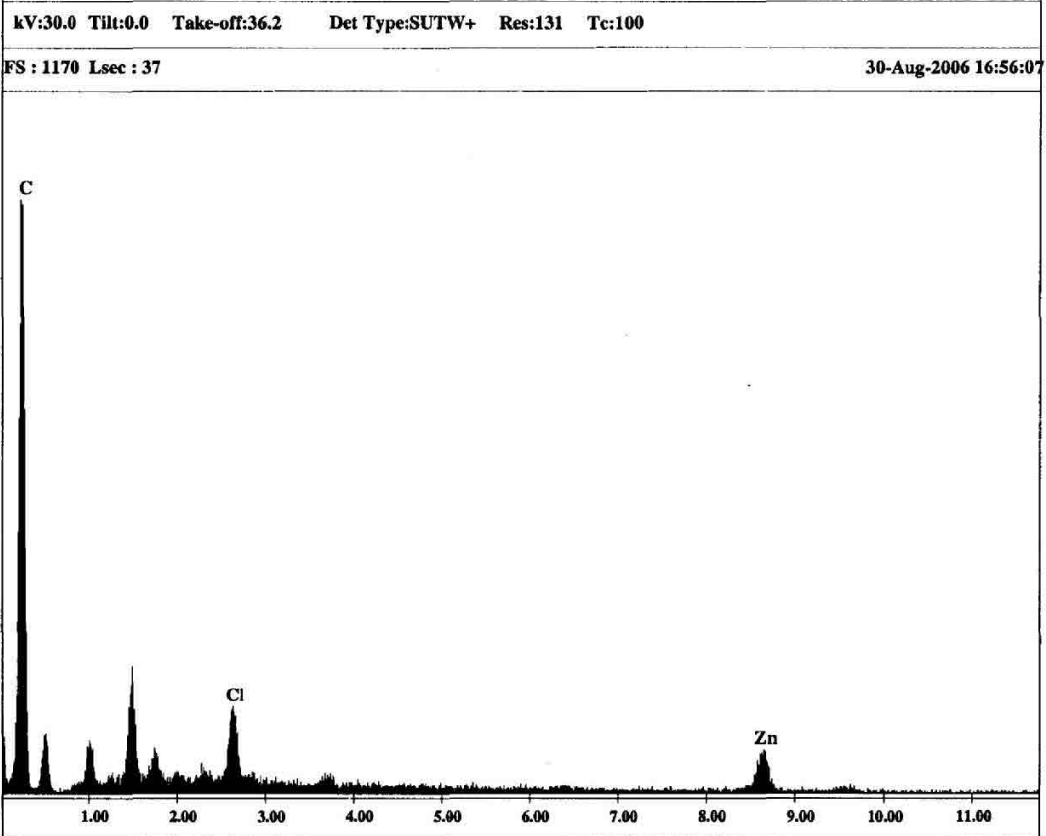
SEC Table : Default

Element	Wt %	At %	K-Ratio	Z	A	F
C K	97.23	99.39	0.7285	1.0034	0.7467	1.0000
ClK	0.59	0.20	0.0056	0.9098	1.0584	1.0000
ZnK	2.19	0.41	0.0188	0.8291	1.0384	1.0000
Total	100.00	100.00				

Element	Net Inte.	Bkgd Inte.	Inte. Error	P/B
C K	131.85	2.01	1.50	65.74
ClK	6.27	4.01	10.20	1.56
ZnK	6.10	0.46	7.35	13.31

APPENDIX 11.0

EDX Spectrum of AC-1Z-V



EDAX ZAF Quantification (Standardless)

Element Normalized
SEC Table : Default

Element	Wt %	At %	K-Ratio	Z	A	F
C K	90.42	97.70	0.4110	1.0118	0.4492	1.0000
ClK	2.37	0.87	0.0217	0.9173	0.9976	1.0000
ZnK	7.20	1.43	0.0624	0.8371	1.0350	1.0000
Total	100.00	100.00				

Element	Net Inte.	Bkgd Inte.	Inte. Error	P/B
C K	86.48	2.09	1.80	41.42
ClK	28.13	5.38	3.63	5.23
ZnK	23.58	0.86	3.49	27.53

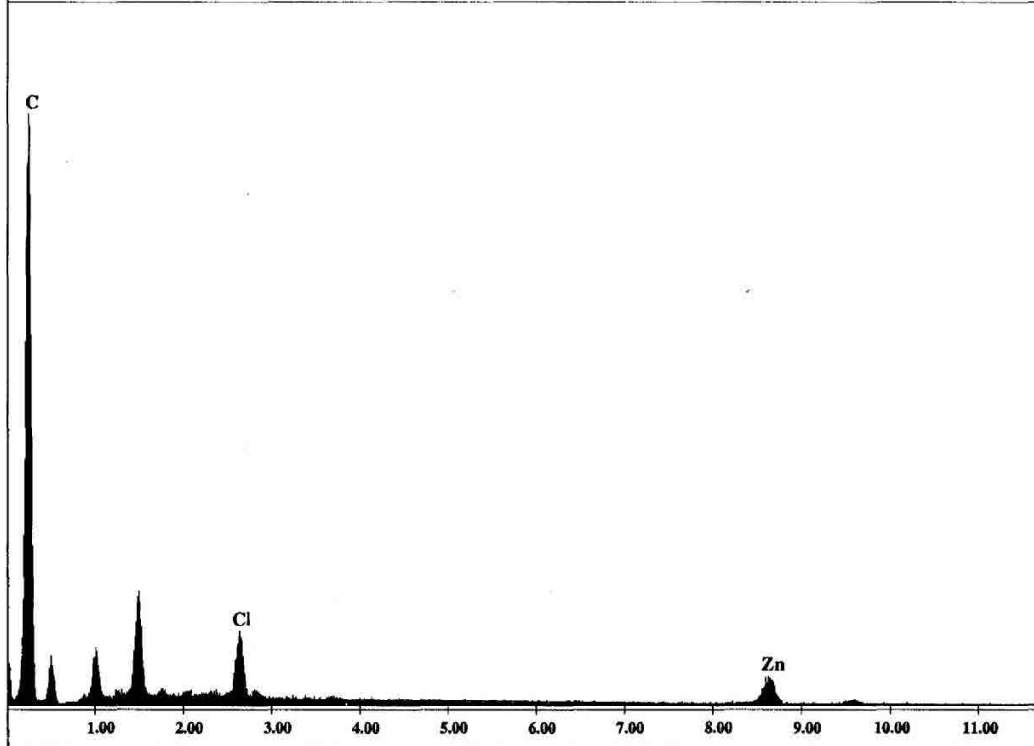
APPENDIX 12.0

EDX Spectrum of AC-2Z-N

kV:30.0 Tilt:0.0 Take-off:36.2 Det Type:SUTW+ Res:131 Tc:100

FS : 3280 Lsec : 74

30-Aug-2006 16:53:04



EDAX ZAF Quantification (Standardless)

Element Normalized

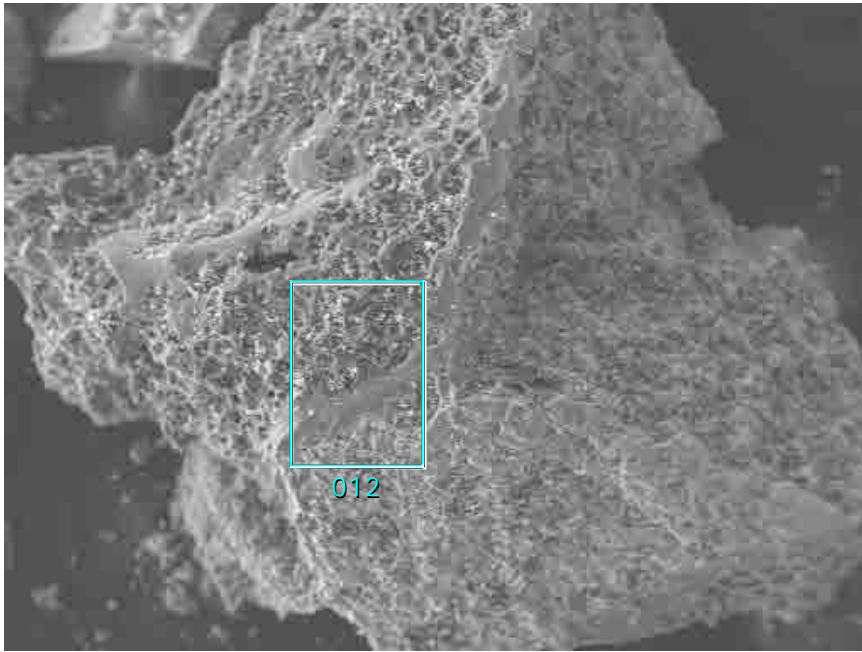
SEC Table : Default

Element	Wt %	At %	K-Ratio	Z	A	F
C K	92.59	98.20	0.4670	1.0090	0.4998	1.0000
ClK	2.15	0.77	0.0200	0.9147	1.0201	1.0000
ZnK	5.26	1.03	0.0455	0.8344	1.0360	1.0000
Total	100.00	100.00				

Element	Net Inte.	Bkgd Inte.	Inte. Error	P/B
C K	122.50	2.21	1.06	55.46
ClK	32.30	5.88	2.38	5.50
ZnK	21.43	1.71	2.69	12.51

APPENDIX 13.0

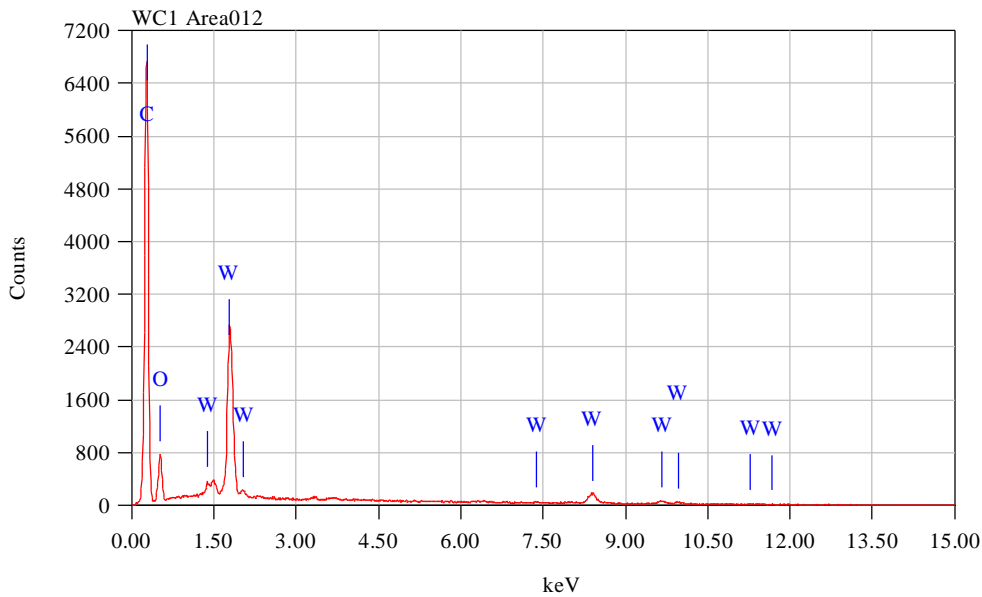
EDX Spectrum of ACN-15-950



Title : IMG1

 Instrument : 6701F
 Volt : 15.00 kV
 Mag. : x 150
 Date : 2007/09/06
 Pixel : 512 x 384

Acquisition Parameter
 Instrument : 6701F
 Acc. Voltage : 15.0 kV
 Probe Current: 2.56160 nA
 PHA mode : T4
 Real Time : 71.96 sec
 Live Time : 50.00 sec
 Dead Time : 30 %
 Counting Rate: 3532 cps
 Energy Range : 0 - 20 keV

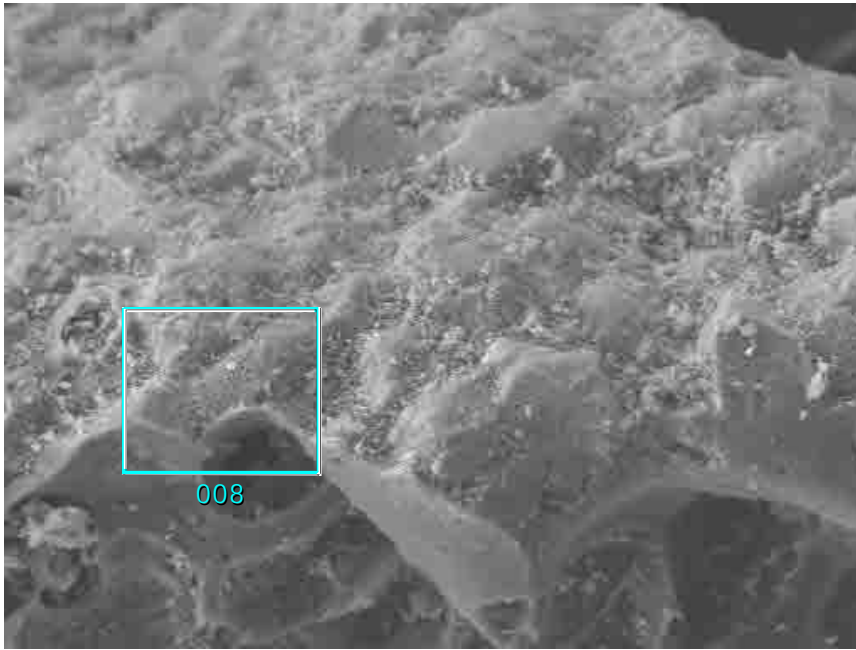


APPENDIX 14.0

ZAF Method Standardless Quantitative Analysis
 Fitting Coefficient : 0.2766

Element	(keV)	Mass%	Error%	Area	Cation	K
C K	0.277	62.51	0.05	84.53		58.2131
O K	0.525	13.11	0.28	13.31		11.6558
W M	1.774	24.37	0.37	2.15		37.7479
Total		100.00		100.00		

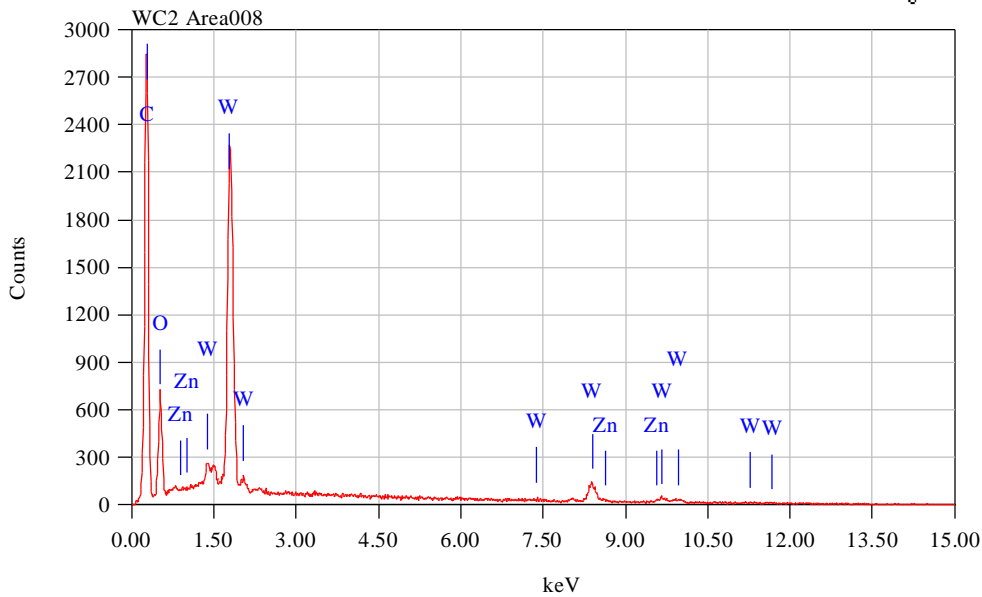
EDS Spectrum of A CV15-050



Title : IMG1

 Instrument : 6701F
 Volt : 15.00 kV
 Mag. : x 500
 Date : 2007/09/06
 Pixel : 512 x 384

100 μm



Acquisition Parameter
 Instrument : 6701F
 Acc. Voltage : 15.0 kV
 Probe Current: 2.56160 nA
 PHA mode : T4
 Real Time : 63.79 sec
 Live Time : 50.00 sec
 Dead Time : 21 %
 Counting Rate: 2483 cps
 Energy Range : 0 - 20 keV

ZAF Method Standardless Quantitative Analysis
 Fitting Coefficient : 0.3011

Element	(keV)	Mass%	Error%	Atom%	Compound	Mass%	Cation	K
C	0.277	48.98	0.05	78.08				35.9162
O	0.525	14.51	0.20	17.36				14.7909
Zn	8.630	3.97	1.86	1.16				7.1727
W	1.774	32.55	0.33	3.39				48.7412
Total		100.00		100.00				